Development of Advanced Multifunctional Optical Coherence Tomography Based on Jones-matrix Theory for Biological Tissue Investigation

En Li

July 2020

Development of Advanced Multifunctional Optical Coherence Tomography Based on Jones-matrix Theory for Biological Tissue Investigation

En Li
Doctoral Program in Applied Physics

Submitted to the Graduate School of
Pure and Applied Sciences
in Partial Fulfillment of the Requirements
for the Degree of Doctor of Philosophy in
Engineering

at the
University of Tsukuba

To my family

Abstract

Optical coherence tomography (OCT) as a promising biomedical imaging technology has been rapidly developed for many biological and medical fields. It shows many great benefits for the in vivo biological tissue imaging, such as non-invasiveness, relatively high resolution and deep penetration, etc. Among the various OCTs, the function extended OCTs, especially the multifunctional OCT (MF-OCT) is a promising imaging technology for the investigations of biological tissues, because it can provide several contrasts for detailed structures in tissues, including the two most important: components collagenous and vascular structures. However, there are very few studies on MF-OCT, and current MF-OCT is mostly limited to eye measurement but not suitable for the other high scattering tissues, such as skin.

Moreover, current single-functional OCTs for the investigation of birefringent tissues, such as skin, are not sufficient. For example, most PS-OCTs measure the cumulative phase retardations to detect the polarization property of skin, but it has been demonstrated to be not accurate for the tissue with non-uniform optic axis orientation. The other emerging functional OCT for birefringent tissue investigation is compression-based optical coherence elastography (OCE) technique, which can be used to measure the mechanical property of the birefringent tissue. But it is still not accurate enough as well because of the absence of lateral displacement measurement. Therefore, an advanced multifunctional OCT enabling multiple contrasts for the comprehensive assess of biological tissues with high scattering characteristics, such as skin, is proposed in this thesis. And with this advanced multifunctional OCT the simultaneous imaging for the optical and mechanical properties of the tissue can be obtained through once measurement. More importantly, a more accurate local birefringence imaging technology is applied in this MF-OCT instead of the phase retardation measuring method. And the lateral displacement and microstructural decorrelation (MSD) of the compressed tissue, which have never been reported before, are measured for the first time in this study as well.

This study was divided into two phases as follows:

First, a primary multifunctional OCT system is developed for skin tissue, which is capable of providing relatively accurate and high-quality multi-contrast images including local birefringence for in vivo human skin and degree of polarization uniformity images. Also, the optical and flow properties of the in vivo human skin tissue could be investigated by the multi-contrast imaging. In this stage, we investigate and demonstrate the simultaneous imaging of scattering intensity, angiography, local birefringence and degree of polarization uniformity for different *in vivo* human skin tissues, such as finger pad, outer-forearm and inner-forearm skins by the new multifunctional OCT. Unlike most common dermatological PS-OCTs using phase retardation imaging to investigate the collagen-related skin alteration (or its polarization property), local birefringence imaging enables more accurate evaluation of tissue polarization property, which is significantly associated with collagenous compositions in tissues.

Secondly, an advanced multifunctional OCT with elastography function is further developed. To this end, a new method of axial and in-plane lateral displacement measurements based on a multifunctional JM-

OCT system is first proposed. Based on that, the biomechanical properties imaging for biological tissues, including the lateral displacement and microstructural decorrelation maps, is achieved and it has never been reported in the previous researches of compression-OCE. Finally, the simultaneous imaging of optical and mechanical properties of biological tissue is realized by a new birefringence and biomechanics analysis method, i.e. compression-based PS-OCE, which enables simultaneously to measure two-dimensional birefringence tomography, scattering intensity OCT, spatial-resolved in-plane axial and lateral displacement, the coupled effect of out-of-plane displacement and microstructural decorrelation induced by micrometer-scale tissue compression. Particularly, it is found that the scattering OCT, birefringence, and biomechanical images revealed different tissue structures. Sole use of OCT, birefringence or biomechanical imaging is not sufficient to visualize all of the tissue structures. Additionally, the displacement imaging revealed that significant amount of lateral displacement is induced by axial compression. It implies that not only axial but also lateral displacement measurement is important for compression based OCE.

The final results suggest that the advanced multifunctional OCT based on the Jones matrix is capable of providing more comprehensive insight and information of the microstructures in biological tissue than the sole use of any single functional OCT or the previous multifunctional OCT. It would be expected as a powerful and helpful technology for the biomedical investigations and clinical care.

Contents

List of Figures

List of Tables

Chapter 1

Introduction

1.1 Overview of biomedical imaging technologies

1.2 Opportunities and challenges of optical coherence tomography (OCT)

1.3 Objectives of this research

1.4 Organization of this dissertation

References

1.1 Overview of biological imaging technologies

1.1.1 Biomedical imaging technologies

Biomedical imaging is used to detect and describe the features and properties of the structures and functions of biological tissues. Therefore, it is an important and useful tool, not only for clinical diagnosis and treatment, but also for biological and medical investigations and studies [1]. Various biomedical imaging technologies have been developed, some of them have been applied in clinical care and biomedical investigation, and some remain in the stage of laboratorial demonstration.

Among the imaging and measuring technologies commonly used in clinical care and biomedical investigation, optical coherence tomography (OCT) as an emerging biomedical imaging technique has been developed rapidly in the past several decades. OCT is essentially a low-coherence interferometry modality that provides noninvasive, high-resolution (micrometer scale), cross-sectional and three-dimensional imaging of biomedical tissues [2]. The principle of OCT is analogous to ultrasound imaging technique, the difference is that the OCT uses a near-infrared (NIR) light as a probing source to scan the sample but not the sound wave. Compared with some other biomedical imaging techniques commonly applied in clinical medicine, such as ultrasound imaging, X-ray computed tomography (CT), and magnetic resonance imaging (MRI), OCT possesses relatively higher axial resolution with few micrometers to around 10 μm [3]. Meanwhile, compared

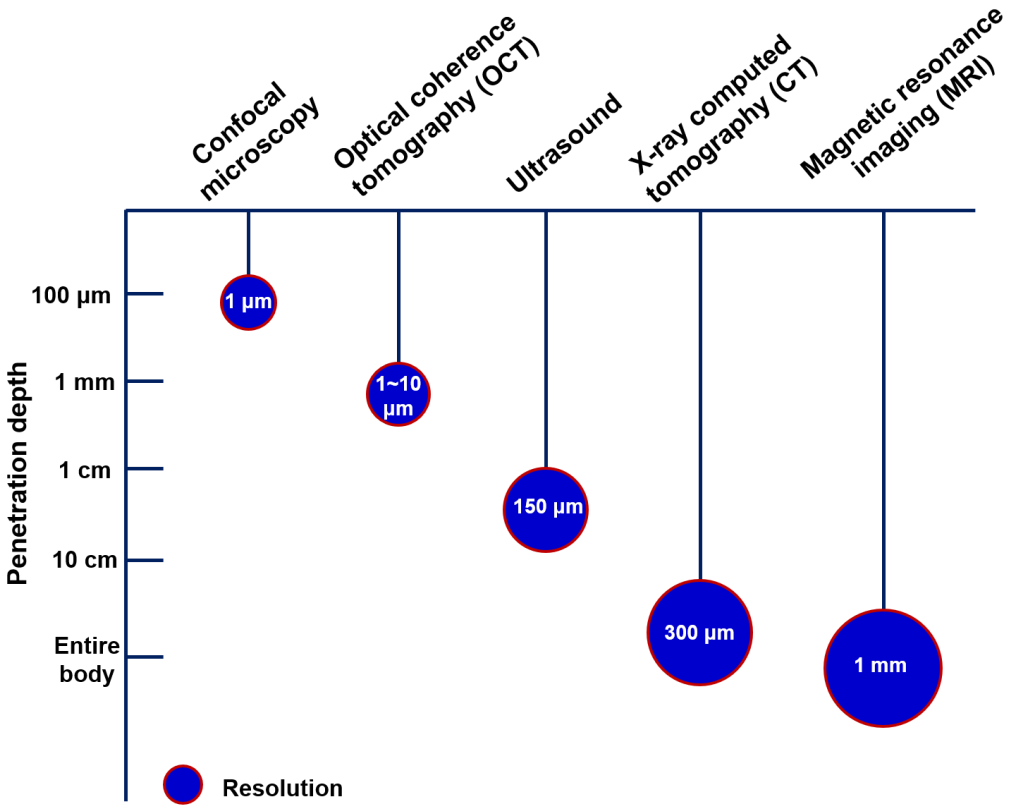

Figure 1.1: Comparison of resolution and penetration depth among OCT and other typical biological imaging technologies.

with some high-resolution imaging methods such as confocal microscopy, multiphoton microscopy, etc., OCT is capable to provide deeper tomographic imaging. Therefore, OCT can fill up the gap between these two types of biological imaging techniques and enables high-resolution and depth-resolved *in vivo* biological imaging (as shown in Fig. 1.1) [3]. In addition, because OCT uses a weak NIR light to illuminate the sample, it provides safer imaging of the human body than CT.

For the above reasons, OCT attracts the attention of many biomedical engineers and researchers and is regarded as a very promising imaging technology in many fields of biological and medical researches.

1.1.2 Investigation for biological tissue

For the biological tissue investigation, we are usually interested in two components in tissues. One is collagenous compositions as collagen is the most abundant structural protein in animals' bodies and the major component of extracellular matrix. In addition, it is responsible for the tensile strength of tissue and supports the organic activity [4]. Some studies have demonstrated that many pathological changes and injuries of biological tissue are associated with the abnormal conditions of collagenous structures in tissue [5–8]. The other important component in biological tissues is vascular structures, because they pervade every organ in organism and connect all the organ systems to nourish tissue and sustain life. Furthermore, the morphological and functional characteristics of the blood flow or blood vessels can reflect the physical condition of the organisms [9]. Therefore, measuring and assessing the properties of the collagenous compositions and vascular structures is very important to understand and investigate the characteristics of the normal and/or abnormal biological tissues.

1.1.3 Investigating approaches for main components of tissue

1.1.3.1 Assessing approaches for collagenous tissue

There are three common approaches for collagenous tissue assessment. One is histology-staining microscopic imaging [Figure 1.2(a) [10]]. Because of its low-cost and high-resolution merits, it is still the major method for collagenous tissue investigation in most studies. It can be used to observe the organizations of collagenous fibers such as arrangement and density. However, this method is only suitable for the in vitro measurement and usually costs a long measuring time. There are also two burgeoning methods, second harmonic generation (SHG) microscopy [Figure 1.2(c) [10]] and polarization-sensitive OCT (PS-OCT) [Figure 1.2(b) [10]]. Both of them enable the imaging for *in vivo* biological tissues, but it is not yet easily implemented for SHG microscopy in most cases [11]. With SHG image, the collagen fibrils orientation can be observed clearly. Although SHG microscope has an excellent resolution, its field of view (FOV) and penetration are limited as most high-resolution microscopies. While, as a function extended OCT, PS-OCT is quite suitable for *in vivo*

biological tissue imaging. Despite its resolution is not as high as histology and SHG microscopes, it has a relatively large FOV and deeper penetration. The PS-OCT can be used to visualize and assess the collagenous structures by measuring the polarization properties of tissue, such as birefringence and degree of polarization uniformity.

Figure 1.2 [10] shows the images from a same sample, which is an *ex vivo* rat back skin, by the three different imaging techniques mentioned above for comparison. From this figure, we can see that these three images tested different characteristics of the collagenous structures in tissue by different contrast mechanisms. The histological microscopic image with Masson's trichrome staining [Figure 1.2(a)] showed the arrangement and density of the collagen fibers in different layers of the sample. The SHG image [Figure 1.2(c)] revealed the detailed information of the collagen fibrils, such as the distribution and orientation of the collagen fibrils, in a certain small location of the sample. Moreover, the density of the collagen fibrils in a local area of sample can be visualized as well as the histological image. While, in the PS-OCT image [Figure 1.2(b)], the bulk-collagenous structures in the sample can be assessed with its particular optical property – birefringence (or phase retardation). The magnitude of the birefringence (or phase retardation) displayed in PS-OCT image indicates the collagen content of the tissues. Thus, all these three approaches can be utilized to visualize and measure the collagenous tissues, but they evaluate different characteristics of the collagenous structures for concrete investigating purpose.

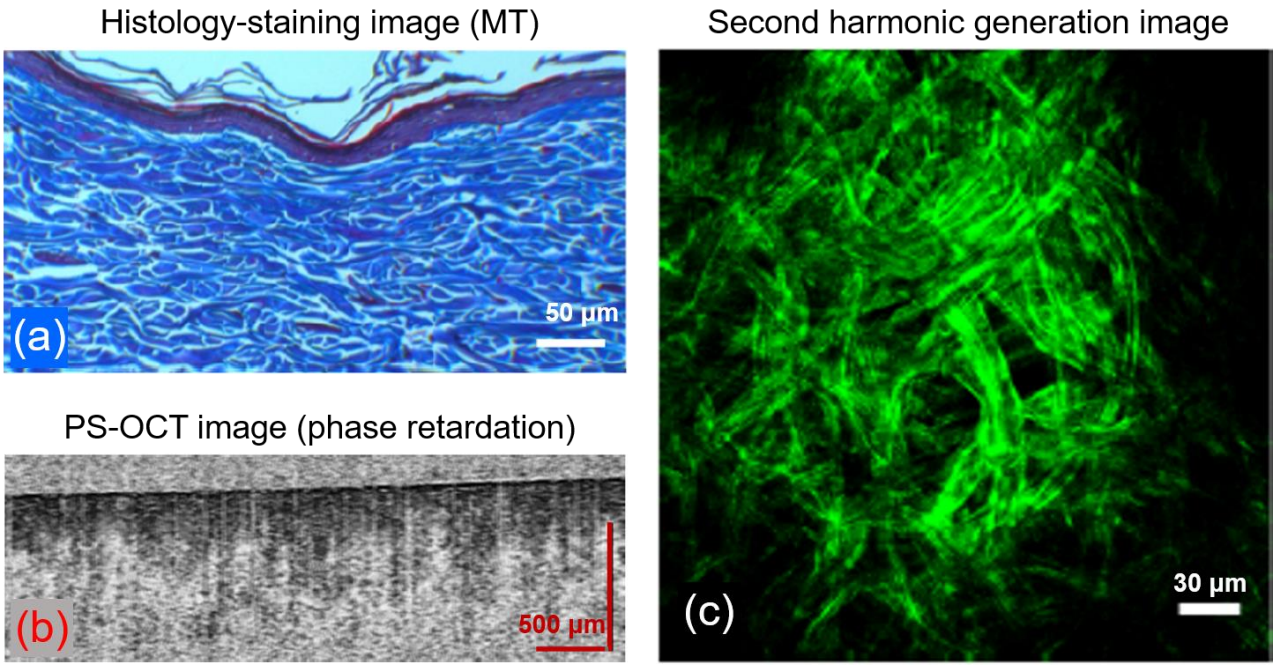

Figure 1.2: The measurements of an *ex vivo* rat back skin by different imaging approaches. (a) is Histological image with Masson's trichrome (MT) staining, (b) is phase retardation image obtained by PS-OCT, and (c) is second harmonic generation (SHG) image [10].

Additionally, tissue biomechanics is relevant to the collagenous compositions of the biological tissue, so the mechanical property is one of the important information for collagenous tissue investigation as well.

And this property also can be measured by an OCT based elastography, which is also regarded as optical coherence elastography (OCE). And this technology has been demonstrated to be helpful for the anomalous tissue evaluation such as shown in figure 1.3 [12]. In the figure 1.3 [12], we can see that the scar and tumor tissues, which are strongly associated with the abnormal collagenous compositions [8,13–16], present a significantly different stiffness from the normal tissues in the OCE images.

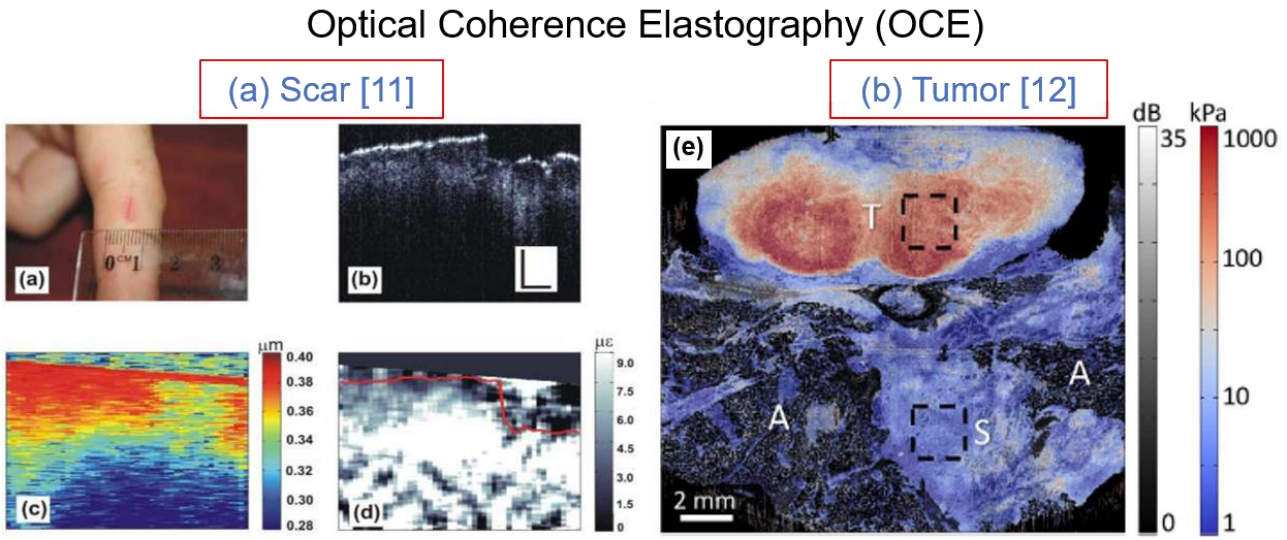

Figure 1.3: The biomechanical imaging of abnormal tissues with collagenous composition changes by OCE. (a) is OCT and OCE tomographic images of finger-skin tissue with scar. (b) is *en face* OCE image of tumor tissue in human breast [11].

1.1.3.2 Measuring methods for vascular structures

For the study of the vascular structures, there are three angiography technologies based on different imaging methods, computed tomography angiography (CTA), magnetic resonance angiography (MRA) and optical coherence tomography angiography (OCTA). As it is mentioned in the first subsection (section 1.1.1), the penetration of OCT is lower than CT and MRI. And currently, the measurable location of OCTA is still limited. But, OCTA has much higher resolution and faster measurement speed than CTA and MRA. Moreover, it has the smallest damage and physical discomfort, such as radiation injury and noise stimulation, among these three methods. According to the individual superiorities of these three technologies, CTA and MRA are suitable for the large vessels of whole-body measurement, but they are hard to visualize the tiny blood vessels and blood capillaries at present. While, the OCTA has a better performance for the investigations of tiny vascular structures and blood capillaries in local tissues. The different characteristics of these three angiography techniques can be seen clearly in the figure 1.4 [17].

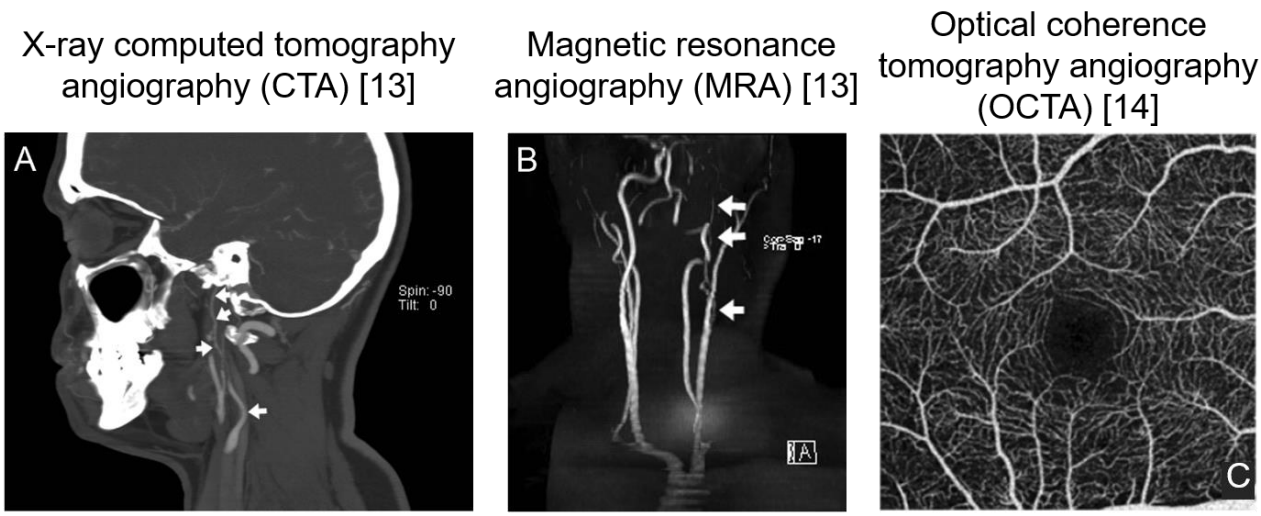

Figure 1.4: The comparison of different imaging technologies for vascular structures. A and B are the X-ray computed tomography angiography (CTA) and magnetic resonance angiography (MRA) of the human carotid artery, respectively. C is an optical coherence tomography angiography (OCTA) of a human eye [12].

1.2 Opportunities and challenges of optical coherence tomography (OCT)

Through the above brief review of the investigating methods and measuring means for biological tissues, we can find OCT would be a helpful and powerful tool for biological and medical investigations and further for the clinical applications as its quite a lot of benefits to the imaging for biological tissues. Compared to the other investigating methods for both collagen and vascular structures, the advantages and disadvantages of OCT can be summarized as follows.

- **Advantages**

  1. OCT enables a fast 3D morphological imaging for *in vivo* biological tissues with submillimeter resolution.

  2. OCT is also capable to provide evaluations of various properties of biological tissue including optical, blood flow and biomechanical properties by different modalities. (E.g., PS-OCT: birefringence and degree of polarization uniformity, OCTA: blood flow, OCE: elasticity or stiffness).

- **Disadvantages**

  1. Scarce OCT provides comprehensive information of biological tissue with once measurement.

2. Most PS-OCTs' measurement (phase retardation) is not accurate for tissue with non-uniform optic-axis orientation (e.g. skin).

3. Current compression-OCE is not accurate enough due to the absence of lateral displacement measurement.

Although OCT has achieved great success in the studies of many fields, as it has the ability of providing not only for morphological imaging but also evaluations of various properties for *in vivo* biological tissues. Currently, the OCT technology still has some limitations. For example, there is no OCT can provide comprehensive information including all the above motioned properties of biological tissues with once measurement. In addition, except for few ophthalmologic PS-OCTs, most PS-OCT technologies measure the cumulative phase retardation of the probing beams in sample to evaluate the polarization property of tissues. However, this method has been discussed to be not accurate for the biological tissues with non-uniform optic-axis orientations, such as skin [18–20]. At last, as a successful OCE technique, compression-OCE is not accurate enough as well, because of the absence of lateral displacement measurement. These shortcomings limit the measuring accuracy and clinical applications of OCT except for ophthalmology. Consequently, to overcome these disadvantages and improve the reliability and availability of the measurement are still challenges for OCT technology.

1.3 Objectives of this research

Based on the above background, the objective of this research is to further develop the availability and universality of OCT by improving its performance and extending its functions. With this purpose, this study was divided into two phases in detail.

First, I planned to develop a primary multifunctional OCT system for dermatology based on Jones matrix theory, which is capable of providing relatively accurate and high-quality multi-contrast images including local birefringence and degree of polarization uniformity measurement, because skin is the largest organ of human body and suitable for OCTs' measurement. Then, the optical and flow properties of the *in vivo* human skin tissue would be investigated by the multi-contrast imaging.

In the second stage, an advanced multifunctional OCT with elastography function is further proposed. The goal of this stage is to perform a biomechanical properties imaging for the biological tissues including the lateral displacement and microstructural decorrelation (MSD) maps, which are never reported in the previous researches of compression-OCE. Finally, the simultaneous imaging of optical and mechanical properties for biological tissues by the advanced multifunctional OCT would be demonstrated.

With this kind of advanced multifunctional OCT, the comprehensive and exact observation and assessment would be expected.

1.4 Organization of this dissertation

In this section, the outline of this dissertation entitled “Development of advanced multifunctional optical coherence tomography based on Jones matrix theory for biological tissue investigation” is explained.

Chapter 1 first shows the background overview of this research. Then, the opportunities and challenges of OCT is discussed in the following section. In the last part of this chapter, the objective of the research developing an advanced multifunctional OCT system including elastography function is proposed, and finally, the thesis outline is presented.

Chapter 2 first retrospects the development history and various technologies of OCT. In the flowing, the key parameters affecting OCT performance is introduced. Further, we move to the application of OCT technology and discuss its potential of imaging some specific biological tissues in the medical field-especially, in ophthalmology field as well as clinical dermatology follow up.

In chapter 3, the general principle of JM-OCT and the polarization properties of biological tissue, as well as the implementation of JM-OCT is first introduced. Based on the knowledge in the JM-OCT, the theory and imaging properties for JM-MF-OCT developed in this study are subsequently discussed. In the end, the advantages and potential applications for the proposed JM-MF-OCT are further explained.

Chapter 4 mainly focuses on the study of dermatological imaging by JM-MF-OCT system, where the experimental details of system establishing, parameter test, and the derived imaging of *in-vivo* skin by JM-MF-OCT system is systematically investigated and presented. Particularly, a more accurate and quantitative evaluation of tissue property is successfully achieved by the birefringence imaging in the proposed multifunctional JM-OCT system in this study. Additionally, the remaining limitations in the JM-MF-OCT system and a few reported strategies to these limitations are also briefly discussed.

Chapter 5 investigates the upgrade of the JM-MF-OCT system in order to the limitations of the OCT system discussed in chapter 3. In particular, the improvement of imaging depth range is mainly studied. By changing the light source and redesigning the sampling points, the imaging depth range of the dermatological multi-functional JM-OCT is ultimately enhanced. Relative to the one used in chapter 3, around 1-mm deeper imaging without causing additional degradation in images is successfully achieved.

In chapter 6, based on multifunctional JM-OCT system discussed in the previous two chapters, a new Jones-matrix-based PS-OCT system for simultaneous imaging of birefringence and biomechanical properties of tissue is developed and studied. It is equipped with a tissue compression probe and could provide birefringence tomography, scattering intensity, depth-resolved in-plane axial and lateral displacements, and microstructural decorrelation maps of a biological tissue simultaneously. This method makes use of OCT images of a tissue obtained from JM-OCT under two different compressive conditions. By means of complex correlation maps computed from these two OCT images, depth-resolved axial and lateral displacement maps of the tissue are obtained. Moreover, a depth-resolved MSD map is also achievable. The combination of the

birefringence and biomechanical images enables more comprehensive insight and information of the microstructures in tissue than the sole use of PS-OCT or OCE. It would provide more degree of freedom in the investigation of *in vivo* tissues.

Chapter 7 summarizes the research work presented in this dissertation. Also, the outlook of further research on the dermatological imaging by OCT technology as well as future clinic application of OCT is discussed.

References

1. P. Morris, *Biomedical Imaging: Applications and Advances* (Elsevier, 2014).

2. D. Huang, E. A. Swanson, C. P. Lin, J. S. Schuman, W. G. Stinson, W. Chang, M. R. Hee, T. Flotte, K. Gregory, C. A. Puliafito, and J. G. Fujimoto, "Optical Coherence Tomography," Science **254**(5035), 1178–1181 (1991).

3. R. Liang, ed., *Biomedical Optical Imaging Technologies: Design and Applications*, Biological and Medical Physics, Biomedical Engineering (Springer-Verlag, 2013).

4. E. Leikina, M. V. Mertts, N. Kuznetsova, and S. Leikin, "Type I collagen is thermally unstable at body temperature," Proc. Natl. Acad. Sci. **99**(3), 1314–1318 (2002).

5. D. C. Adams, M. V. Szabari, D. Lagares, A. F. McCrossan, L. P. Hariri, A. M. Tager, and M. J. Suter, "Assessing the progression of systemic sclerosis by monitoring the tissue optic axis using PS-OCT," Sci. Rep. **10**(1), 1–10 (2020).

6. S. D. Giattina, B. K. Courtney, P. R. Herz, M. Harman, S. Shortkroff, D. L. Stamper, B. Liu, J. G. Fujimoto, and M. E. Brezinski, "Assessment of coronary plaque collagen with polarization sensitive optical coherence tomography (PS-OCT)," Int. J. Cardiol. **107**(3), 400–409 (2006).

7. S. Sakai, M. Yamanari, A. Miyazawa, M. Matsumoto, N. Nakagawa, T. Sugawara, K. Kawabata, T. Yatagai, and Y. Yasuno, "In vivo Three-Dimensional Birefringence Analysis Shows Collagen Differences between Young and Old Photo-Aged Human Skin," J. Invest. Dermatol. **128**(7), 1641–1647 (2008).

8. W. C. Y. Lo, M. Villiger, A. Golberg, G. F. Broelsch, S. Khan, C. G. Lian, W. G. Austen, M. Yarmush, and B. E. Bouma, "Longitudinal, 3D Imaging of Collagen Remodeling in Murine Hypertrophic Scars In Vivo Using Polarization-Sensitive Optical Frequency Domain Imaging," J. Invest. Dermatol. **136**(1), 84–92 (2016).

9. R. S. Udan, J. C. Culver, and M. E. Dickinson, "Understanding vascular development," WIREs Dev. Biol. **2**(3), 327–346 (2013).

10. V.-H. Le, S. Lee, B. Kim, Y. Yoon, C. J. Yoon, W. K. Chung, and K. H. Kim, "Correlation between polarization sensitive optical coherence tomography and second harmonic generation microscopy in skin," Biomed. Opt. Express **6**(7), 2542–2551 (2015).

11. F. S. Pavone and P. J. Campagnola, *Second Harmonic Generation Imaging* (CRC Press, 2013).

12. B. F. Kennedy, T. R. Hillman, R. A. McLaughlin, B. C. Quirk, and D. D. Sampson, "In vivo dynamic optical coherence elastography using a ring actuator," Opt. Express **17**(24), 21762–21772 (2009).

13. K. Cw and B. Gs, "Structure of the collagen nodule from hypertrophic scars and keloids.," Scan. Electron Microsc. (Pt 3), 371–376 (1981).

14. J. W. Madden and E. E. Peacock, "Studies on the biology of collagen during wound healing. 3. Dynamic metabolism of scar collagen and remodeling of dermal wounds.," Ann. Surg. **174**(3), 511–520 (1971).

15. M. R. Ng and J. S. Brugge, "A Stiff Blow from the Stroma: Collagen Crosslinking Drives Tumor Progression," Cancer Cell **16**(6), 455–457 (2009).

16. P. P. Provenzano, D. R. Inman, K. W. Eliceiri, J. G. Knittel, L. Yan, C. T. Rueden, J. G. White, and P. J. Keely, "Collagen density promotes mammary tumor initiation and progression," BMC Med. **6**(1), 11 (2008).

17. M. Mozayan and C. Sexton, "Imaging of carotid artery dissection," J. Community Hosp. Intern. Med. Perspect. **2**(2), 18645 (2012).

18. C. Fan and G. Yao, "Mapping local retardance in birefringent samples using polarization sensitive optical coherence tomography," Opt. Lett. **37**(9), 1415–1417 (2012).

19. D. Kasaragod, S. Makita, S. Fukuda, S. Beheregaray, T. Oshika, and Y. Yasuno, "Bayesian maximum likelihood estimator of phase retardation for quantitative polarization-sensitive optical coherence tomography," Opt. Express **22**(13), 16472–16492 (2014).

20. S. Sugiyama, Y.-J. Hong, D. Kasaragod, S. Makita, S. Uematsu, Y. Ikuno, M. Miura, and Y. Yasuno, "Birefringence imaging of posterior eye by multi-functional Jones matrix optical coherence tomography," Biomed. Opt. Express **6**(12), 4951–4974 (2015).

Chapter 2

Basics of OCT imaging technology

2.1 Introduction

Optical coherence tomography (OCT) is essentially a low-coherence interferometry modality that provides noninvasive, and fast imaging with high-resolution (micrometer scale) of internal microstructures for biomedical tissues [1]. It uses a near-infrared ray (NIR) as a light source and applies the Michelson interference principle to measure the backscattered lights from the tissue layers, then reconstructs the cross-sectional image of the tissue.

When an OCT measures a sample, the depth imaging of the sample is resolved with the coherence gating, which is accomplished by interfering the lights from a variable reference arm and a sample arm of the interferometer. During the measurement, when the optical path lengths of the reference and the sample arms match within one coherence length of the light source, they interfere with each other and generate the interference fringes. If the reference mirror moves along the optical axis, the interference signals corresponding to the different positions in the depth of the sample can be produced. It is termed as A-line. The intensities of the interference signals can be expressed as

$$\begin{aligned} I_d(\tau) &= \int_{-\infty}^{\infty} |E_s(t) + E_r(t-\tau)|^2 dt \\ &= \int_{-\infty}^{\infty} |E_s(t)|^2 dt + \int_{-\infty}^{\infty} |E_s(t)|^2 dt + \int_{-\infty}^{\infty} E_s(t) {E_r}^*(t-\tau)\, dt + c.c. \\ &= I_s + I_r + 2Re\left\{\int_{-\infty}^{\infty} E_s(t) {E_r}^*(t-\tau) dt\right\} \quad (1), \end{aligned}$$

where the E_s and E_r respectively represent the electric field intensities of the lights returning from the sample and the reference arms, the I_s and I_r express the intensities of the lights from the sample and the reference arms, respectively, t is any time points during the measurement, τ is the time delay from the reference mirror, and $c.c.$ is the complex conjugate of the third term in the second row of the equation [2]. This equation consists of two DC components, I_s and I_r, and one AC component modulated by the mismatched optical pathlengths of the reference and sample arms. The AC term changed with a time-delay controlled by the reference arm is the measured signal in OCT.

If we use a galvanometric mirror make the A-line transversely scan the sample along the lateral axis, a two-dimensional (2D) image, which is called as B-scan, can be obtained. Further, when we move the B-scan along the y-axis by a pair of galvanometric mirrors, a three-dimensional (3D) image could be achieved as well.

2.2 Development of OCT

The first OCT emerged in 1991, invented by Fujimoto's group, which first obtained the image of *ex vivo* porcine eye successfully [1]. In the following decades, with the advancements of the light source, fiber optics, optical detectors, and other optical components, OCT has been developed rapidly. Retrospect to the development of OCT, in accordance with the different approaches of interference fringes generation for obtaining the depth information of the sample, there are two main categories of OCT. One is time-domain OCT (TD-OCT) [2–4], the other is Fourier-domain OCT (FD-OCT) [5]. While, according to the different configurations of the light source and detector, FD-OCT is further divided into two categories: spectral-domain OCT (SD-OCT) [6–9] and swept-source OCT (SS-OCT) [5,10,11].

2.2.1 TD-OCT

TD-OCT is the first generation of OCT, which was first demonstrated in 1991 [1]. TD-OCT is built on a low-coherence broadband light source (e.g., a super luminescent diode (SLD) or white light). Figure 2.1 shows an example of the typical TD-OCT schematic. The laser from the light source is separated by a beam splitter (or a 2 × 2 fiber coupler). The two beams go through the reference and sample arms and then illuminate a reference mirror and the sample, respectively. The reflected lights from the two arms are recombined in the beam splitter (or the coupler). And the interference signal corresponding to each position of the sample in depth can be produced when the optical path lengths (OPLs) of the two arms are matched with each other within a coherent

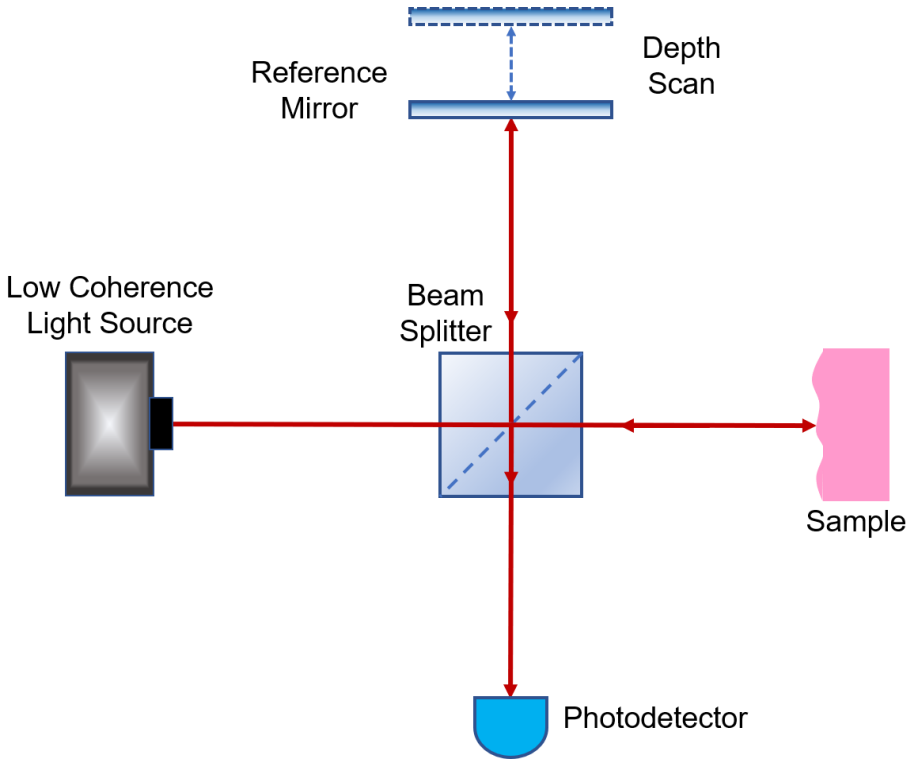

Figure 2.1: Schematic of typical TD-OCT.

length of the light source. In other words, the TD-OCT uses a scanning mirror to detect the depth information of sample. A cross-sectional imaging for human eye by TD-OCT is shown in Fig. 2.2 [1] as an example.

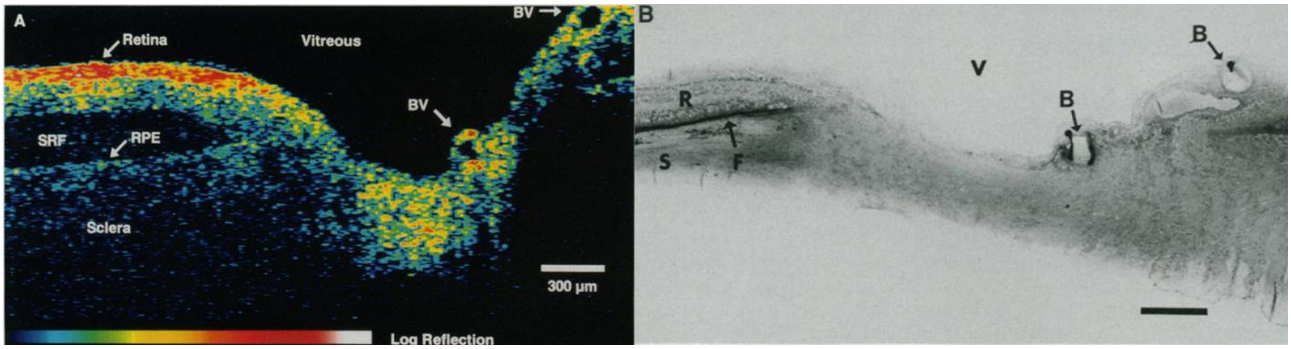

Figure 2.2: Optical coherence tomography of human retina and optic disk in vitro (A) and histologic section of the same specimen (B) [1].

Since the depth information of the sample is acquired by scanning the reference mirror in TD-OCT, the measurement speed of TD-OCT is very slow [12–14], especially for 2D and 3D imaging. It is too hard to perform 3D imaging by TD-OCT, because of its low measurement speed that limited by the mechanical scanning modality. The measurement speed is very important for *in vivo* biological tissue imaging in medical applications. In particular, it is difficult to keep *in vivo* tissues being stable for a long time during the clinical examinations, and the long-time measurement might make the patients uncomfortable. Furthermore, the SNR and sensitivity of TD-OCT are relatively low as well because the optical power of the sample arm collected by the point detector in TD-OCT is only concentrated at the signal position, which corresponds to a narrow temporary coherence gate [14–16]. These two parameters are quite important for the biological tissue imaging as well.

2.2.2 FD-OCT

To overcome the limitations of TD-OCT, the second generation of OCT, Fourier domain (or frequency domain) OCT (FD-OCT), then was developed in 1995 [6]. Different from TD-OCT, it uses different wavelengths to detect the depth information of sample. Without the mechanical scan of the reference arm, the speed of FD-OCT was significantly improved, that enables the 3D imaging in OCT. Moreover, the sensitivity of FD-OCT is much higher than TD-OCT.

The FD-OCT has gradually replaced the TD-OCT in recent years. The important reason is that it does not need the mechanical optical path scanning in the reference arm to achieve the axial depth scanning. Therefore, the imaging speed of FD-OCT can be greatly improved, and thus the SNR and sensitivity are enhanced as well [5,13,15,17]. Different from TD-OCT, in FD-OCT the reference mirror is fixed, and the time-domain signals in axial direction (corresponding to each depth position of sample) are transformed into

Fourier-domain (a power spectrum), i.e. each longitudinal (depth) scan corresponds to an interference spectrum containing all the depth information of the sample. Then, according to the Wiener-Khintchine theorem for the Fourier relation between the autocorrelation function and the spectral power density of a wide-sense-stationary random process, the depth-related information of the sample then can be obtained immediately from the power spectrum by Fourier transform.[18,19] Based on the different implementing methods and system configurations, FD-OCT is further classified into SD-OCT and SS-OCT.

2.2.2.1 SD-OCT

SD-OCT is one subtype of FD-OCT. A simplified SD-OCT scheme is shown in Fig. 2.3 as an example. In SD-OCT, the broadband low-coherence light source is usually a Superluminescent diode (SLD) or a broadband pulse laser such as Ti: Sapphire laser. A typical center wavelength of SD-OCT light source is around 830 nm or 1000 nm with a bandwidth that is from about 50 to 100 nm. However, if a 1000-nm (or longer wavelength) light source is used in SD-OCT, correspondingly, a relatively high-cost line sensor (such as InGaAs sensor) has to be utilized. Consequently, the light source with a center wavelength over 1000 nm is not extensively applied for SD-OCT.

Similar to TD-OCT, the laser from the light source is divided into two beams by a coupler. One part is the reference beam, and the other part is the probing beam. These two beams respectively pass through the reference and sample arms, and the beams reflected from the reference mirror and the sample are recombined and form the interference signals at the coupler. As mentioned above, instead of the scanning reference mirror in TD-OCT, the spectral interference signals corresponding to the backscattered lights of all depths are

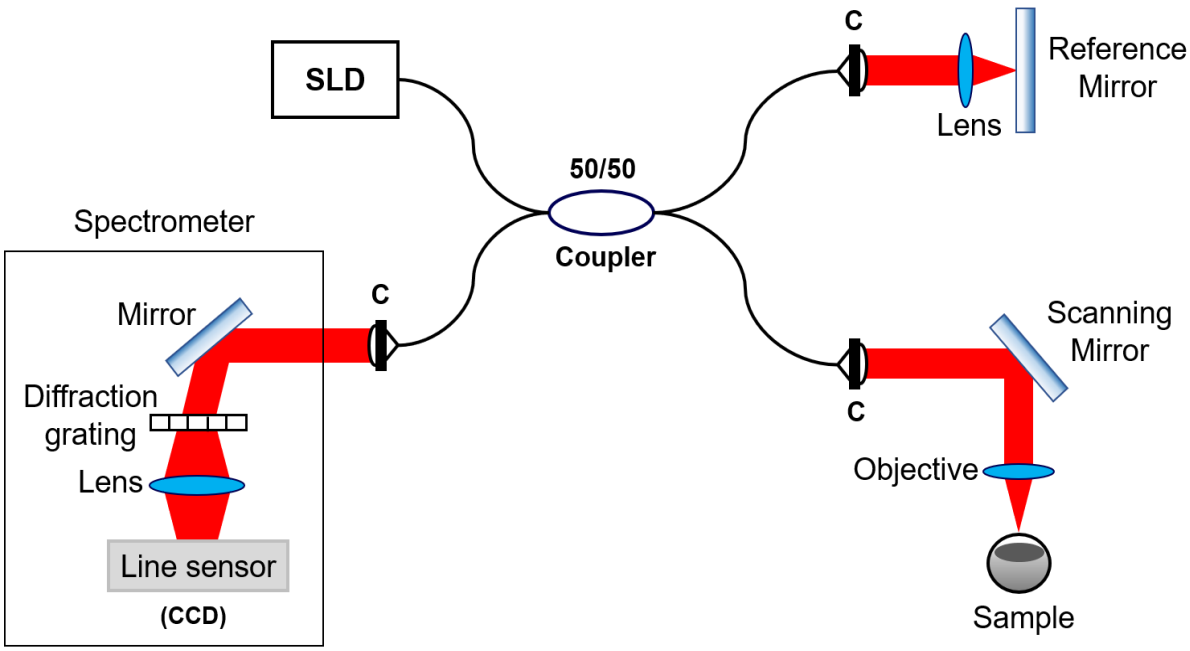

Figure 2.3: Schematic of SD-OCT. SLD: Superluminescent diode; C: collimator; CCD: charge coupled device camera.

generated at the coupler with only one axial scan. The spectrum of these depth-resolved interference signals is dispersed by a diffraction grating and simultaneously detected by a high-speed line sensor, such as CCD [7,18,20]. The depth profile (A-scan) is then obtained by the inverse Fourier transformation of the detected spectrum-resolved interference signals. By using a transversal scanning mirror or two orthogonal galvanometric mirrors, 2D (B-scan) or 3D (volumetric) imaging can be performed.

It has been demonstrated that, the imaging speed and sensitivity of SD-OCT imaging have been significantly improved compared to TD-OCT [5,13,14]. In addition, the imaging depth range and resolution are also can be improved in SD-OCT [9,21]. A comparison of TD-OCT and SD-OCT for ophthalmology imaging are shown in Fig. 2.4 [22]. It shows that the image of human eye tissue obtained by SD-OCT (Fig. 2.4(a)) has less noise and higher sensitivity than that obtained by TD-OCT (Fig. 2.4(b)). Thus, SD-OCT shows a relatively high quality and high contrast imaging for the tissue compared to TD-OCT. The A-scan rate of the first generation SD-OCT is 40 kHz, and so far it has been improved to 300 - 500 kHz (500 kHz can be achieved by multiple line sensors as well) [16,23–25]. The A-scan rate of a common SD-OCT is hundreds times faster than that of TD-OCT [24,26]. It enables the imaging depth range and resolution of OCT to be significantly improved.

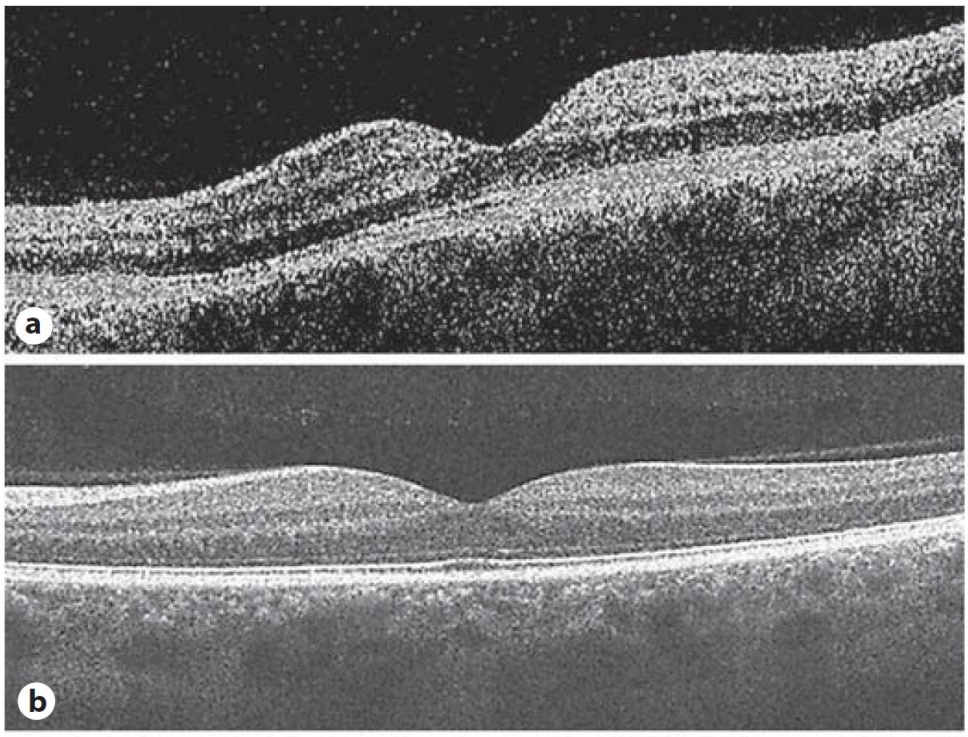

Figure 2.4: Comparison of OCT images from the same healthy eye by (a) TD-OCT and (b) SD-OCT [22].

2.2.2.2 SS-OCT

SS-OCT is another subtype of FD-OCT, which detects the interference signals in frequency-domain and obtains the depth information by Fourier transformation as well. However, the spectrally resolved interference signals generating and detecting methods of SS-OCT are different from SD-OCT based on their different configurations. As shown in Fig. 2.5, SS-OCT utilizes a broadband rapid wavelength swept light source instead of SLD to scan the sample and reference mirror and the returned beams from two arms are mutually interfered at the coupler. The center wavelength of SS-OCT source is commonly longer than 1000 nm, such as 1060 nm, 1310 nm with a bandwidth wider than 100 nm. Because the longer wavelength light source has deeper penetration in tissue, the SS-OCT is usually used for deeper tissues (e. g. posterior eye) or thicker tissues (e.g. skin). The reference mirror in SS-OCT is also fixed as it is in SD-OCT, but the OCT spectrum is not dispersed before the detector in SS-OCT. It is because SS-OCT uses a single high-speed point detector to sequentially acquire the time-encoded frequency components of the OCT spectrum corresponding to the orderly wavelength scanning for sample. The depth profile (A-scan) is thus obtained from Fourier transformation of these time-encoded spectrally resolved interference signals acquired by detector. All depths information of sample along axial scanning (A-scan) are obtained in parallel from the recorded OCT spectrum [16,18,19].

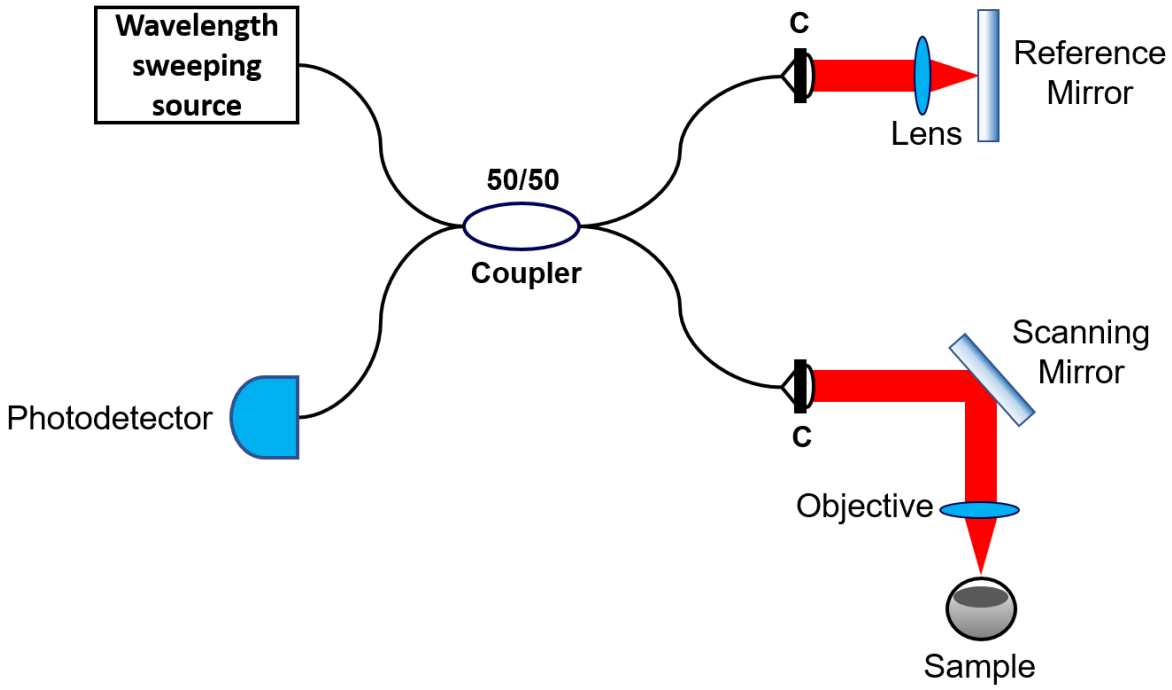

Figure 2.5: A simplified SS-OCT schematic. C: collimator.

The acquisition speed of line sensor, which consists of array photodetectors, limits the imaging speed and sensitivity of SD-OCT. Whereas, SS-OCT uses a rapid wavelength sweeping source and a single photodetector with subsequent A/D conversion. Thus, the imaging speed and sensitivity of SS-OCT is higher than SD-OCT. Especially for 3D imaging, the volumetric acquisition speed of SS-OCT is much faster than that of SD-OCT [16,23,24]. Figure 2.6 compares the images of the same *in vivo* human eye tissue obtained by

SS-OCT (Fig. 2.6 (a)) and SD-OCT (Fig. 2.6 (b)), respectively [27]. It can be seen that the SS-OCT with 1060-nm center wavelength possesses larger imaging depth range than the SD-OCT with 840-nm center wavelength. And the contrast of the tissue in SS-OCT image is much stronger than that in SD-OCT image, especially for the deeper tissue. In addition, the boundaries of each tissue layers shown in SS-OCT image is clearer than those in SD-OCT image.

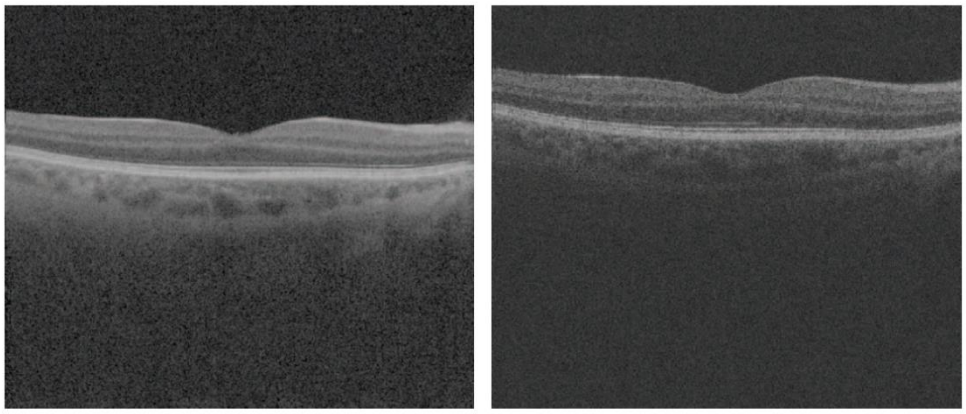

Figure 2.6: Comparison of imaging for *in vivo* human eye tissue by (a) SS-OCT and (b) SD-OCT [27].

To briefly outline the shortcomings of SS-OCT, one is a high cost from the used light source. SS-OCT typically requires a narrow linewidth, high speed, and wavelength sweeping laser that are very pricey. In addition, the axial resolution of SS-OCT is not high enough because of its long-center-wavelength source. However, the long-center-wavelength swept source is capable of providing deeper penetration as well. Hence, selecting an appropriate light source and FD-OCT configuration should balance the resolution and imaging depth range according to the measured object. The basic performance parameters of each type of OCT are listed in Table 2.1 for comparison. The parameters in Table 2.1 will be explained detailly in the Section 2.3. As shown in Table 2.1, current FD-OCT possesses much higher speed and sensitivity than TD-OCT. In addition, the resolution of FD-OCT is relatively high as well. Therefore, FD-OCT is regarded as a promising

Table 2.1 Performance of TD-OCT, SD-OCT, and SS-OCT.

Feature	TD-OCT	FD-OCT	
		SD-OCT	SS-OCT
Light source	SLD	Broadband SLD	Swept source
center wavelength	800nm	800 ~ 1000nm	> 1000nm
A-scan rate	2k – 8kHz	300k – 500kHz	100k – 6.7MHz
Sensitivity (Dynamic rang)	40 – 60 dB	> 100dB	> 100dB (w/o roll-off)
Axial resolution (in tissue)	around 10 μm	< 10 μm	5 – 15 μm

imaging technology for biological tissue investigation. And SS-OCT is more suitable for deeper and thicker tissue measurement such as skin tissue.

2.2.3 Extension of OCT

In the above two sections (2.2.1, 2.2.2), the primary types of OCT have been introduced. However, the traditional OCT mainly provides the cross-sectional structure profile of the tissue by mapping out the intensity of the reflectivity. The information from the traditional OCT is not always enough for biomedical and clinical applications. Considering the biomedical and clinical requirements to improve the practicability of OCT, based on these standard OCT modalities, some function extended OCTs were developed in recent years as well. The functional extended OCTs, such as polarization-sensitive OCT (PS-OCT) [28,29], Doppler OCT (DOCT) [30,31], OCT angiography (OCTA) [32,33] and so on, provide extra useful and helpful information for biological and medical investigation.

2.2.3.1 PS-OCT

As early as 1992, the polarization sensitive low-coherence interferometer (PS-LCI) was demonstrated, which enables the characterization of sample birefringence by phase-retardation measurements [34]. Soon after, PS-OCT was developed by de Boer et al [29,35] and was advanced to 2D and 3D imaging of birefringent materials [36,37]. Because PS-OCT is capable of providing the specific contrast (birefringence) of biological tissues and the birefringence has been demonstrated as an important property of biological tissues, PS-OCT is regarded as a promising imaging technique for various fields.

In biological tissues, there are many factors that can affect the polarization state of light, such as microscopic fibrous structures, molecular properties and concentration, the chemical composition of the molecules and so on. This property of biological tissues is referred to as birefringence. When a polarized light goes into a biological tissue that possesses birefringence property, the light is decomposed into two orthogonally polarization states, and these two polarization states propagate at different speeds in the tissue. One polarization state of the incident beam occurs a phase-retardation relative to the other one, and this phase-retardation is dependent on the difference of the refractive index for the two polarization states and the thickness of the tissue. Additionally, sometimes the attenuation of the incident beam in the tissue is different depending on its polarization state. Thus, the optic-axis, orientation, phase-retardation, and diattenuation were determined as the polarization properties of biological tissues for PS-OCT imaging. Then, by measuring these four polarization properties of tissues, the PS-OCT is capable of providing enhanced contrast of tissues' specific properties and microscopic structure alterations.

PS-OCT essentially utilizes a polarized light to detect the polarization states changes by tissues, thereby acquires the information of the polarization properties of the tissue. The polarization state can be represented by two different forms, Jones vector and Stokes vector (in a Poincare's Sphere). The Jones vector only can be used to describe the completely polarized states. However, the Stokes vector can be used to describe not only completely polarized light, but also partially polarized and depolarized lights. Accordingly, the actions of matters on light, including optical components and any scattering materials, can be presented by a Jones matrix or a Mueller matrix. Corresponding to different mathematical formalisms of the expressions for the interaction between the polarized light and matters, there are mainly two different types of PS-OCT, one is Jones-matrix-based PS-OCT (JM-OCT), the other is Stokes-vector and Mueller-matrix-based PS-OCT [38–41]. Furthermore, to make it suit for the clinical application in the future, fiber-based PS-OCT, which is built by applying the single-mode fiber, has been developed [42]. An example of *in vivo* phase retardation imaging for optic nerve head (ONH) of myopic human eye by PS-OCT is shown in Fig. 2.7 [11]. The characteristic changes of phase retardation of the lamina cribrosa in the ONH can be observed by PS-OCT imaging, which is difficult to be discriminated in the traditional OCT image.

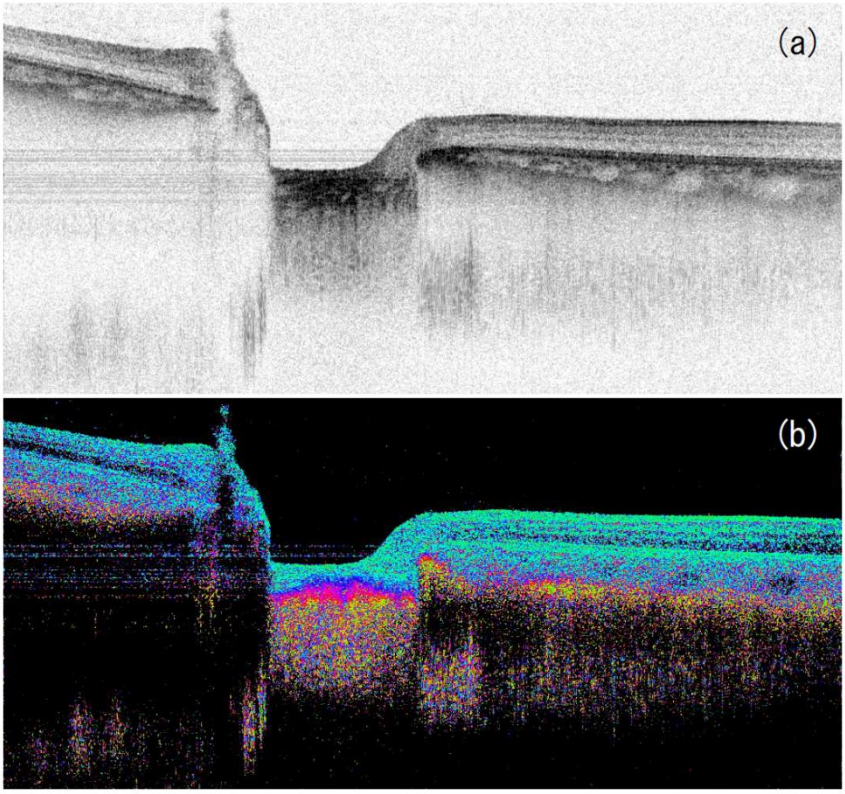

Figure 2.7: *In* vivo imaging for human eye by PS-OCT. (a) Intensity tomography of ONH. (b) Phase retardation images corresponding to (a) [11].

2.2.3.2 Doppler OCT

With the development of low-coherence interferometer (LCI) and OCT, as well as the first demonstration of using the Doppler technique in LCI to obtain the fluid velocity data [43], and then DOCT emerged immediately.

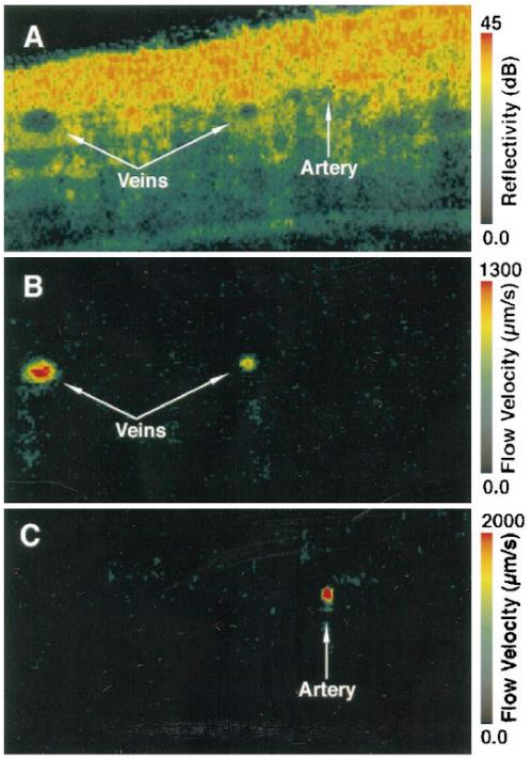

Figure 2.8: DOCT images of *in vivo* blood flow in rodent skin. (A) color-coded tomographic structural image. (B) color-coded velocity image of venous blood flow (into the page). (C) color-coded velocity image of arterial blood flow.

In 1997, by applying the Doppler frequency shifted approach in OCT [44], the first Doppler OCT (DOCT) was developed to achieve the tomographic imaging of *in vivo* blood flow velocity in rodent skin (Fig. 2.8) [45].

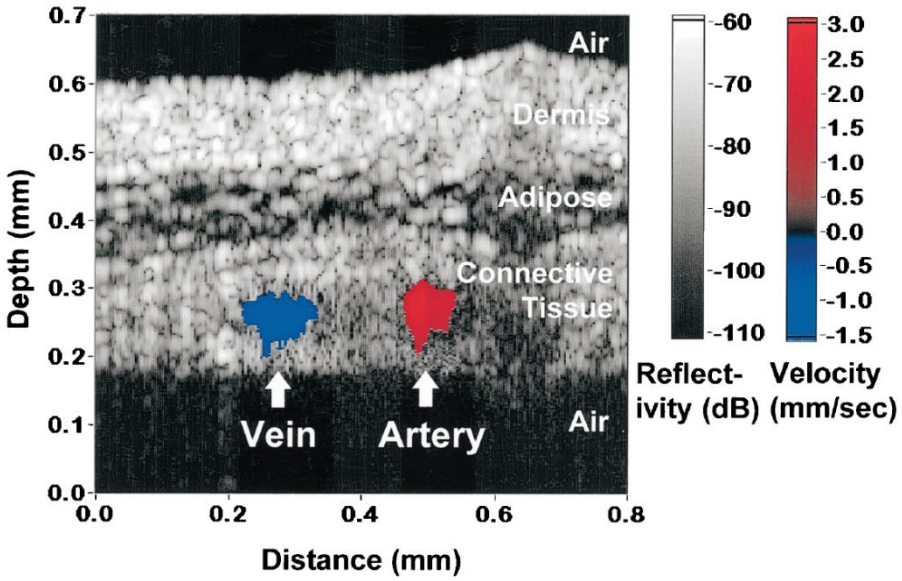

Figure 2.9: *In vivo* color DOCT image of a hamster dorsal skin-flap.

In the same year, based on the Doppler-shifted principle of DOCT, Izzat et al employed the short-time Fourier-transform (STFT) algorism to map out localized blood flow velocity in the cross-sectional OCT image of *in vivo* tissues with micrometer-scale resolution [30]. As shown in Fig. 2.9, the velocity of the blood flow was colored in the OCT image, thus their technology was reported as "color DOCT" [30]. Since then, many further improvements of DOCT have been achieved with the efforts of researchers and these technologies made the DOCT start to be applied for *in situ* and *in vivo* human tissue measurement. For example, the advanced DOCT developed by Zhao et al (Fig. 2.10-left) [31] and by Yazdanfar et al (Fig. 2.10-right) [46] respectively visualized the blood flow in the *in vivo* human skin and retina, and quantitatively measured velocity of the blood flow, successfully.

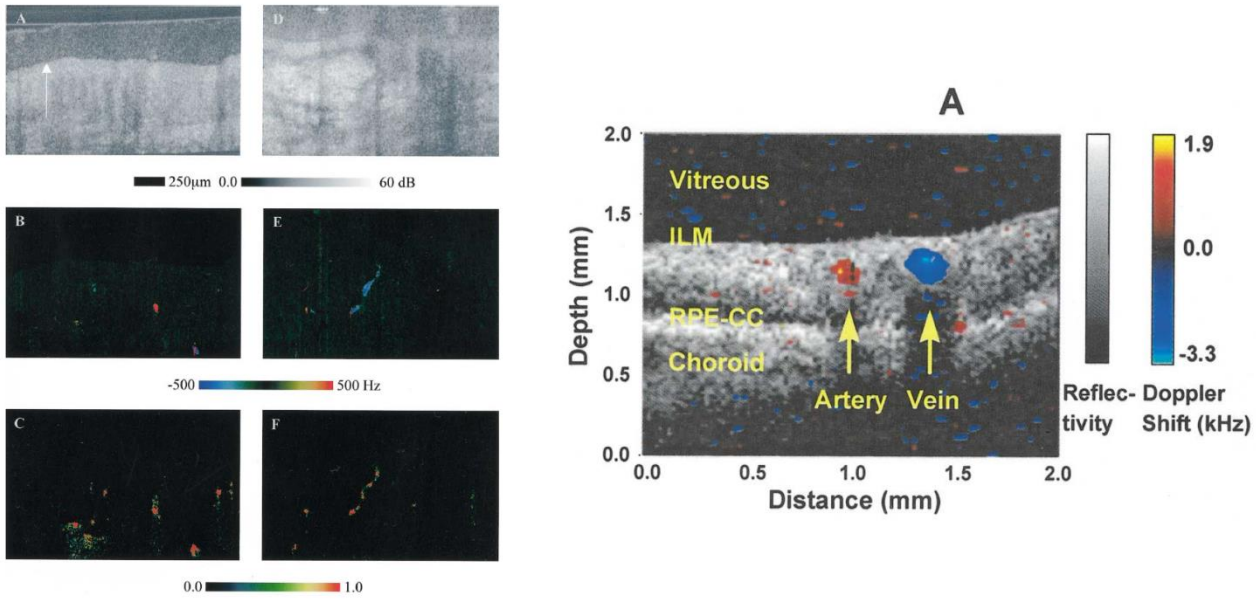

Figure 2.10: Left: OCT images (A, D) and blood flow velocity images (B, C, E, F) of *in vivo* human skin; Right: DOCT image with blood flow velocity data of *in vivo* human retina tissue.

2.2.3.3 OCT angiography

OCT angiography (OCTA/OCA) was developed based on DOCT theory and built on a high-speed SD-OCT, which has been developed by Makita et al in 2006 [32]. Same with DOCT, OCTA is applied for blood flow or vasculature imaging as well. Compared with most TD-OCT system based DOCT, the advantages of OCTA based on SD-OCT is the relatively high resolution, high speed and high contrast 3D imaging for vascular structures and blood flow [32,33]. OCTA, first, applies a histogram-based algorithm and phase wrapping method to eliminate the artifacts due to the bulk motion of the sample. And the phase difference between the adjacent axial scans (A-lines) is utilized to generate the bi-directional flow and power of Doppler shift images. By averaging these two images, the blood flow image is created. In addition, a correlation-based method is employed for motion compensation between two cross-sectional images (B-scans) in 3D imaging. Figure 2.11 [32] shows a group of OCA images of *in vivo* human optic nerve head (ONH). By applying the SD-OCT based

OCT-A and an improved segmentation algorithm, the three-dimensional vasculatures in the different tissue structures can be clearly observed and distinguished.

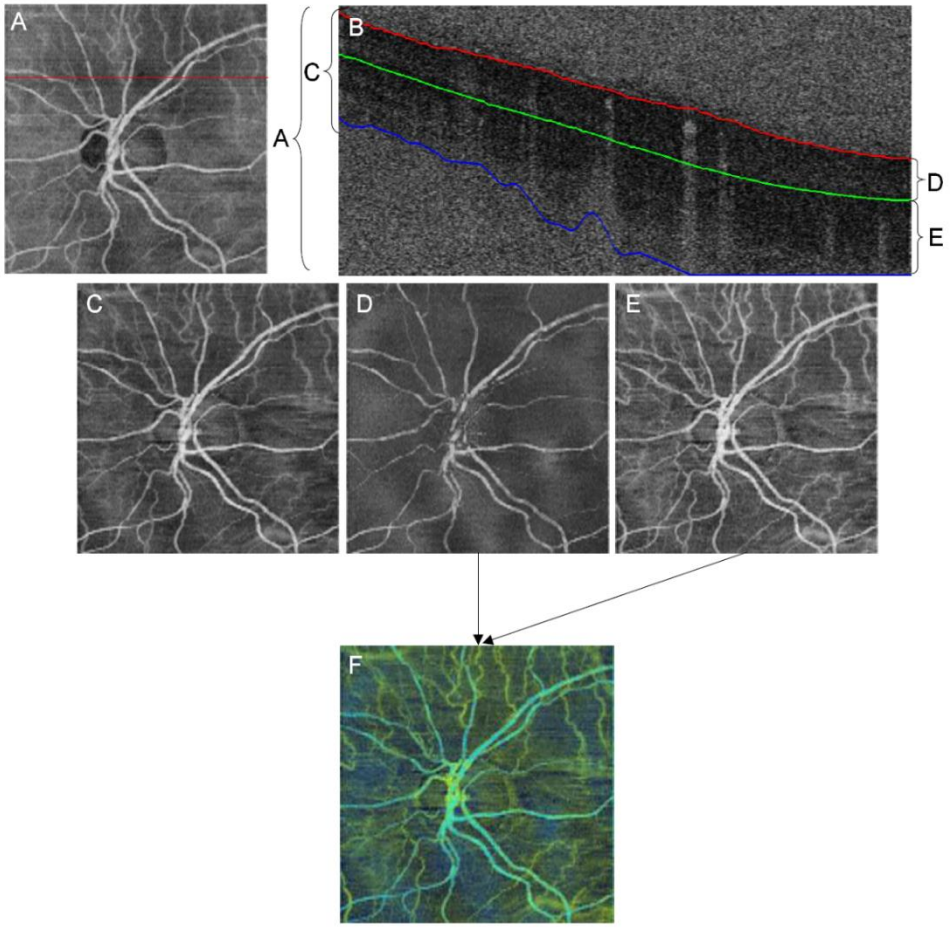

Figure 2.11: 3D OCTA of *in vivo* human ONH. A, projected OCTAs of the entire depth. B, cross-sectional blood flow image. C, projected OCTAs of the tissue region. D, retinal part. E, choroidal part. F, the combination of D and E [32].

2.2.3.4 Others

In addition to the above widely researched and used functional OCTs, there are sever other extensions to OCT, which possesses particular functions for biomedical investigations. Such as spectroscopic OCT, differential absorption OCT, refractometric OCT and so on. Furthermore, by combining the endoscope, elastography and other technologies, some new functional OCT technologies, such as endoscopic OCT, OCT elastography and so on, have been developed. They brought more challenges to the investigation of OCT and made it have more potential for biomedical and clinical applications.

2.3 Relevant parameters of OCT

2.3.1 Resolution

In contrast to optical confocal microscopy, the axial resolution is independent of lateral resolution in OCT imaging. It is mainly determined by the size of coherence length, which is related to the center wavelength and is inversely proportional to the spectral bandwidth of the used light source. For a Gaussian spectrum, the axial resolution, ΔZ, is typically expressed as equation (2) below:

$$\Delta Z = \frac{2\ln(2)}{\pi}\frac{{\lambda_0}^2}{\Delta\lambda} \quad (2),$$

where $\lambda_0$is the center wavelength and $\Delta\lambda$ is the bandwidth of the light source. Hence, a light source with relatively broad bandwidth and/or short center wavelength is able to improve the axial resolution. The above equation is only suitable for Gaussian spectrum. To further understand the impact of a spectrum of arbitrary shape probing beam on the axial resolution and artefacts, Fig. 2.12 plots the axial resolution versus bandwidth for light sources, exhibiting how axial resolution is affected by bandwidth of the light source for three different central wavelengths [47].

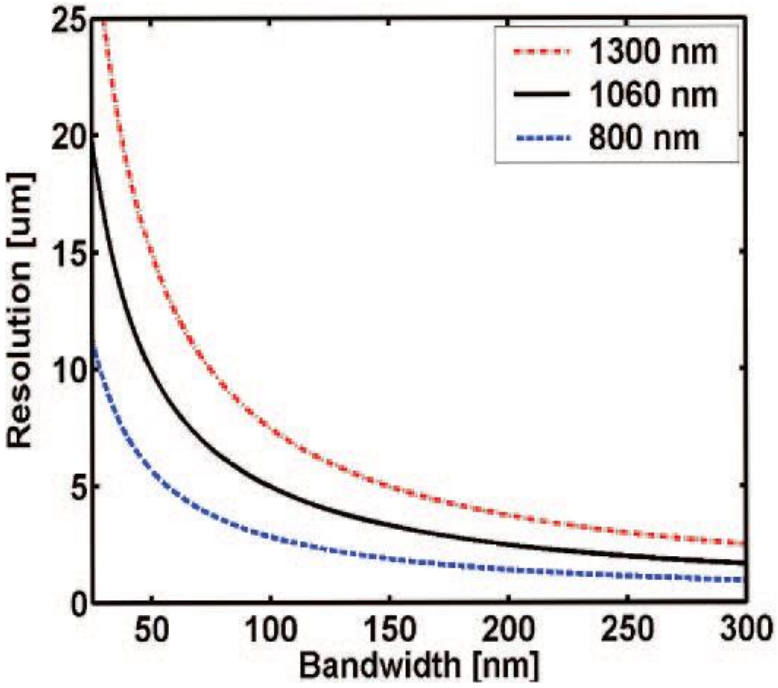

Figure 2.12: Axial resolution versus band width of light source for different center wavelengths [47].

On the other hand, the lateral resolution, Δx, in OCT is the same as in conventional microscopy and is fully dependent on the wavelength and the sample arm optics. Assuming a Gaussian beam, then the lateral resolution is given by

$$\Delta x = \frac{4\lambda_0}{\pi}\frac{f}{d} \quad (3),$$

where f is the focal length of the objective lens, and d is the diameter of the $1/e^2$ Gaussian beam at beam waist. It is inversely proportional to the numerical aperture (NA) of objective lens. In addition, the lateral resolution is also associated with the axial depth of field or the confocal parameter b, which is equal to twice the Rayleigh range z_R of the focused beam. It could be expressed by

$$b = 2z_R = \frac{\pi\Delta x^2}{\lambda_0} \quad (4).$$

Thus, a trade-off between a large axial depth of field and a high lateral resolution is presented and it has to be considered carefully. These parameters related to the resolution in OCT imaging are depicted in Fig. 2.13.

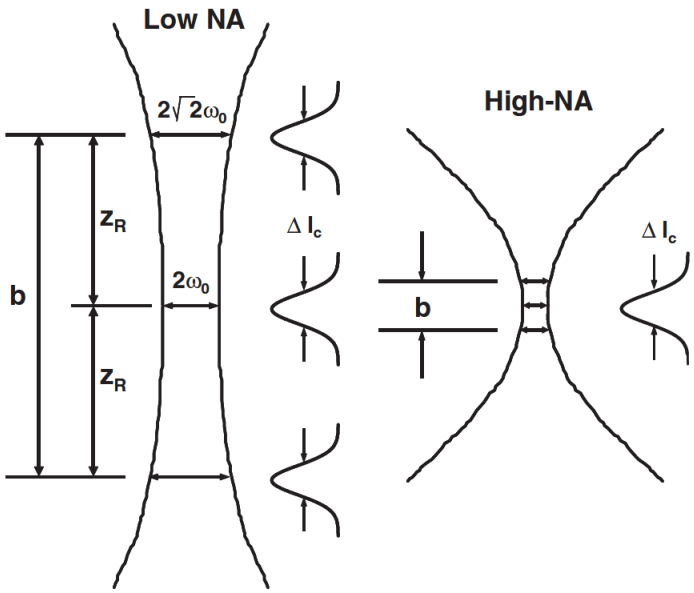

Figure 2.13: Lateral resolution in OCT [47].

In general, objective lens with a low numerical aperture focusing, i.e., large depth of field, is commonly utilized in OCT imaging. Also, it is possible to use a large NA in OCT for a sufficient lateral resolution. Furthermore, both fine lateral resolution and large depth of field can be achieved by means of Bessel-beam instead of Gaussian beam. Nevertheless, it results in increased complexity of the system setup and causes a sacrifice of signal-to-noise ratio (SNR) in OCT. In this study, the Gaussian beam is used for the development of OCT system.

2.3.2 Imaging depth range

Imaging depth range is another important parameter for OCT applications, especially in the biomedical field. The imaging depth of OCT is primarily limited by the penetration of the light source in the biological tissues. And it is also related to the center wavelength of the light and sampling number. Since frequency of the interference spectrum decodes the depth information. Therefore, the axial imaging depth z_{max} is defined by the maximum detectable interference fringe frequency. Then, the maximum imaging depth can be calculated as:

$$z_{max} = \frac{1}{4}\frac{{\lambda_0}^2}{\Delta\lambda}N \quad (5),$$

where $\Delta\lambda$ is the total recorded spectral width, and λ_0 is the center wavelength of source. For FD-OCT, and N is the number of the sampling points. Furthermore, the sensitivity is dependent on the depth in FD-OCT. Thus, the depth dependent signal decay affects the imaging depth range of FD-OCT as well. The Fourier transform of instantaneous linewidth gives the maximum imaging depth at -6-dB sensitivity as

$$z_{-6\mathrm{dB}} = \frac{\ln 2{\lambda_0}^2}{n\pi\Delta\lambda} \quad (6),$$

where n is the refractive index of sample, $\Delta\lambda$ is the spectrometer resolution in SD-OCT or the instantaneous linewidth in SS-OCT.

2.3.3 Sensitivity

The sensitivity of an imaging system is referred to the ratio of the maximum possible signal power to the noise power, namely, signal-to-noise ratio (SNR). Typically, there are three main noise sources including receiver noise, excess noise, shot noise in OCT, which limit the sensitivity of OCT imaging [14,48,49]. Receiver noise could be modeled as electrical and thermal noise within the detector. Excess noise and shot noise both arise from the detector photocurrent noise for the case of the broadband light source. In general, the reflectance of the tissue sample is much weaker than that of reference in an OCT system, and hence the optimum sensitivity can be achieved by adjusting the optical power. Figure 2.14 illustrates the sensitivity of OCT system as a function of the reference reflectance for different wavelength bandwidths [50]. It can be primarily classified into three regimes. At large source power, the excess noise would limit the sensitivity, and at small power, the sensitivity would be governed by receiver noise. Further, an optimized OCT system is typically operated in the shot-noise controlled regime with a moderate power. The well-known expression for the sensitivity of TD-OCT in the shot-noise limit regime is thus given by

$$\mathrm{SNR}_{TD-OCT} = \frac{\rho S_{TD-OCT} R_s}{2eB_{TD-OCT}} \quad (7),$$

where S_{TD-OCT} is the instantaneous source power incident in the sample and reference arms, R_s is the sample reflectance, e the electronic charge, and B_{TD-OCT} is the electronic detection bandwidth. Clearly, SNR of TD-OCT in the shot-limit regime is proportional to the optical power retuning from the sample ($S_{TD-OCT}R_s$), to the detector responsivity (ρ), and inversely proportional to the electronic bandwidth. Since the axial resolution can be enhanced by increasing bandwidth, a trade-off in sensitivity and axial resolution exists in TD-OCT. Similarly, considering the *SNR* of a FD-OCT system in the same operation regime, it is generally expressed by

$$\mathrm{SNR}_{TD-OCT} = \frac{\rho[S_{FD-OCT}(k_m)]R_s}{4eB_{FD-OCT}} M \quad (8),$$

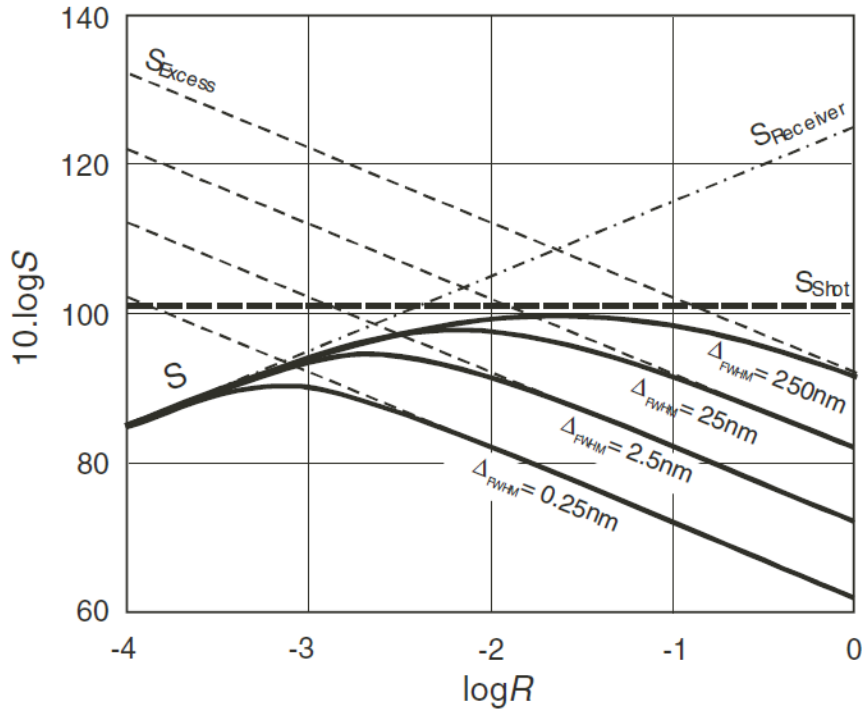

Figure 2.14: Sensitivity curves an OCT system as a function of the logarithm of reference mirror reflectivity *R* [50].

where *M* is the number of spectral bins in detector array or number of spectral lines in the source, $S_{FD-OCT}(k_m)$ is that portion of the instantaneous power incident on the sample, corresponding to spectral channel *m* of the detection array, whether time-multiplexed in SSOCT or on separate detectors in SDOCT. Further to compare TD-OCT and FD-OCT, SNR is further written as:

$$\mathrm{SNR}_{FD-OCT} \approx \mathrm{SNR}_{TD-OCT}\frac{M}{2} \quad (9).$$

According to the equation above, it can be known that the improvement in SNR of FD-OCT by a factor of M/2 as comparing to TD-OCT system, where M >>2 for a realistic detector array or swept-source laser.

2.4 Applications of OCT

OCT was originally developed for imaging of ophthalmology, and currently is still mainly applied in the ophthalmology field. The reason is that the eye has very special structure, which is a translucent and near-optical system. It makes the eye fit quite well for OCT measurement. The first application of OCT in ophthalmology is in 1993, which was demonstrated by Swanson et al [51]. It indicated the potential ability of OCT for the clinical diagnosis in ophthalmology. Since then, quite a lot of researches has demonstrated the usefulness of OCT for the investigations of biomedical and clinical medicines in ophthalmology. Figure 2.15 shows an example of the application of OCT in ophthalmology [12]. The results show the potential of relative early diagnosis of eye disease by OCT imaging.

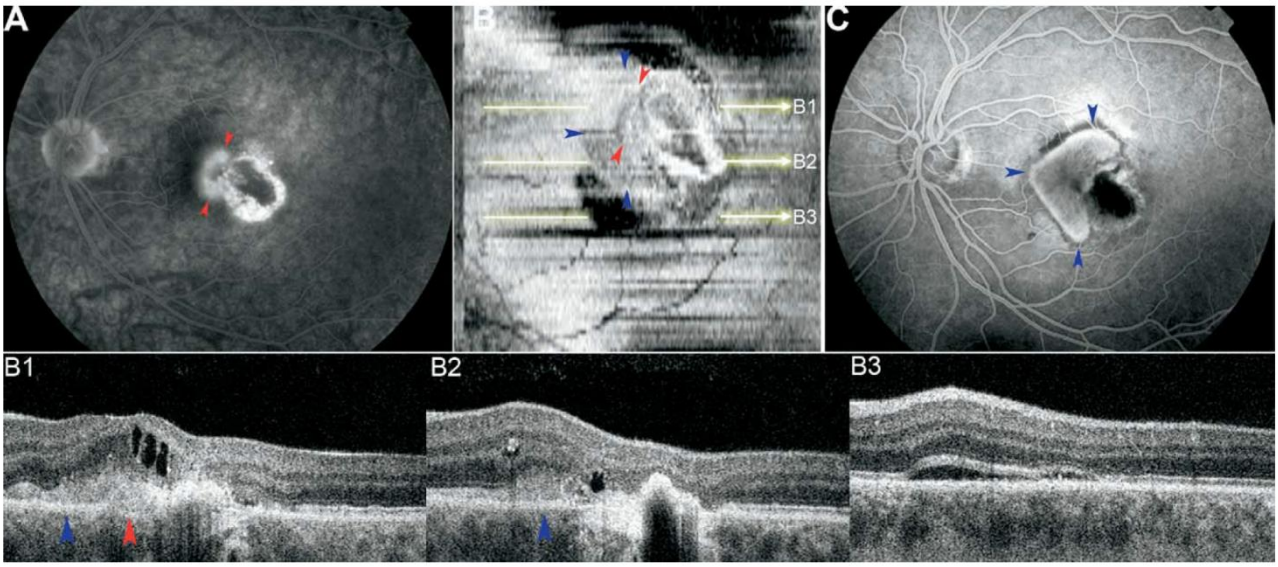

Figure 2.15: OCT images of choroidal neovascular membrane (CNV) in age-related macular degeneration. A, *en-face* fluorescein angiography image of CNV. B, *en-face* OCT image (C-scan) of CNV (B1, B2, B3 are the cross-sectional images (B-scans) of the subretinal tissues, B1, B2 shows the extended lesions in subretinal tissue. C, fluorescein angiography images of the CNV progress after 3 months [12].

Since the advantages, such as high resolution, high speed, and high sensitivity, have made OCT become a good tool in ophthalmology. However, its disadvantage that short penetration distance in other tissues limits the application of OCT in other medical fields. Although there are also many efforts have been worked in several other medical fields, such as cardiology, gastroenterology, dentistry, dermatology and so on. These

studies still almost stay in the stage of laboratorial demonstration and might be far away from the practical clinical applications. Along with the improvement of the OCTs' performance and the developments of some functional extensions to OCT, OCT has started to break the limitation of OCT in other biomedical fields. In 2000, for example, the endoscopic technology combined OCT demonstrated a potential real-time biopsy for intestinal disease diagnosis [52]. A tubular adenoma of the colon tissue was successfully characterized by an endoscopic OCT imaging (Fig. 2.16) [52].

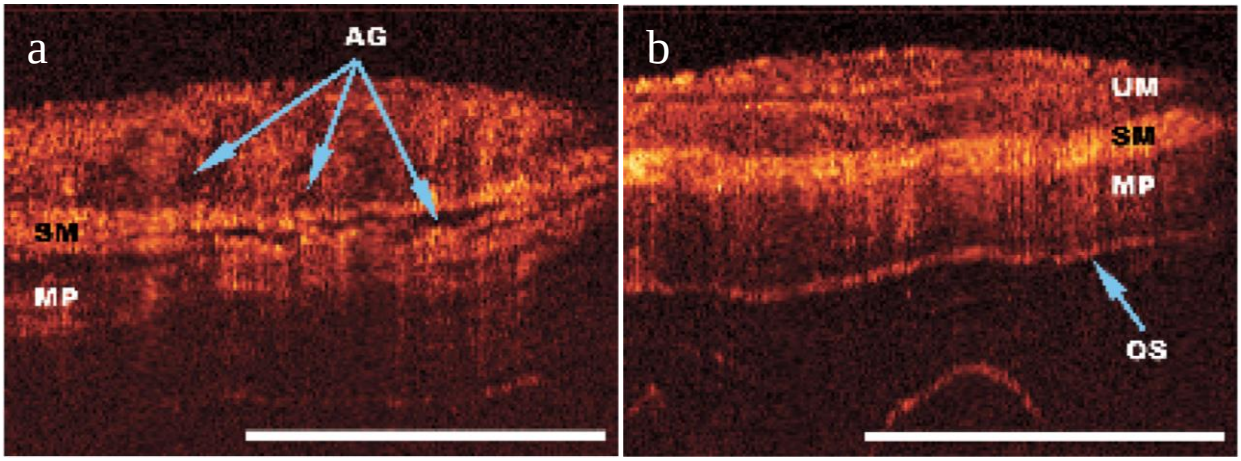

Figure 2.16: *In vivo* OCT imaging for gastroenterology. A, a transverse colon tissue with tubular adenoma. B, a normal transverse colon tissue [52].

Another promising medical application of OCT is dermatology. Skin is easily accessible sample by OCT. Although in current clinical dermatology, the main diagnosis method for skin disease is using naked eye based on the doctor's experiences. However, it is not accurate. Moreover, for the diagnosis of skin cancers, the biopsy and pathological examination are invasive and usually take a long time. Thus, the OCT would be expected to be a new method of dermatological diagnosis, which is non-invasive, rapid and accurate. Figure 2.17 shows

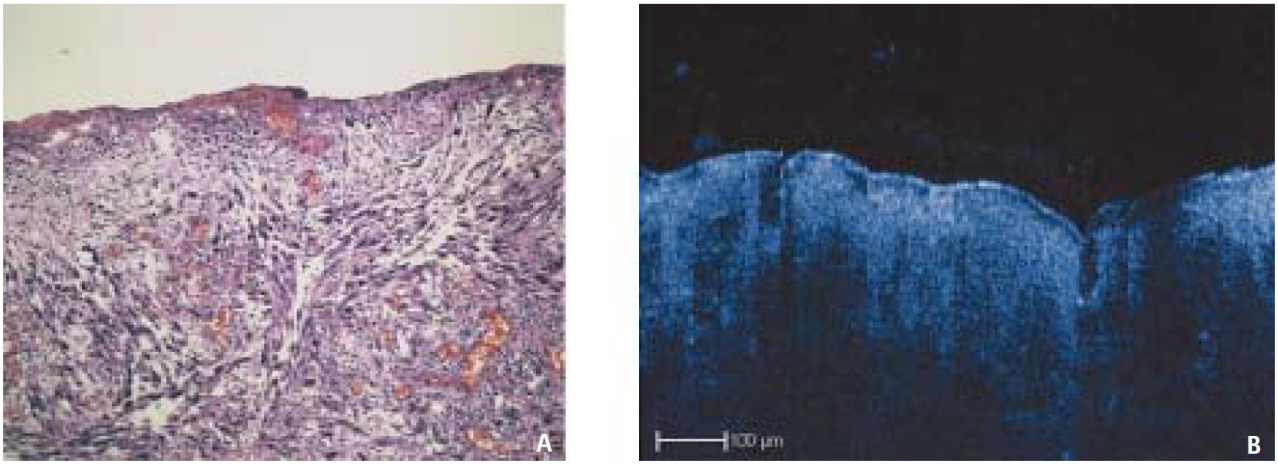

Figure 2.17: OCT imaging for dermatology. A) histological image and B) cross-sectional OCT image of a skin tissue with malignant melanoma [53].

an example of malignant melanoma in skin tissue measured by OCT [53]. Because of the limited penetration, how much depth of the skin was invaded by the cancer was impossible to be measured. However, it still shows a potential ability of OCT to detect the cancer of skin tissue in real-time.

2.5 Summary

In this chapter, the development of OCT technology is systematically introduced, where two major types of OCT, i.e. TD-OCT as first-generation OCT and FD-OCT as second-generation OCT, together with a few emerging extended OCT techniques are explained with their own advantages and disadvantages. Overall, FD-OCT has gradually replaced TD-OCT in recent years because it enables improved imaging speed and enhanced SNR and sensitivity. Moreover, a series of key parameters, such as resolution, imaging depth range, sensitivity, etc., closely related to the performance of an OCT system and the imaging quality are also described in this chapter. Further to consider the practical application, OCT technology is now mainly applied in ophthalmology field. But with continuous technology innovation, OCT becomes one of most promising approach in the imaging of dermatological tissues and it even present the potential ability to detect the cancer of skin tissue in real-time.

References

1. D. Huang, E. A. Swanson, C. P. Lin, J. S. Schuman, W. G. Stinson, W. Chang, M. R. Hee, T. Flotte, K. Gregory, C. A. Puliafito, and J. G. Fujimoto, "Optical Coherence Tomography," Science **254**(5035), 1178–1181 (1991).

2. J. M. Schmitt, "Optical coherence tomography (OCT): a review," IEEE J. Sel. Top. Quantum Electron. **5**(4), 1205–1215 (1999).

3. J. M. Schmitt, A. Knuttel, M. Yadlowsky, and M. A. Eckhaus, "Optical-coherence tomography of a dense tissue: statistics of attenuation and backscattering," Phys. Med. Biol. **39**(10), 1705–1720 (1994).

4. A. F. Fercher, "Optical coherence tomography," J. Biomed. Opt. **1**(2), 157–173 (1996).

5. S. H. Yun, G. J. Tearney, J. F. de Boer, N. Iftimia, and B. E. Bouma, "High-speed optical frequency-domain imaging," Opt. Express **11**(22), 2953–2963 (2003).

6. A. F. Fercher, C. K. Hitzenberger, G. Kamp, and S. Y. El-Zaiat, "Measurement of intraocular distances by backscattering spectral interferometry," Opt. Commun. **117**(1), 43–48 (1995).

7. G. Haeusler and M. W. Lindner, ""“Coherence radar” and “Spectral radar”- new tools for dermatological diagnosis," J. Biomed. Opt. **3**(1), 21–31 (1998).

8. N. A. Nassif, B. Cense, B. H. Park, M. C. Pierce, S. H. Yun, B. E. Bouma, G. J. Tearney, T. C. Chen, and J. F. de Boer, "In vivo high-resolution video-rate spectral-domain optical coherence tomography of the human retina and optic nerve," Opt. Express **12**(3), 367–376 (2004).

9. M. Wojtkowski, V. J. Srinivasan, T. H. Ko, J. G. Fujimoto, A. Kowalczyk, and J. S. Duker, "Ultrahigh-resolution, high-speed, Fourier domain optical coherence tomography and methods for dispersion compensation," Opt. Express **12**(11), 2404–2422 (2004).

10. Y. Yasuno, V. D. Madjarova, S. Makita, M. Akiba, A. Morosawa, C. Chong, T. Sakai, K.-P. Chan, M. Itoh, and T. Yatagai, "Three-dimensional and high-speed swept-source optical coherence tomography for in vivo investigation of human anterior eye segments," Opt. Express **13**(26), 10652–10664 (2005).

11. M. Yamanari, S. Makita, Y. Lim, and Y. Yasuno, "Full-range polarization-sensitive swept-source optical coherence tomography by simultaneous transversal and spectral modulation," Opt. Express **18**(13), 13964–13980 (2010).

12. S. Alam, R. J. Zawadzki, S. Choi, C. Gerth, S. S. Park, L. Morse, and J. S. Werner, "Clinical Application of Rapid Serial Fourier-Domain Optical Coherence Tomography for Macular Imaging," Ophthalmology **113**(8), 1425–1431 (2006).

13. S. Takarada, T. Imanishi, Y. Liu, H. Ikejima, H. Tsujioka, A. Kuroi, K. Ishibashi, K. Komukai, T. Tanimoto, Y. Ino, H. Kitabata, T. Kubo, N. Nakamura, K. Hirata, A. Tanaka, M. Mizukoshi, and T. Akasaka, "Advantage of next-generation frequency-domain optical coherence tomography compared with conventional time-domain system in the assessment of coronary lesion," Catheter. Cardiovasc. Interv. **75**(2), 202–206 (2010).

14. R. Leitgeb, C. K. Hitzenberger, and A. F. Fercher, "Performance of fourier domain vs. time domain optical coherence tomography," Opt. Express **11**(8), 889–894 (2003).

15. J. F. de Boer, B. Cense, B. H. Park, M. C. Pierce, G. J. Tearney, and B. E. Bouma, "Improved signal-to-noise ratio in spectral-domain compared with time-domain optical coherence tomography," Opt. Lett. **28**(21), 2067–2069 (2003).

16. J. F. de Boer, R. Leitgeb, and M. Wojtkowski, "Twenty-five years of optical coherence tomography: the paradigm shift in sensitivity and speed provided by Fourier domain OCT [Invited]," Biomed. Opt. Express **8**(7), 3248–3280 (2017).

17. N. Nassif, B. Cense, B. H. Park, S. H. Yun, T. C. Chen, B. E. Bouma, G. J. Tearney, and J. F. de Boer, "In vivo human retinal imaging by ultrahigh-speed spectral domain optical coherence tomography," Opt. Lett. **29**(5), 480–482 (2004).

18. D. P. Popescu, L.-P. Choo-Smith, C. Flueraru, Y. Mao, S. Chang, J. Disano, S. Sherif, and M. G. Sowa, "Optical coherence tomography: fundamental principles, instrumental designs and biomedical applications," Biophys. Rev. **3**(3), (2011).

19. H. M. Subhash and R. K. Wang, "Optical Coherence Tomography: Technical Aspects," in *Biomedical Optical Imaging Technologies: Design and Applications*, R. Liang, ed., Biological and Medical Physics, Biomedical Engineering (Springer, 2013), pp. 163–212.

20. M. Wojtkowski, R. Leitgeb, A. Kowalczyk, T. Bajraszewski, and A. F. Fercher, "In vivo human retinal imaging by Fourier domain optical coherence tomography," J. Biomed. Opt. **7**(3), 457–463 (2002).

21. M. Wojtkowski, A. Kowalczyk, R. Leitgeb, and A. F. Fercher, "Full range complex spectral optical coherence tomography technique in eye imaging," Opt. Lett. **27**(16), 1415–1417 (2002).

22. S. Wolf and U. Wolf-Schnurrbusch, "Spectral-Domain Optical Coherence Tomography Use in Macular Diseases: A Review," Ophthalmologica **224**(6), 333–340 (2010).

23. J. F. Bille, ed., *High Resolution Imaging in Microscopy and Ophthalmology: New Frontiers in Biomedical Optics* (Springer International Publishing, 2019).

24. A. G. Podoleanu, "Optical coherence tomography," J. Microsc. **247**(3), 209 (2012).

25. L. An, P. Li, T. T. Shen, and R. Wang, "High speed spectral domain optical coherence tomography for retinal imaging at 500,000 A-lines per second," Biomed. Opt. Express **2**(10), 2770–2783 (2011).

26. J. S. Schuman, "Spectral Domain Optical Coherence Tomography for Glaucoma (An AOS Thesis)," Trans. Am. Ophthalmol. Soc. **106**, 426 (2008).

27. L. Zhang, G. H. S. Buitendijk, K. Lee, M. Sonka, H. Springelkamp, A. Hofman, J. R. Vingerling, R. F. Mullins, C. C. W. Klaver, and M. D. Abràmoff, "Validity of Automated Choroidal Segmentation in SS-OCT and SD-OCT," Invest. Ophthalmol. Vis. Sci. **56**(5), 3202–3211 (2015).

28. R. K. Wang, S. Kirkpatrick, and M. Hinds, "Phase-sensitive optical coherence elastography for mapping tissue microstrains in real time," Appl. Phys. Lett. **90**(16), 164105 (2007).

29. J. F. de Boer, T. E. Milner, M. J. C. van Gemert, and J. S. Nelson, "Two-dimensional birefringence imaging in biological tissue by polarization-sensitive optical coherence tomography," Opt. Lett. **22**(12), 934–936 (1997).

30. J. A. Izatt, M. D. Kulkarni, S. Yazdanfar, J. K. Barton, and A. J. Welch, "In vivo bidirectional color Doppler flow imaging of picoliter blood volumes using optical coherence tomography," Opt. Lett. **22**(18), 1439–1441 (1997).

31. Y. Zhao, Z. Chen, C. Saxer, Q. Shen, S. Xiang, J. F. de Boer, and J. S. Nelson, "Doppler standard deviation imaging for clinical monitoring of in vivo human skin blood flow," Opt. Lett. **25**(18), 1358–1360 (2000).

32. S. Makita, Y. Hong, M. Yamanari, T. Yatagai, and Y. Yasuno, "Optical coherence angiography," Opt. Express **14**(17), 7821–7840 (2006).

33. S. Makita, K. Kurokawa, Y.-J. Hong, M. Miura, and Y. Yasuno, "Noise-immune complex correlation for optical coherence angiography based on standard and Jones matrix optical coherence tomography," Biomed. Opt. Express **7**(4), 1525–1548 (2016).

34. M. R. Hee, D. Huang, E. A. Swanson, and J. G. Fujimoto, "Polarization-sensitive low-coherence reflectometer for birefringence characterization and ranging," JOSA B **9**(6), 903–908 (1992).

35. J. F. de Boer, S. M. Srinivas, A. Malekafzali, Z. Chen, and J. S. Nelson, "Imaging thermally damaged tissue by polarization sensitive optical coherence tomography," Opt. Express **3**(6), 212–218 (1998).

36. J. F. de Boer, T. E. Milner, M. J. C. van Gemert, and J. S. Nelson, "Two-dimensional birefringence imaging in biological tissue by polarization-sensitive optical coherence tomography," Opt. Lett. **22**(12), 934–936 (1997).

37. E. Götzinger, M. Pircher, B. Baumann, C. Ahlers, W. Geitzenauer, U. Schmidt-Erfurth, and C. K. Hitzenberger, "Three-dimensional polarization sensitive OCT imaging and interactive display of the human retina," Opt. Express **17**(5), 4151–4165 (2009).

38. Y. Yasuno, S. Makita, Y. Sutoh, M. Itoh, and T. Yatagai, "Birefringence imaging of human skin by polarization-sensitive spectral interferometric optical coherence tomography," Opt. Lett. **27**(20), 1803–1805 (2002).

39. B. H. Park, M. C. Pierce, B. Cense, and J. F. de Boer, "Jones matrix analysis for a polarization-sensitive optical coherence tomography system using fiber-optic components," Opt. Lett. **29**(21), 2512–2514 (2004).

40. B. Baumann, "Polarization Sensitive Optical Coherence Tomography: A Review of Technology and Applications," Appl. Sci. **7**(5), 474 (2017).

41. J. F. de Boer, C. K. Hitzenberger, and Y. Yasuno, "Polarization sensitive optical coherence tomography - a review [Invited]," Biomed. Opt. Express **8**(3), 1838–1873 (2017).

42. M. Yamanari, S. Tsuda, T. Kokubun, Y. Shiga, K. Omodaka, Y. Yokoyama, N. Himori, M. Ryu, S. Kunimatsu-Sanuki, H. Takahashi, K. Maruyama, H. Kunikata, and T. Nakazawa, "Fiber-based polarization-sensitive OCT for birefringence imaging of the anterior eye segment," Biomed. Opt. Express **6**(2), 369–389 (2015).

43. X. J. Wang, T. E. Milner, and J. S. Nelson, "Characterization of fluid flow velocity by optical Doppler tomography," Opt. Lett. **20**(11), 1337–1339 (1995).

44. Z. Chen, T. E. Milner, S. Srinivas, X. Wang, A. Malekafzali, M. J. C. van Gemert, and J. S. Nelson, "Noninvasive imaging of in vivo blood flow velocity using optical Doppler tomography," Opt. Lett. **22**(14), 1119–1121 (1997).

45. Z. Chen, T. E. Milner, S. Srinivas, X. Wang, A. Malekafzali, M. J. C. van Gemert, and J. S. Nelson, "Noninvasive imaging of in vivo blood flow velocity using optical Doppler tomography," Opt. Lett. **22**(14), 1119–1121 (1997).

46. S. Yazdanfar, A. M. Rollins, and J. A. Izatt, "Imaging and velocimetry of the human retinal circulation with color Doppler optical coherence tomography," Opt. Lett. **25**(19), 1448–1450 (2000).

47. W. Drexler and J. G. Fujimoto, *Optical Coherence Tomography: Technology and Applications* (Springer Science & Business Media, 2008).

48. V. V. Tuchin, ed., *Handbook of Coherent-Domain Optical Methods: Biomedical Diagnostics, Environmental Monitoring, and Materials Science*, 2nd ed. (Springer-Verlag, 2013).

49. *Lasers and Current Optical Techniques in Biology* (2004).

50. A. F. Fercher, W. Drexler, C. K. Hitzenberger, and T. Lasser, "Optical coherence tomography - principles and applications," Rep. Prog. Phys. **66**(2), 239–303 (2003).

51. E. A. Swanson, J. A. Izatt, M. R. Hee, D. Huang, C. P. Lin, J. S. Schuman, C. A. Puliafito, and J. G. Fujimoto, "In vivo retinal imaging by optical coherence tomography," Opt. Lett. **18**(21), 1864–1866 (1993).

52. S. Jäckle, N. Gladkova, F. Feldchtein, A. Terentieva, B. Brand, G. Gelikonov, V. Gelikonov, A. Sergeev, A. Fritscher-Ravens, J. Freund, U. Seitz, S. Schröder, and N. Soehendra, "In Vivo Endoscopic Optical Coherence Tomography of the Human Gastrointestinal Tract - Toward Optical Biopsy," Endoscopy **32**(10), 743–749 (2000).

53. R. Steiner, K. Kunzi-Rapp, and K. Scharffetter-Kochanek, "Optical Coherence Tomography: Clinical Applications in Dermatology," Med. Laser Appl. **18**(3), 249–259 (2003).

Chapter 3

Theory of multifunctional Jones-matrix optical coherence tomography (JM-OCT)

3.1 Introduction

In Chapter 1, several functional OCTs have been introduced. And each functional OCT is capable of providing a specific contrast of the different detailed structures or properties for biological tissue. Sometimes, a single image is not possible to represent enough characteristics of the tissue, it may lead to some important information lost. Thus, the multifunctional OCT (MF-OCT) has been developed to simultaneously acquiring few kinds of contrasts of the tissue, such as scattering intensity (OCT), Doppler (or OCTA), degree of polarization uniformity (DOPU) and phase retardation (or birefringence) images [1–4]. Because all of these MF-OCTs were built based on a Jones-matrix-based PS-OCT (JM-OCT). Thus, the principle of JM-OCT, first, will be illustrated in this chapter. And it is also the theoretical basis of the research presented in this thesis.

3.2 Principle of JM-OCT

JM-OCT is essentially one form of PS-OCT that has been mentioned in section 2.2.3 of Chapter 2. Hence, the primary purpose of JM-OCT is to measure the polarization properties of biological tissue, such as phase-retardation, diattenuation, and optic-axis orientation. And these polarizations of tissue associate with the birefringence of the microstructures or some chemical compositions in tissue.

3.2.1 General principle

JM-OCT was established based on the Joes matrix theory that demonstrates to describe the polarization affected by the optical systems (including the optical elements or birefringent materials) [5]. With the Jones matrix theory, first, the complete polarized light entered in an optical system can be decomposed into two orthogonal polarization states and be represented as a pair of Jones vectors:

$$\boldsymbol{E}_{in} = \begin{bmatrix} E_x \\ E_y \end{bmatrix} \quad (1),$$

where the superscripts *x* and *y* express the two orthogonal polarized components of the incident light. Because the states (amplitude and phase) of the two polarization components will change after going through an optical system which can be characterized by a complex 2 × 2 Jones matrix. Then, the relationship between the two polarized beams and an optical system is described as follow,

$$\boldsymbol{E}_{out} = \begin{bmatrix} J_{11} & J_{12} \\ J_{21} & J_{22} \end{bmatrix} \begin{bmatrix} E_x \\ E_y \end{bmatrix} = \boldsymbol{J}\boldsymbol{E}_{in} \quad (2).$$

Here, all of the vectors in the matrixes are considered in a three-dimensional spatial (x, y, z). Just for simplification, the coordinates are temporally omitted. Thus, from the Eq. (2), the Jones matrix of the optical system can be expressed by the electric field vectors of the input and output polarized beams as:

$$\boldsymbol{J} = \boldsymbol{E}_{out}\boldsymbol{E}_{in}^{-1} \quad (3).$$

Considered to apply this relationship in an OCT measurement system, as shown in Fig. 3.1. An incident 45˚ linear polarized light is first aligned by a series of the optical elements and some single-mode-fibers (SMF). And then, it can be optimized and separated into two orthogonal polarization states by the optical elements, and these two beams with different polarization states enable to be multiplexed by the special configuration of the JM-OCT system as well. However, because the birefringence of the optical components, especially the SMFs, are very sensitive to the environment and fiber conditions (such as mechanical stress and temperature et al), it is almost impossible to determine the actual incident polarization states to the sample. And it is also quite difficult to measure the exact Jones vectors of the back-scattered beam from the sample. Thus, to resolve this problem, referring to the above expression, several symbols are determined. First, the input and output polarization states, respectively corresponding to which come from JM-OCT system and generated by the interferometer in it, are represented as $\boldsymbol{J}_{in}$ and $\boldsymbol{J}_{out}$. Similarly, the Jones matrices of the round-trip in the sample are represented as $\boldsymbol{J}_s$ and $\boldsymbol{J}_s^T$. These parameters of the optical systems and measured biological tissue are also spatially resolved, thus they are the functions of positional coordinates (x, y, z) as well, and the z-axis is the direction of the depth in the sample. Then, the single-trip Jones matrix of a part of the tissue with a certain thickness in the sample can be further described as $\boldsymbol{J}_s(z)$. Here, the (x, y) are omitted for simplification as well. Thereby, the expression of the incident light effected by the OCT system and sample is modified as follow:

$$\boldsymbol{J}(z) = \boldsymbol{J}_{out}\boldsymbol{J}_s^T(z)\boldsymbol{J}_s(z)\boldsymbol{J}_{in} = \boldsymbol{E}_{out}(z)\boldsymbol{E}_{in}^{-1} \quad (4),$$

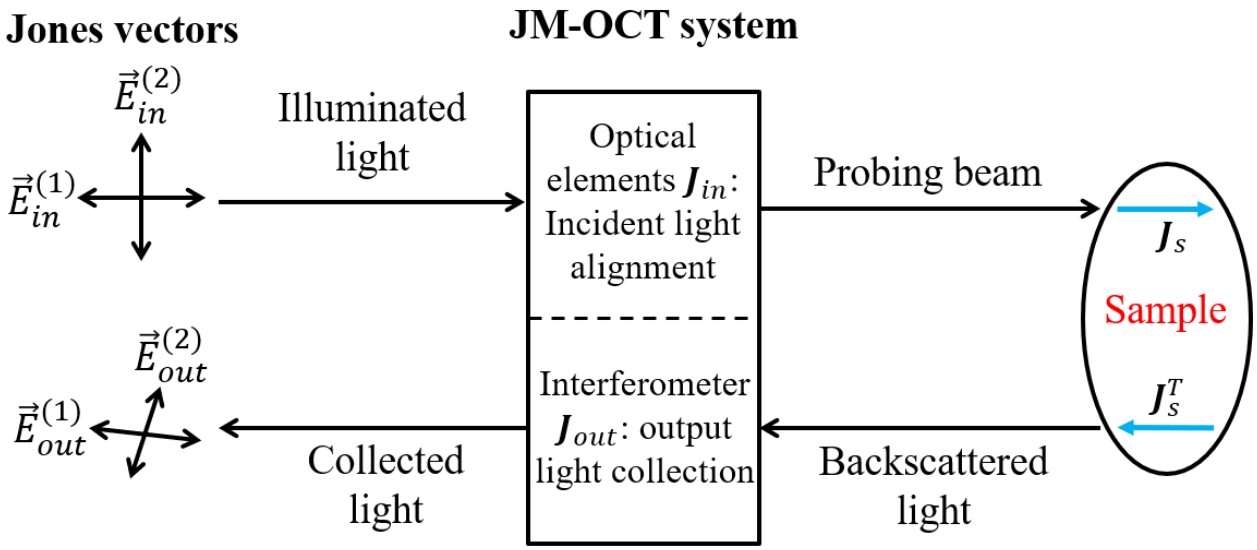

Figure 3.1: The schematic diagram of the JM-OCT measurement.

where the $\boldsymbol{J}(z)$ represents the whole Jones matrix in the process of JM-OCT measurement that contains the OCT system and the measured part of the tissue. $\boldsymbol{E}_{out}$ and $\boldsymbol{E}_{in}^{-1}$ are the matrix and the inverse matrix of the output and input lights consisting of the two polarized beams with different states, and $\boldsymbol{E}_{in} = \left[\vec{E}_{in}^{(1)}, \vec{E}_{in}^{(2)}\right]$, $\vec{E}_{in}^{(1)}$ and $\vec{E}_{in}^{(2)}$ are two orthogonal polarized beams.

If the back-scattered lights are reflected by the surface of the tissue, i.e. when $z = z_0 = 0$, the corresponding Jones matrix of the sample is denoted as $\boldsymbol{J}_s(z_0)$, and the whole Jones matrix is $\boldsymbol{J}(z_0)$. The Jones matrix of the output light is $\boldsymbol{E}_{out}(z_0)$. Similarly, Eq. (4) can be expressed as:

$$\boldsymbol{J}(z_0) = \boldsymbol{J}_{out}\boldsymbol{J}_s^T(z_0)\boldsymbol{J}_s(z_0)\boldsymbol{J}_{in} = \boldsymbol{E}_{out}(z_0)\boldsymbol{E}_{in}^{-1} \quad (5).$$

To figure out the Jones matrix of the measured tissue or its similar matrix, the inverse matrix of $\boldsymbol{J}(z_0)$, which is the transformation of Eq. (5)

$$\boldsymbol{J}(z_0)^{-1} = \boldsymbol{J}_{in}{}^{-1}\boldsymbol{J}_s(z_0)^{-1}\boldsymbol{J}_s^T(z_0)^{-1}\boldsymbol{J}_{out}{}^{-1} = \boldsymbol{E}_{in}\boldsymbol{E}_{out}(z_0)^{-1} \quad (6),$$

is considered to be employed in the Eq. (4). Then the following equation is obtained:

$$\begin{aligned}\boldsymbol{J}(z)\boldsymbol{J}(z_0)^{-1} &= \boldsymbol{J}_{out}\boldsymbol{J}_s^T(z)\boldsymbol{J}_s(z)\boldsymbol{J}_{in}\boldsymbol{J}_{in}{}^{-1}\boldsymbol{J}_s(z_0)^{-1}\boldsymbol{J}_s^T(z_0)^{-1}\boldsymbol{J}_{out}{}^{-1} \\ &= \boldsymbol{E}_{out}(z)\boldsymbol{E}_{in}^{-1}\boldsymbol{E}_{in}\boldsymbol{E}_{out}(z_0)^{-1} \quad (7).\end{aligned}$$

It can be further simplified as:

$$\begin{aligned}\boldsymbol{J}(z)\boldsymbol{J}(z_0)^{-1} &= \boldsymbol{J}_{out}\boldsymbol{J}_s^T(z)\boldsymbol{J}_s(z)\boldsymbol{J}_s(z_0)^{-1}\boldsymbol{J}_s^T(z_0)^{-1}\boldsymbol{J}_{out}{}^{-1} \\ &= \boldsymbol{E}_{out}(z)\boldsymbol{E}_{out}(z_0)^{-1} \quad (8).\end{aligned}$$

In general, the diattenuation of the sample surface is considered to be negligible, thus the round-trip Jones matrix of the sample's surface can be treated as an identity matrix. [6,7] Consequently, Eq. (8) is finally simplified as:

$$\boldsymbol{J}(z)\boldsymbol{J}(z_0)^{-1} = \boldsymbol{J}_{out}\boldsymbol{J}_s^T(z)\boldsymbol{J}_s(z)\boldsymbol{J}_{out}{}^{-1} = \boldsymbol{E}_{out}(z)\boldsymbol{E}_{out}(z_0)^{-1} \quad (9).$$

This equation indicates that the matrix (or inverse matrix) of the electric field intensities of the output lights is the similar matrix of the round-trip Jones matrix of the sample. The matrix $\boldsymbol{E}_{out}(z)$ and the inverse matrix $\boldsymbol{E}_{out}(z_0)^{-1}$ respectively corresponds to the output lights from the depth of *z* and sample's surface. It should be noticed that, the $\boldsymbol{E}_{out}(z)$ and $\boldsymbol{E}_{out}(z_0)$ in Eq. (7) – (9) are two independent matrices, namely the matrix $\boldsymbol{E}_{out}(z_0)$ (or the matrix of incident lights $\boldsymbol{E}_{in}$) should be a non-singular matrix for obtaining the inverse matrix $\boldsymbol{E}_{out}(z_0)^{-1}$ (or $\boldsymbol{E}_{in}^{-1}$).

Since the matrix $[\boldsymbol{E}_{out}(z)\boldsymbol{E}_{out}(z_0)^{-1}]$ is the similar matrix of the round-trip Jones matrix $[\boldsymbol{J}_s^T(z)\boldsymbol{J}_s(z)]$ of the measured tissue, therefore, $[\boldsymbol{J}_s^T(z)\boldsymbol{J}_s(z)]$ and $[\boldsymbol{E}_{out}(z)\boldsymbol{E}_{out}(z_0)^{-1}]$ has the same eigenvalues.

Nevertheless, their eigenvectors are not the same, generally. Furthermore, the amount of $[\boldsymbol{E}_{out}(z)\boldsymbol{E}_{out}(z_0)^{-1}]$ is possible to be measured by OCT. As a result, the eigenvalues $\lambda_{1,2}$ (corresponding to the two orthogonal incident polarized beams) and eigenvectors of $[\boldsymbol{J}_s^T(z)\boldsymbol{J}_s(z)]$ can be calculated by utilizing the measured similar matrix and a numerical eigenvalue algorism, i. e., off-diagonal elements minimality and matrix-diagonalization methods [6,8]. It is known that the eigenvalues are also can be acquired by using the following equation:

$$\lambda_{1,2} = \frac{T}{2} \pm \sqrt{\frac{T^2}{4} - D} \quad (10),$$

where the T and D respectively represent the trace and determinant of the round-trip Jones matrix of the sample. Then, with the obtained eigenvalues, the polarization properties of the tissue can be measured.

3.2.2 Polarization properties of biological tissue

As mentioned in Chapter 2 (Section 2.2.3), the polarization properties of the biological tissue have been determined as phase retardation, diattenuation, and optical axis orientation. In addition, the previous section has introduced the similar-matrix relationship between the measurable output signals from OCT and the objective Jones matrix. Then, the eigenvalues and eigenvectors of the sample's Jones matrix are obtained indirectly. In this section, the approaches for the polarization properties measurement are briefly introduced.

3.2.2.1 Phase retardation

The phase retardation δ is determined by the two eigenvalues $\lambda_{1,2}$ of the similar Jones matrix, which has been described in quite a lot of papers of PS-OCT. The determinate formula is presented as:

$$\delta \equiv \mathrm{Arg}[\lambda_1/\lambda_2] = \arctan\left[\frac{Im(\lambda_1/\lambda_2)}{Re(\lambda_1/\lambda_2)}\right] \quad (11).$$

The parameters in this equation are spatial-resolved functions as well. The phase retardation δ obtained by this formula is the cumulative phase retardation of the round-trip from the surface to a measuring depth position of the sample. Another worthy notice of this method is that the phase retardation value obtained here is ambiguous, it is because the two eigenvalues λ_1 and λ_2 are selected arbitrarily. Therefore, the phase retardation imaging for biological tissues is displayed with a 0 to π rad range as

$$\delta' \equiv \begin{cases} \delta & : 0 \le \delta < \pi \\ 2\pi - \delta & : \pi \le \delta < 2\pi \end{cases} \quad (12),$$

where the δ' is the round-trip phase retardation of the sample.

3.2.2.2 Diattenuation

The diattenuation *d* is also defined by using the two eigenvalues λ_1 , λ_2 as the following formula:

$$d \equiv \frac{||\lambda_1|^2 - |\lambda_2|^2|}{|\lambda_1|^2 + |\lambda_2|^2} \quad (13).$$

Likewise, the diattenuation *d* is also a function of the 3D spatial coordinate. This value is usually negligible.

3.2.2.3 Optic-axis orientation

The optic-axis orientation is initially defined by the eigenvector of the sample's Jones matrix, which can be acquired by the eigenvalues mentioned above. This eigenvector is a Jones matrix of the similar matrix of the sample, which describes an invariable polarization state with the round-trip Jones matrix of the sample. Utilizing the Stokes vector converted from this Jones matrix, the optic-axis orientation can be represented in a Poincaré sphere. [1,7] Although similar matrixes have the same eigenvalues, their eigenvectors may be not the same. The eigenvector used to provide the optic-axis orientation is not an eigenvector of the round-trip matrix of the sample but is the eigenvector of a similar matrix of the sample. Hence, the optic-axis orientation obtained by this approach is not the actual optic-axis orientation, which contrasts the property of the sample. It is a relative optic-axis orientation. While, in 2012, a new calibration technique developed for a fiber-based JM-OCT, which enables the measurement of the absolute optic-axis orientation without ambiguity [9].

3.2.2.4 Degree of polarization uniformity

Besides the above mentioned three polarization properties, the depolarization is an additional polarization-change factor of the biological tissue, which is due to the multiple scattering effect of the tissue. However, it is not possible to measure the depolarization directly by OCT because of the intrinsic coherent-detection scheme of the OCT instrument [10]. The degree of polarization (DOP) can be used to describe the changes of the polarization state in tissue as a substitute of the depolarization. Nevertheless, it is impossible to be detected by the PS-OCT, because the DOP of the Jones vector is unity [10]. Some papers have demonstrated a new parameter, which is called degree of polarization uniformity (DOPU), enables the representation of DOP of the tissue. And further uses this parameter to study the depolarization effect of tissue.

The DOPU is originally calculated by the Stokes vectors. However, it is known that the Jones matrix is able to be converted into a Stokes vector by employing a virtual incident beam [11]. For example, if we introduce a virtual incident polarization state, such as $[1 \;\; 0]^T$, to illuminate the sample for simple calculation, the output Jones vectors becomes

$$\boldsymbol{E}_{out}\begin{bmatrix}1\\0\end{bmatrix}=\begin{bmatrix}J_{11}\\J_{12}\end{bmatrix} \quad (14),$$

where J_{11} and J_{12} are obtained by only two OCT signals from one PD detection (usually, there are two PD detections in JM-OCT). Therefore, the corresponding Stokes parameters can be written by these two elements of the similar matrix of the measured round-trip Jones matrix [$\boldsymbol{J}(z)\boldsymbol{J}(z_0)^{-1}=\boldsymbol{E}_{out}(z)\boldsymbol{E}_{out}(z_0)^{-1}$] as:

$$\boldsymbol{S}=\begin{bmatrix}I\\Q\\U\\V\end{bmatrix}\equiv\begin{bmatrix}|J_{11}|^2+|J_{12}|^2\\|J_{11}|^2-|J_{12}|^2\\J_{11}J_{12}^*+J_{11}^*J_{12}\\i(J_{11}J_{12}^*-J_{11}^*J_{12})\end{bmatrix} \quad (15).$$

Then, by using the definition of DOPU:

$$\mathrm{DOPU}=\frac{\sqrt{\bar{Q}^2+\bar{U}^2+\bar{V}^2}}{\bar{I}} \quad (16).$$

As mentioned above, DOP is not possible to be measured within one pixel in the OCT instrument, because the incident beam is completed polarization [10]. Consequently, in Eq. (16), the DOPU is calculated within a spatial averaging kernel or window by using the normalized Stokes parameters. In addition, Makita et al., further developed the noise-correction DOPU by the averaging statistical property of PS-OCT signals and multiple incident polarization states to achieve more accurate DOPU tomography.

3.2.3 Implementation of JM-OCT

Based on the above illuminated principle of JM-OCT, to implement the measurement by JM-OCT, in brief, two different incident polarization states (usually two orthogonal polarization states) and two measured Jones vectors of the backscattered beams are required. Hence, a polarization multiplexing mechanism and a polarization-diversity detection unit are necessary for the implementation of JM-OCT. There are several deferent approaches to realize the two polarization states illumination, multiplexing and polarization-diversity detection, such as time-division, polarization modulation, frequency shift, time-delayed incident polarization. In like manner, the Jones vector detection of JM-OCT also has several types adapt to the different configuration of the interferometers. For example, the spectrometer-based polarization-diversity is utilized for SD-OCT based PS-OCT, and the balance-photodetector-based polarization-diversity unit is specially designed for SS-OCT based PS-OCT. In this thesis, the multifunctional JM-OCT is an SS-OCT based PS-OCT. Thus, the two orthogonal incident polarized beams are produced and multiplexed by a time-delay based passive polarization delay unit (PPDU). The two different polarization states are kept multiplexing in the depth of the tissue with time delay caused by their different optical path lengths. And the interference signals are generated and

detected in the balance polarization-diversity detection unit (PDDU) that only one suitable detection for Swept-source-based JM-OCT. The interference signal is known to be expressed as

$$\boldsymbol{I} = \left|\boldsymbol{E}_p + \boldsymbol{E}_r\right|^2 = \left|\boldsymbol{E}_p\right|^2 + |\boldsymbol{E}_r|^2 + \boldsymbol{E}_p\boldsymbol{E}_r{}^* + \boldsymbol{E}_p{}^*\boldsymbol{E}_r \quad (17),$$

where $\boldsymbol{E}_p$ and $\boldsymbol{E}_r$ are the backscattered probe beam from sample and reference-beam from the reference arm, respectively. The third term of the interference signal expansion

$$\boldsymbol{E}_p\boldsymbol{E}_r{}^* = \begin{bmatrix} E_p^{(H)}E_r^{(H)*} \\ E_p^{(V)}E_r^{(V)*} \end{bmatrix} \quad (18),$$

is the Jones vector of the OCT signal acquired by the PDDU. Here, the superscripts (H) and (V) in the equation represents the horizontal and vertical components of the Jones vectors, which are detected by two detectors in PDDU. Moreover, the fourth term is the mirror signal of the measured OCT signal. Considering the two incident polarized beams illuminate the sample, actually, the complete four output OCT signals should be written as a 2x2 Jones matrix, such as

$$\boldsymbol{E}_p\boldsymbol{E}_r{}^* = \begin{bmatrix} \boldsymbol{E}_{oct}^{(1)(H)} & \boldsymbol{E}_{oct}^{(2)(H)} \\ \boldsymbol{E}_{oct}^{(1)(V)} & \boldsymbol{E}_{oct}^{(2)(V)} \end{bmatrix} \quad (19),$$

where the additional superscripts (1) and (2) represents the two different incident polarization states. Furthermore, some previous researches have demonstrated the unbalanced two polarization components of the reference beam and unevenness OCT signals of two of two incident polarization states do not affect the measurement result in the JM-OCT well aligned by the polarizers and polarization controllers in the system. Therefore, with this JM-OCT configuration, relatively high-speed and wide-range (depth) measurements can be achieved.

3.3 Extended theory of multifunctional JM-OCT

The JM-OCT based multifunctional OCT enables more contrast imaging than original JM-OCT within only one measurement by combing some additional analysis and processing of the four OCT signals obtained by JM-OCT.

3.3.1 Sensitivity-enhanced scattering OCT

The first contrast, scattering OCT is the fundamental function of OCT, which provides the morphology imaging for the biological tissue. However, in a JM-OCT, the four coherent signals from four channels, which correspond to the four entries of the measured Jones matrix, separated the power of the incident light into four parts. And in addition, in the traditional JM-OCT measurement, the scattering OCT was obtained by averaging the four entries of a Jones matrix. Therefore, the sensitivity of the scattering OCT image is degraded by using this method. To overcome this disadvantage of JM-OCT, a sensitivity-enhance scattering OCT image was introduced by MJ. Ju et al in 2013 [11]. In their method, the four interference signal entries are not processed to average, but are coherently composited by applying a mathematical model of the depth-resolved output Jones matrix, which is denoted as:

$$\boldsymbol{E}_p\boldsymbol{E}_r{}^{*} = \begin{bmatrix} \boldsymbol{E}_{out}^{(1)(H)}(z) & \boldsymbol{E}_{out}^{(2)(H)}(z) \\ \boldsymbol{E}_{out}^{(1)(V)}(z) & \boldsymbol{E}_{out}^{(2)(V)}(z) \end{bmatrix} \cong \begin{bmatrix} \boldsymbol{E}_{out}^{(1)(H)}(z) & e^{i\theta_1}\boldsymbol{E}_{out}^{(1)(H)}(z) \\ e^{i\theta_2}\boldsymbol{E}_{out}^{(1)(H)}(z) & e^{i\theta_3}\boldsymbol{E}_{out}^{(1)(H)}(z) \end{bmatrix} \quad (20),$$

where θ_i $(i = 1, 2, 3)$ represents the depth-independent relative phase offset of each other entries to the first one in the matrix. And these phase offsets are estimated by a complex argument of summed products of the other entry vectors and conjugate vector of the first entry. And this summation is for all pixels along the depth within the imaging range of the tissue. Then, using these three estimated phase offsets, the coherent composited OCT signal defined as

$$\overline{E_{out}}(z) = \frac{1}{4}\left[E_{out}^{(1)(H)}(z) + e^{-i\theta_1}E_{out}^{(1)(H)}(z) + e^{-i\theta_2}\boldsymbol{E}_{out}^{(1)(V)}(z) + e^{-i\theta_3}\boldsymbol{E}_{out}^{(2)(V)}(z)\right] \quad (21).$$

can be obtained. For the multi-contrast imaging, each position of the tissue is scanned 4 times in our measurement protocol. Thus, there are four B-frames of each position of the sample. After a noise correction, by summing up these four B-frames of OCT image with a global phase offset among them, and then a sensitivity-enhanced intensity OCT can be obtained as the following formula

$$I = \left| \sum_{j=n_0}^{n_0+n-1} \overline{E_{out}(z,J)}e^{\left(-i\Delta\varphi(z)^{(n_0,j)}\right)} \right|^2 \quad (22),$$

where z is the depth position of the measured sample, j is the index of B-scan, n_0 is the starting B-scan, n is the B-scan number, and $\Delta\varphi(z)^{(n_0,j)}$ is the global phase offset between each two estimated Jones matrices of the four B-scans.

3.3.2 Local birefringence imaging

JM-OCT was initially developed for measuring phase retardation or phase changes to assess the polarization property of the biological tissue. However, it has been demonstrated that the method of phase retardation measurement is difficult to provide accurate and high-quality contrast of the local tissue polarization property. Thus, a local birefringence imaging method was proposed by S. Makita et al [8]. To obtain accurate local birefringence, first, the fiber birefringence effect is ignored by setting the reference point at the surface of the sample (or a glass coverslip on the sample). Likewise, the birefringence of the tissue above the interested tissue position can be neglected by shifting the reference-point depth. Then the Jones matrix of the OCT signals from the local tissue can be written by using the Jones matrix of the one tissue point above. And the cumulative and round-trip Jones matrix of the sample can be expressed with the single-trip Jones matrix of the local tissue, i. e.,

$$\boldsymbol{J}_{S,T}(z_i) = [\boldsymbol{J}_S^T(z_1, z_2) \cdots \boldsymbol{J}_S^T(z_{i-1}, z_i)][\boldsymbol{J}_S(z_{i-1}, z_i) \cdots \boldsymbol{J}_S(z_1, z_2)] \quad (22),$$

where $\boldsymbol{J}_{S,T}(z_i)$ is the cumulative round-trip Jones matrix of the sample, $\boldsymbol{J}_S(z_i, z_{i+1})$ $(i = 1, 2, 3, \cdots)$ is the single-trip Jones matrix of the local tissue correspond the depth range from z_i to z_{i+1}. According to the principle of JM-OCT, a similar Jones matrix denoted as $\boldsymbol{M}(z_{i-n-1}, z_i)$ of the local tissue round-trip Jones matrix $\boldsymbol{J}_S(z_{i-n}, z_i)$ corresponding to the tissue depth range from z_{i-n} to z_i can be obtained. Thus, the eigenvalues and eigenvector matrix of $\boldsymbol{M}(z_{i-n-1}, z_i)$ is possible to be calculated by the diagonalized matrix of $\boldsymbol{M}(z_{i-n-1}, z_i)$. As mentioned above, the phase retardation is defined by the eigenvalues $\lambda'_{1,2}$. Similarly, the local phase retardation is also determined by the eigenvalues of the similar matrix of local tissue, i. e.,

$$\delta'(z_{i-n}, z_i) \equiv \mathrm{Arg}[\lambda'_1/\lambda'_2] = \left|\arctan\left[\frac{Im(\lambda'_1/\lambda'_2)}{Re(\lambda'_1/\lambda'_2)}\right]\right| \quad (23).$$

If there is no diattenuation effect of the sample arm and measured tissue, Jones matrix of the local tissue and output matrix are unitary. Thus, the local phase retardation also can be calculated by the following equation:

$$\delta'(z_{i-n}, z_i) = 2\cos^{-1}\frac{|tr\boldsymbol{M}|}{\sqrt{2tr(\boldsymbol{M}^*\boldsymbol{M})}} \quad (24),$$

where *tr* represents the trace of the matrix, $\boldsymbol{M}$ is the similar Jones matrix of the local tissue, and $\boldsymbol{M}^*$ is the complex conjugate matrix of $\boldsymbol{M}$. Furthermore, the local birefringence *b* can be obtained by using the local phase retardation as

$$b(z_{i-n}, z_i) = \frac{\delta'(z_{i-n}, z_i)}{2k_c\Delta z} \quad (25),$$

where k_c is the wavenumber corresponding to the center wavelength of the light source, and $\Delta z = z_i - z_{i-n}$ is the thickness of the local tissue. The number '2' means the calculation is for the round-trip of the measured tissue. With this method, high contrast local birefringence can be obtained by a large depth

separation of the tissue, which corresponds to Δz, at the expense of axial resolution. Thus, the setting of Δz should balance the contrast of the birefringence and the axial resolution for high quality imaging.

In addition, the SNR is an important factor associated with the performance of birefringence imaging. Hence, the systematic error caused by background noise in phase retardation measurement was estimated by a local Jones matrix analysis method. And then the measured phase retardation r_m was expressed by three parameters as:

$$r_m = 2\cos^{-1}\left[\frac{\sqrt{\cos^2\frac{r}{2} + \gamma^{-1}\csc^2\frac{\zeta}{2}}}{\sqrt{1 + 4\gamma^{-1}\csc^2\frac{\zeta}{2}}}\right] \quad (26),$$

where r is the true phase retardation, γ represents the effective SNR (ESNR), and ζ denotes the angle between the two input polarization states on a Poincaré sphere. Here, the ESNR of the measured phase retardation is described as:

$$\gamma(z) = \mathrm{ESNR}(z_{i-n}, z_i)$$

$$= \left[\frac{1}{4}\left(\frac{1}{\mathrm{SNR}^{(1)}(z_{i-n})} + \frac{1}{\mathrm{SNR}^{(2)}(z_{i-n})} + \frac{1}{\mathrm{SNR}^{(1)}(z_i)} + \frac{1}{\mathrm{SNR}^{(2)}(z_i)}\right)\right]^{-1} \quad (27),$$

where the ESNR (r) is a function of the variable depth (z), z_{i-n}, z_i represent adjacent two depth positions of the reference and measurement tissue points, respectively, the superscripts (1), (2) represent the first and second incident beams, respectively. This ESNR can be utilized to evaluate the accuracy of the measured phased retardation. And moreover, it showed the limitation of the previous phase retardation (also local birefringence) measurement, which is difficult to obtain the true phase retardation. Therefore, to achieve the probability distribution of true local birefringence measurement, in our multifunctional JM-OCT, a maximum-a-posteriori (MAP) estimation of the birefringence has been applied as well. [12]

Since the local birefringence measurement is affected by the background noise, the local Jones matrix of the measured tissue should be modified with an additive noise matrix as

$$\boldsymbol{J}'_{all}(z, \Delta z) = [\boldsymbol{J}_{all}(z_2) + \boldsymbol{N}(z_2)][\boldsymbol{J}_{all}(z_1) + \boldsymbol{N}(z_1)]^{-1} \quad (28),$$

where

$$\boldsymbol{N}(z) = \begin{bmatrix} n_1(z) & n_2(z) \\ n_3(z) & n_4(z) \end{bmatrix} \quad (29)$$

is a matrix, which consists of four random complex noises corresponding to the four-channel OCT signals. The four elements of the noise matrix are independent with each other and obey zero-mean Gaussian distribution. Usually, the local phase retardation (and/or local birefringence) is obtained by this local Jones matrix. However, the phase retardation derived from the local Jones matrix with additive noise is no longer linear, and its distribution is neither Gaussian nor systematic. Hence, the distribution of the phase retardation becomes too complex to be analyzed directly, and the true birefringence is difficult to be estimated. Form the Eq. (26), the measured birefringence is known to be defined by the parameters of the true birefringence, ESNR, and the angle between two input polarization states on a Poincaré sphere (ζ). It should be noted that the parameter ζ only depends on the system design. It means this parameter is a constant in a phase retardation measurement with a certain JM-OCT. Therefore, the measured phased retardation only determined by two independent parameters: true phase retardation and ESNR. Based on this knowledge, Kasaragod et al, proposed to use the true birefringence probability distribution for providing the estimation of the true local birefringence. Although the probability distribution is impossible to be obtained directly, by applying the Bayes' theorem, the proportional relation between the true birefringence probability distribution and the distribution function of the measured local birefringence is provided as

$$p(\beta; b, \gamma) \propto f(b;\ \beta, \gamma)\pi(\beta) \quad (30),$$

where $p(\beta; b, \gamma)$ is the probability distribution of the true birefringence, $f(b;\ \beta, \gamma)$ is a function represents the probability distribution of the measured local birefringence at a specific value of the true birefringence and a specific ESNR, b, β, γ respectively represent the measured birefringence, true birefringence, and ESNR. The $\pi(\beta)$ is the *prior* distribution, which represents a *priori* knowledge of the true birefringence probability distribution. Because β only can be obtained under the condition of that the b and γ have been measured, formula (30) should be substituted by using a proper likelihood function, $f(\beta;\ b, \gamma)$, of β as

$$p(\beta; b, \gamma) \propto f(\beta;\ b, \gamma)\pi(\beta) \quad (31).$$

Formula (31) suggests that, to find out the true birefringence probability distribution $p(\beta; b, \gamma)$, the likelihood function $f(\beta;\ b, \gamma)$ has to be predefined first. To predefine the function $f(\beta;\ b, \gamma)$, A Monte-Carlo statistic simulation method is used to provide a set of distribution functions $f(b;\ \beta, \gamma)$ with several values of β and γ. One set of Monte-Carlo calculations consists of a mass of trails, each trial in it is implemented by using the two measured Jones matrixes in Eq. (28) with Gaussian noises. Then the specific true birefringence β and specific ESNR γ are obtained to simulate the measured birefringence b. Consequently, a distribution function of simulated b can be provide by one set of Monte-Carlo calculation. The Monte-Carlo calculations set repeats quite a lot of times by varying the values of β and γ with a proper resolution of them in their ranges correspond to the range of phase retardation ($0 - \pi\, rad$) under a selected depth separation. Sequentially, a set of distribution functions $f(b;\ \beta, \gamma)$ represented as a 3D numerical array can be generated. Furthermore, by utilizing a Lanczos interpolation, the likelihood function $f(\beta;\ b, \gamma)$ is figured out. With this likelihood

function, the *posterior* distribution of the true birefringence for N measurements $p_N(\beta)$ can be expressed based on the formula (31) as

$$p_N(\beta) \equiv p\,(\beta; b, \gamma)|_{(b,\gamma)=(b_1,\gamma_1),\cdots(b_N,\gamma_N)} \propto \prod_{i=1}^{N} f(\beta; b_i, \gamma_i) \quad (32).$$

Finally, the Bayesian maximum likelihood estimation (mle) after N measurements is provided by the following equation:

$$\hat{\beta}|_{(b_1,\gamma_1),\cdots(b_N,\gamma_N)} \equiv \arg\max_{\beta} \prod_{i=1}^{N} f(\beta; b_i, \gamma_i) \quad (33).$$

In addition, the reliability of the estimation can be measured by the value calculated from the local likelihood integral around the estimated true birefringence

$$\mathcal{L}\left(\hat{\beta};\, \Delta\beta\right) = \int_{\hat{\beta}-\Delta\beta/2}^{\hat{\beta}+\Delta\beta/2} p_N(\beta) d\beta \quad (34).$$

This value can be used to produce a pseudo-color image of local birefringence, which is capable of providing high contrast of the specific characteristic for the biological tissues.

Before the practical biological tissue measurement, the validities of this methods has been proved by testing a series of optical components with prescient phase-retardation, such as a non-birefringent glass plate, a quarter waveplate, and a one-eighth waveplate, which had round-trip phase retardations of 0, $\pi/2$, and π rad, respectively. In addition, since the birefringence of the quarter and one-eighth waveplates do not fit the set true birefringence range of the numerically calculated likelihood function, which was mentioned above, the tailored likelihood functions were numerically generated for the quarter and one-eighth waveplates and the glass plate validations. Thereby, the true birefringence values can fit the range of phase-retardation, which is from 0 to π. The results of the experimental validations with the known birefringent and non-birefringent materials and the numerical simulations demonstrated the local birefringence method works well [12,13].

3.3.3 Noise-corrected DOPU imaging

As mentioned in section 3.2.2, DOPU is an additional function extended to PS-OCT, which is potential to study the depolarization effect of the tissue. Especially, DOPU measurement enables the visualization of *in vivo* pigmented tissue, such as retinal pigment epithelium (RPE) of the ocular tissue. Since the noise influence on the accuracy of the local birefringence measurement has been illuminated in the last section. Thereby, the noise-correction treatment is also necessary for the DOPU measurement. Similarly, to achieve noise-corrected

DOPU imaging, the Stokes parameters derived from the Jones matrixes of the JM-OCT measured signals should be modified with an additive noise as

$$\begin{bmatrix} s_0' \\ s_1' \\ s_2' \\ s_3' \end{bmatrix} = \begin{bmatrix} |g_H|^2 + |g_V|^2 - \left(\overline{|n_H|^2} + \overline{|n_V|^2}\right) \\ |g_H|^2 - |g_V|^2 - \left(\overline{|n_H|^2} - \overline{|n_V|^2}\right) \\ 2Re[g_H g_V^*] \\ 2Im[g_H g_V^*] \end{bmatrix} \quad (34).$$

Equation (34) is a bias-free estimation of true Stokes parameters. Thus, the DOPU with noise-correction can be redefined with the noise-corrected Stokes parameters based on Eq. (16) as

$$\mathrm{DOPU} = \frac{\sqrt{\sum_{v=1}^{3} \overline{s_v'}^2}}{\overline{s_0'}} \quad (35),$$

where $\bar{s}$ means averaging of $\bar{s}$ at a local space. In JM-OCT based PS-OCT, there are two input polarization states, and hence two multiple pairs of polarization-sensitive OCT signals from four channels are detected by a PPDU. For this property of JM-OCT, the noise effect can be further reduced by the combined DOPU with two input polarization states. Finally, the DOPU with multiple incident polarization states obtained by JM-OCT can be calculated by the following equation

$$\mathrm{DOPU}' = \frac{\sum_{m=1}^{M} w^{(m)} \sum_{v=1}^{3} \overline{s_v^{(m)\prime}}^2}{\sum_{m=1}^{M} w^{(m)} \overline{s_0^{(m)\prime}}} \quad (36).$$

3.3.4 Noise-corrected correlation mapping OCT-A

To obtain a high-contrast OCT angiography by JM-OCT, a noise-corrected complex correlation method is applied. In this method, to achieve high-accuracy OCT-A measurement, first, the OCT signal from each channel of JM-OCT is corrected with a random additive noise. And then, refer to the Ref [14], the correlation between measured OCT signals (ρ_G) at different spatiotemporal points ($\mathbf{r}$) and ($\mathbf{r} + \Delta\mathbf{r}$) can be expressed by the correlation coefficient of measured OCT signals (ρ_S) and a decorrelation factor caused by the random noise (ρ_{SNR})

$$\rho_G(\Delta\mathbf{r};\ \mathbf{r}) = \rho_{\mathrm{SNR}}(\Delta\mathbf{r};\ \mathbf{r})\rho_S(\Delta\mathbf{r};\ \mathbf{r}) \quad (37),$$

where

$$\rho_s(\Delta\mathbf{r};\ \mathbf{r}) = \frac{\mathrm{E}[S^*(\mathbf{r}) + S(\mathbf{r}+\Delta\mathbf{r})]}{\sqrt{\mathrm{E}[|S(\mathbf{r})|^2]}\sqrt{\mathrm{E}[|S(\mathbf{r}+\Delta\mathbf{r})|^2]}} \quad (38),$$

$$\rho_{SNR}(\Delta\mathbf{r};\ \mathbf{r}) = \left[\sqrt{1+\mathrm{SNR}(\mathbf{r})^{-1}}\sqrt{1+\mathrm{SNR}(\mathbf{r}+\Delta\mathbf{r})^{-1}}\right]^{-1} \quad (39).$$

In the statistical noise-corrected correlation estimation, the bias and variance indicate that the large variance leads to the low-accuracy imaging with the noise. Thus, to achieve the low-bias and low noise complex correlation estimation, a time-averaged noise power technique combined with an additional averaging window is applied. Here, the noise is measured without OCT signal and is assumed to be identical in space. Then, a SNR-corrected low-noise signal correlation estimate can be expressed as

$$\overline{r_s}(\Delta\mathbf{r};\ \mathbf{r}) \equiv \frac{\langle s_{G12}\rangle_{w_2}}{\langle\varepsilon\sqrt{|[s_{G11}-\hat{q}_N][s_{G22}-\hat{q}_N]|}\rangle_{w_2}} \quad (40),$$

where $s_{Gij}, (i=1,2; j=1,2)$ represents the entry of the estimated covariance matrix at *i*-row and *j*-column, $\hat{q}_N \equiv \langle|g_n(t)-\langle g_n(t)\rangle_t|^2\rangle_t$ is a time-averaged noise power, which is obtained from the OCT signal $[g_n(t)]$ without sample, $\langle\ \rangle_{w_2}$ denotes the averaging window w_2. A sign function ε expressed as

$$\varepsilon = \frac{\mathrm{sgn}(s_{G11}-\hat{q}_N)+\mathrm{sgn}(s_{G22}-\hat{q}_N)}{2} \quad (41).$$

is applied in Eq. (40) to reduce the bias of the correlation estimate after averaging when there is no signal in the region.

To implement the OCT-A measurement in JM-OCT system, the B-scan is repeated several times at the same location in sample. Since each B-scan contains four OCT signals, which are the four entries of the Jones matrix of the measured signal, the enhanced scattering intensity OCT first obtained by coherently compositing the four OCT signals as mentioned in section 3.3.1. Then, the temporal correlation between two time points $(t, t+\tau)$ at the same spatial location $(\boldsymbol{x}, z)$ is denoted as $\rho_s(\Delta\mathbf{r};\ \mathbf{r})|_{\Delta\boldsymbol{r}=(\mathbf{0},0,\tau)}$. During, the temporal correlation coefficient estimating, the temporal averaging utilized to obtain the spatial distribution of true OCT signal correlation coefficient, which is expressed as

$$\overline{r_s}(\tau;\boldsymbol{x},z) \equiv \frac{\langle\left|\langle g(\mathbf{r})g^*\left(\mathbf{r}+(\mathbf{0},0,\tau)\right)_{w_1}\rangle\right|\rangle_{w_2}}{\langle\varepsilon\sqrt{\left|\left[\langle|g(\mathbf{r})|^2\rangle_{w_1}-\hat{q}_N\right]\left[\langle|g(\mathbf{r}+(\mathbf{0},0,\tau)|^2\rangle_{w_1}-\hat{q}_N\right]\right|}\rangle_{w_2}} \quad (42).$$

Thereby, the high-contrast OCT-A (blood flow image) can be obtained.

3.4 Advantages and application of multifunctional JM-OCT

The multifunctional JM-OCT has been demonstrated to be capable of providing some specific contrasts of biological samples such as collagen property, melanin concentration, and vasculature. And there are several papers have presented the usefulness of multifunctional JM-OCT for ophthalmologic imaging. Along with the development of JM-OCT technique, nowadays, multifunctional JM-OCT has been well applied in ophthalmology investigation with its special characteristics. For example, it possesses a highly phase stabilized system, has capabilities of obtaining several polarization parameters of the biological sample and generates the corresponding multi-contrast images of the sample simultaneously. By utilizing these different specific contrasts, the disease or damaged tissue locations of eyes can be observed and investigated. In addition, the measurement time and accuracy were also advanced due to its particular theory. A set of multi-contrast images of eye obtained from JM-OCT are shown in Fig. 2.4 as an example [3]. By using multifunctional JM-OCT, the different microstructures of ocular tissue, such as retinal and choroidal vessels, choroid-sclera interface,

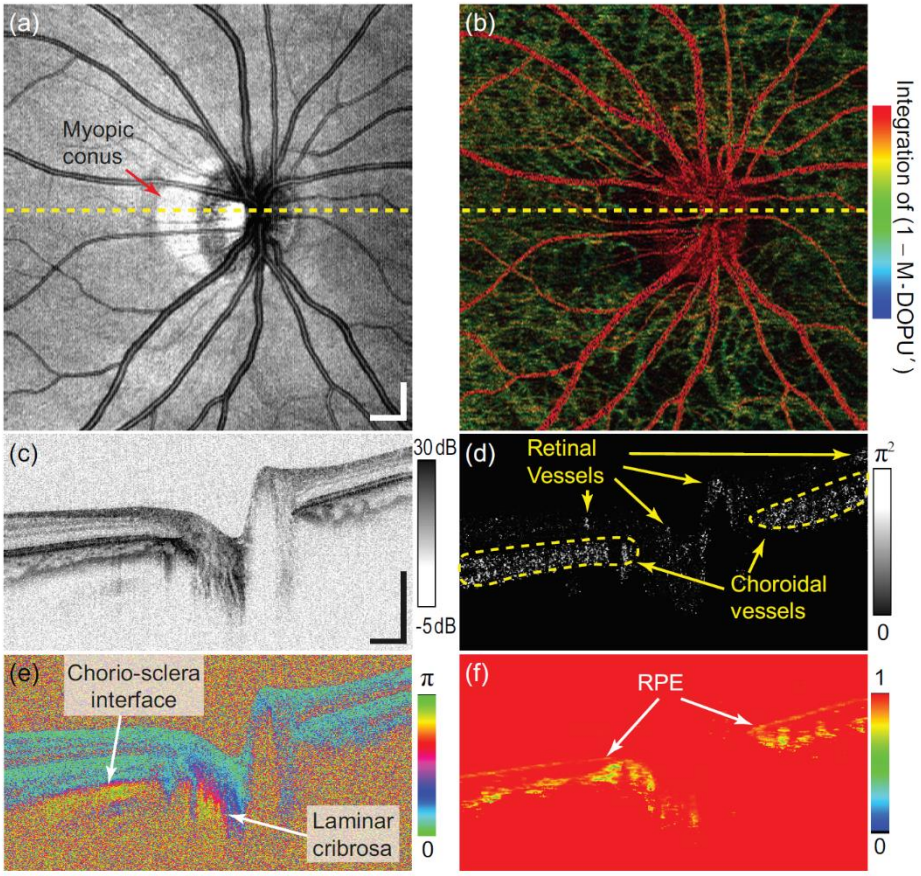

Figure 3.2: Multifunctional OCT images of *in vivo* human optic nerve head. (a), (c) *En face* projection and a cross-sectional image of scattering intensity OCT, respectively, (b) an *en face* pseudo-color image composite of power Doppler and M-DOPU, (d)–(f) cross-sectional power Doppler, phase retardation, and M-DOPU images. [3]

lamina cribrosa, and pigmented tissue (RPE: retinal pigment epithelium), can be visualized and discriminated clearly.

3.5 Summary

In this chapter, the theoretical basis of JM-OCT and multifunctional JM-OCT are introduced in detail. On the one hand, JM-OCT is essentially one form of PS-OCT and aims at measuring the polarization of the interest of tissue, such as phase-retardation, diattenuation, optic-axis orientation, and etc., by which further birefringence of the microstructures or some chemical compositions in tissue could be achieved. On the other hand, JM-OCT based multifunctional OCT, as an extension technology of JM-OCT, enables more contrast imaging than original JM-OCT within only one measurement by combing some additional analysis and processing of the four OCT signals obtained by JM-OCT. The methods to obtain above-mentioned four images by one multifunctional JM-OCT scan are theoretically introduced in this chapter. Four OCT signals including sensitivity-enhanced scattering OCT, local birefringence imaging, noise-corrected DOPU imaging, and noise-corrected correlation mapping OCT-A could be simultaneously created by single scan, which allows one to get more comprehensive information of tissue in a high-efficient and cost-effective way.

References

1. B. H. Park, M. C. Pierce, B. Cense, and J. F. de Boer, "Real-time multi-functional optical coherence tomography," Opt. Express **11**(7), 782–793 (2003).

2. Y. Lim, Y.-J. Hong, L. Duan, M. Yamanari, and Y. Yasuno, "Passive component based multifunctional Jones matrix swept source optical coherence tomography for Doppler and polarization imaging," Opt. Lett. **37**(11), 1958–1960 (2012).

3. Y.-J. Hong, S. Makita, S. Sugiyama, and Y. Yasuno, "Optically buffered Jones-matrix-based multifunctional optical coherence tomography with polarization mode dispersion correction," Biomed. Opt. Express **6**(1), 225–243 (2015).

4. S. Sugiyama, Y.-J. Hong, D. Kasaragod, S. Makita, S. Uematsu, Y. Ikuno, M. Miura, and Y. Yasuno, "Birefringence imaging of posterior eye by multi-functional Jones matrix optical coherence tomography," Biomed. Opt. Express **6**(12), 4951–4974 (2015).

5. R. C. Jones, "A New Calculus for the Treatment of Optical SystemsI. Description and Discussion of the Calculus," JOSA **31**(7), 488–493 (1941).

6. B. H. Park, M. C. Pierce, B. Cense, and J. F. de Boer, "Jones matrix analysis for a polarization-sensitive optical coherence tomography system using fiber-optic components," Opt. Lett. **29**(21), 2512–2514 (2004).

7. B. H. Park, M. C. Pierce, B. Cense, and J. F. de Boer, "Optic axis determination accuracy for fiber-based polarization-sensitive optical coherence tomography," Opt. Lett. **30**(19), 2587–2589 (2005).

8. S. Makita, M. Yamanari, and Y. Yasuno, "Generalized Jones matrix optical coherence tomography: performance and local birefringence imaging," Opt. Express **18**(2), 854–876 (2010).

9. Z. Lu and S. J. Matcher, "Absolute fast axis determination using non-polarization-maintaining fiber-based polarization-sensitive optical coherence tomography," Opt. Lett. **37**(11), 1931–1933 (2012).

10. S. Jiao, G. Yao, and L. V. Wang, "Depth-resolved two-dimensional Stokes vectors of backscattered light and Mueller matrices of biological tissue measured with optical coherence tomography," Appl. Opt. **39**(34), 6318–6324 (2000).

11. M. J. Ju, Y.-J. Hong, S. Makita, Y. Lim, K. Kurokawa, L. Duan, M. Miura, S. Tang, and Y. Yasuno, "Advanced multi-contrast Jones matrix optical coherence tomography for Doppler and polarization sensitive imaging," Opt. Express **21**(16), 19412–19436 (2013).

12. D. Kasaragod, S. Makita, S. Fukuda, S. Beheregaray, T. Oshika, and Y. Yasuno, "Bayesian maximum likelihood estimator of phase retardation for quantitative polarization-sensitive optical coherence tomography," Opt. Express **22**(13), 16472–16492 (2014).

13. D. Kasaragod, S. Makita, Y.-J. Hong, and Y. Yasuno, "Noise stochastic corrected maximum a posteriori estimator for birefringence imaging using polarization-sensitive optical coherence tomography," Biomed. Opt. Express **8**(2), 653–669 (2017).

14. S. Makita, F. Jaillon, I. Jahan, and Y. Yasuno, "Noise statistics of phase-resolved optical coherence tomography imaging: single-and dual-beam-scan Doppler optical coherence tomography," Opt. Express **22**(4), 4830–4848 (2014).

Chapter 4

Multifunctional JM-OCT for dermatology

4.1 Introduction

Optical coherence tomography (OCT) is a noninvasive, high resolution, and fast imaging modality that is capable of visualizing the internal micro-structures of *in vivo* tissue [1]. Because of these particular advantages, OCT has been applied in several medical fields such as ophthalmology [2,3], cardiology [4], gastroenterology [5], dentistry [6], and dermatology [7–10]. Among them, dermatology is a suitable field for OCT because skin is easily accessible and consists of several sub-millimeter internal structures.

Skin consists of a significant amount of collagen, which is a birefringent material. In addition, some skin diseases, such as scleroderma, are believed to be associated with collagen abnormality [11,12]. Hence, birefringence measurement would be useful for pathological investigation. Furthermore, some research has found that skin blood flow relates to diabetes and peripheral vascular disease [13,14]. This suggests that non-invasive angiography would be able to provide useful information for diagnosing diabetes and vascular disease.

There are some functional extensions of OCT that have been applied to dermatological investigations [15–20]. Among them, polarization sensitive OCT (PS-OCT) [16,17,19], OCT angiography (OCT-A) [15], and its combination [21] are the most promising options. Currently, most dermatological PS-OCT measures phase retardation to detect the polarization property of the skin. However, it was recently argued that the phase retardation measurement is not accurate for biological tissues with non-uniform optic axis orientation along its depth, which includes skin [22]. Therefore, a depth-localized birefringence measurement is required for more accurate dermatological investigation. The limitation of cumulative phase retardation imaging can be overcome by the birefringence measurement based on localized Jones matrix measurement [23–25]. Although the local Jones matrix measurement suffers from a low signal-to-noise ratio (SNR), inaccurate phase-retardation and birefringence, these problems were recently resolved by birefringence and phase retardation estimation techniques that include the coherent averaging of the Jones matrix and/or Jones vector [26–28], eigenvalue-based averaging [29], Jones matrix estimation based on the Cloude-Pottier decomposition [30], Muller analysis [31,32], a specially designed phase-retardation estimation function [33], and maximum a posteriori birefringence estimators [25,34,35]. These advances enabled the birefringence imaging of *in vivo* skin. The uniformity of polarization property of tissue is also useful for dermatological investigation [36]. It was recently applied to investigate hypertrophic scars [37]. OCT-A has also been applied to dermatological investigations. This method enables the non-invasive visualization of the internal vascular structure *in vivo* [38,39].

In this chapter, we demonstrate our new multifunctional (multi-contrast) Jones matrix optical coherence tomography (JM-OCT) for dermatological imaging. It enables the simultaneous investigation of the polarization and flow properties of skin. The JM-OCT simultaneously provides depth-resolved birefringence (local phase retardation) tomography [25], degree-of-polarization-uniformity (DOPU) [40,41], complex-correlation based OCT-A [42], and the scattering intensity OCT. The system is based on a design that is similar to our previous passive-polarization-delay based posterior-eye JM-OCT [22,27], but is specially redesigned for dermatological investigation. The performance of the system is demonstrated by measuring different skin

tissues *in vivo*.

4.2 Method

4.2.1 System

The dermatological JM-OCT system was built from the passive-polarization-delay-based PS-OCT [22,27,28,43,44]. The schematic of our JM-OCT is shown in Fig. 4.1(a). The light source is a MEMS-based wavelength sweeping laser source (AXA10823-8, Axsun Technologies, MA) with a center wavelength of 1310 nm, an average output power of 22.6 mW, and a scanning rate of 49,600 Hz. The light is first divided by a 90:10 broadband coupler (FC1310-70-10-APC, Thorlabs Inc., NJ) such that 90% goes to the sample arm, and the other 10% goes to the reference arm.

In the sample arm, the beam goes to a passive polarization delay (PPD) module. The PPD module used in this system has a configuration that is similar to the one in [22, 27], but all the optical components are miniaturized and encased in a small box (91 mm × 50 mm footprint and 30 mm height). This compact PPD module (DE-G043-13, Optohub Co. Ltd., Saitama, Japan) was collaboratively developed with Optohub Co. Ltd. and is commercially available. In the PPD module, the beam is split into two orthogonal independent polarizations states by a broadband polarizing beam-splitter cube (PBS). A linear polarizer is placed just before the PBS to control the splitting ratio. The split beams are recombined by another PBS and sent to the fiber output of the PPD module. Different delays are applied to the two polarizations before recombination. This mutual delay results in the depth-multiplexing of the two incident polarizations in the resulting OCT image [22,27]. The output power of the PPD is maximized by a fiber polarization controller just before the PPD module (PC1), i.e., just before the polarizer. The output from the PPD module goes to a bulk probe arm through a broadband circulator (CIR-1310-50-APC, Thorlabs). The back scattered light from the sample passes a polarization controller (PC2) and the circulator, and it is sent to a polarization-diversity-detection module (PD-detector, DE-G036-13, Optohub).

In the probe unit, the beam is first collimated by a fiber-tip collimator (beam diameter = 3.49 mm, type number PAF-X-18-C, Thorlabs), passes a two dimensional galvanometric scanner (model 6220, Cambridge Technology Inc., MA), and focused by an objective (effective focal length = 36 mm, working distance = 25.1 mm, type number LSM03, Thorlabs). The $1/e^2$ beam diameter at the beam waist is 18 μm and the depth of focus is 389 μm. To reduce the skin surface reflection causing signal saturation, a tilted glass slip was attached in front of the probe unit as shown in Fig. 4.1(b). The space between the glass slip and the sample (skin) is filled by the ultrasound gel for refractive index matching. The probe unit is identical to that used in Ref. [45].

In addition, 10% of the power from the light source is sent to the reference arm of the interferometer. In the reference arm, the light is first sent to a fiber Bragg grating (FBG, FBG-SMF-1266-80-0.2-A-(2)60F/E, L = 1M, reflectivity 80%, Tatsuta Electric Wire & Cable Co., Ltd, Osaka, Japan). The light is reflected sharply

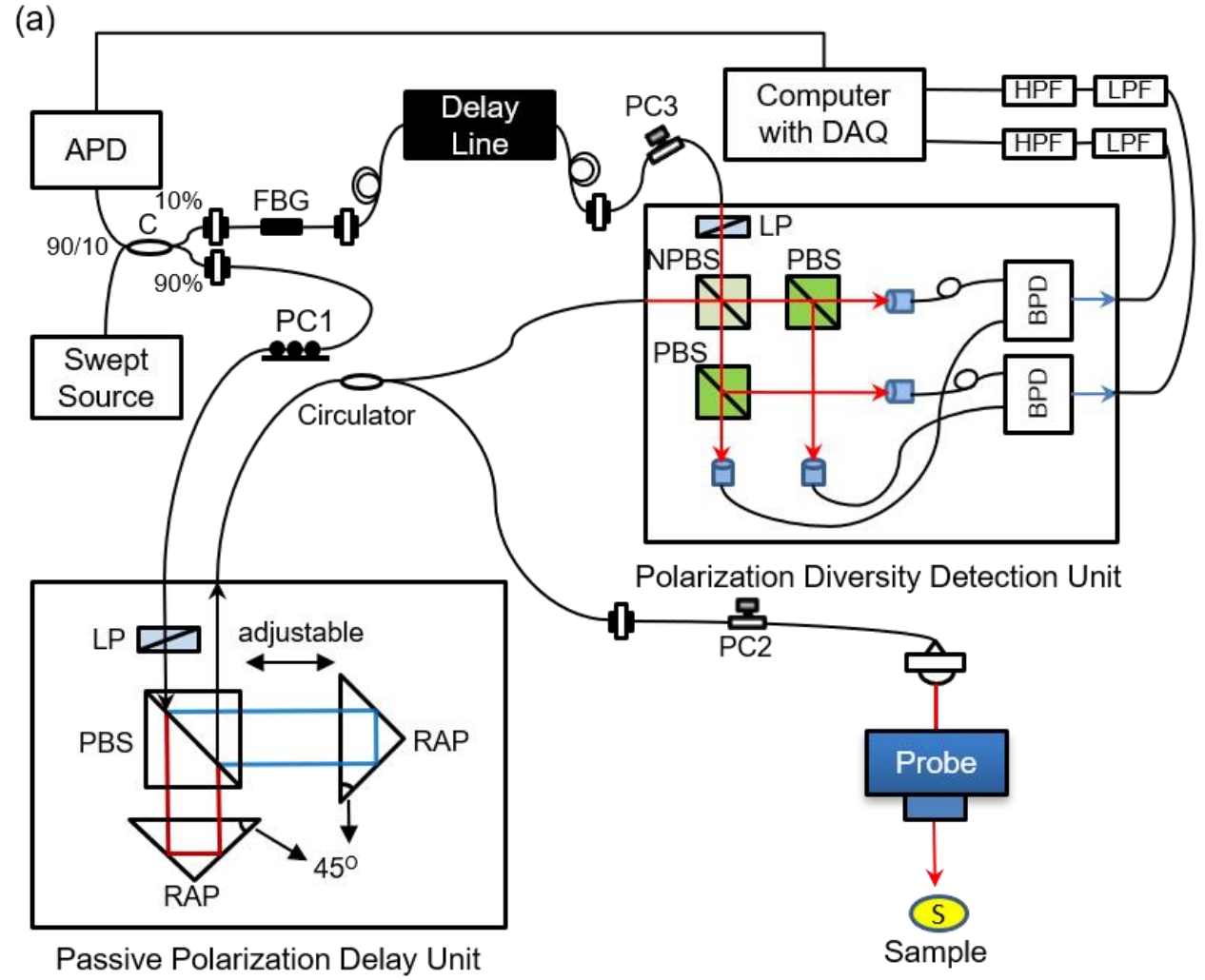

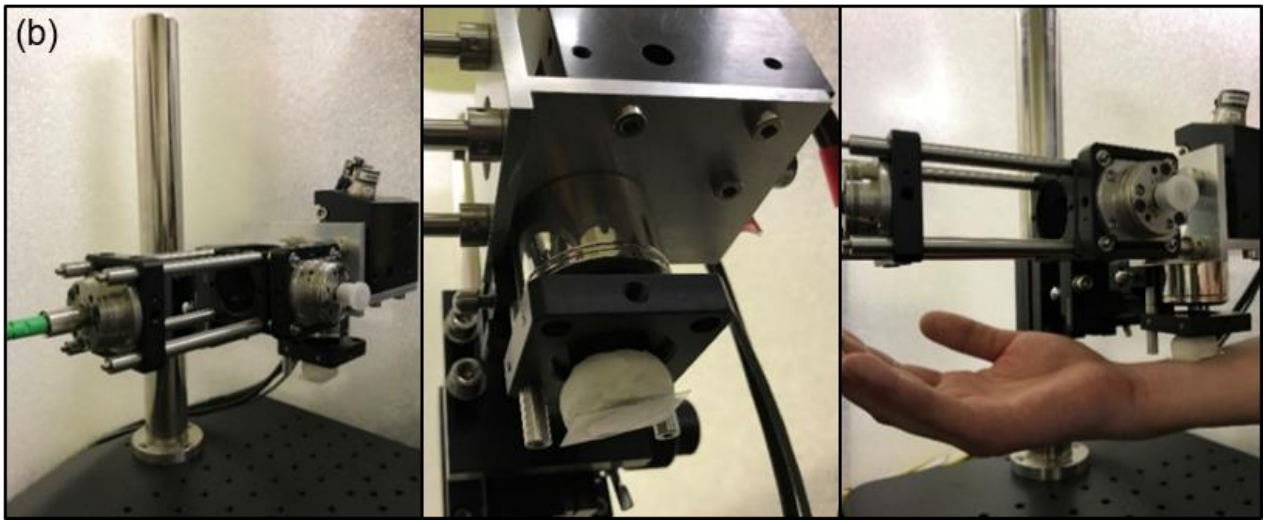

Figure 4.1: (a) Configuration of the Jones matrix OCT system. APD: amplified photodetector; C: coupler; PC1, PC2 and PC3: polarization controllers; LP: linear polarizer; PBS: polarizing beam splitter; RAP: right angle prism; S: sample; NPBS: non-polarization beam splitter; BPD: balanced photodetector; LPF: low pass filter, and HPF: high pass filter. (b) Pictures of scanning probe for skin.

at 1266-nm, and the reflected light is detected by an amplified photodetector (PDA10CF, Thorlabs). The amplified photodetector output is sent to a digitizer (ATS9350, Alazar Technologies Inc., Quebec, Canada) and used as a trigger for each A-line acquisition. The light passing the FBG goes to the reference arm and is sent to the PD-detector through a variable optical delay line (Advanced Fiber Resource Ltd., Hong Kong, China).

In the PD-detector, the reference and probe beams are combined by a non-polarization beam splitter (NPBS) and generate an interference signal. The interference signal is split into two polarization components by two PBSs, and these polarization components are independently detected by two balanced photodetectors. In the reference path of the PD-detector, a polarizer is located just before the NPBS, which balances the reference powers between the two detection polarization channels. The total reference power is optimized by a polarization controller just before the PD-detector (PC3). In contrast to our previous JM-OCTs [22,27,44], the PD-detector in the present system is an encased detection module with a compact size of 156 mm (width) × 105 mm (depth) × 34 mm (height), which includes not only miniaturized bulk optics but also two balanced photodetectors. Because of the encased PD-detector and PPD module, the system is built using only non-bulk components except for the probe head.

The detected interference signals are sent to the digitizer after passing through a high-pass filter (1 MHz cutoff frequency, Chebyshev type, HP1CH3, R&K Co., Ltd., Shizuoka, Japan) and a low-pass filter (62 MHz cutoff frequency, Chebyshev Type, LP62CH3, R&K Co., Ltd., Shizuoka, Japan) of each channel of the two output . Each spectral interference signal is sampled at 1,152 points and the optical bandwidth to be sampled is 106 nm. The sampling is performed with a built-in k-clock generated by the light source.

The OCT signals are generated from the Fourier transform of the interference signals. Fixed pattern noise was removed by complex median subtraction method [46]. Because two incident polarizations are multiplexed by the PPD and two detection polarizations are independently detected by the PD-detector, this process provides a set of four complex OCT images. This set of OCT images forms a Jones matrix tomography, which is mathematically similar to the round-trip Jones matrix of the sample. The Jones matrix tomography formation is identical to the process described in our previous publications [22,27], but with the following exceptions. In the present system, we apply intensity correlation based sub-pixel depth-shift correction among four images, which was not used in the previous JM-OCT. For this sub-pixel shift, each intensity image of four polarization channels are enlarged along the depth with fast Fourier transform (FFT) based interpolation algorithm with 7-times of zero-padding. 1-D image correlations along the depth are computed among the four images. This correlation provides depth-shifts of each A-line. The shift between images is then defined as the median of the set of depth-shifts. In contrast, the numerical phase stabilization that is used in the previous system is not applied here because the phase has been stabilized by the k-clock.

4.2.2 Performance of system

Probe power

As mentioned above, the probe power was well adjusted by the polarization controller and the polarizer. After optimizing the optical system, the incident power to the sample is around 10.2 mW, which is much lower than maximal permissible exposure limited by ANSI standard. It means this power value of the probing beam is safe for skin.

Reference power

For the reference power, in order to find out the most appropriate signal-noise ratio (SNR) and sensitivity, it is necessary to measure the sensitivity corresponding to the reference power changed by a certain step. The trend of sensitivity changing with reference power is shown as Fig. 4.2. In addition, the noise increases with the reference power. Therefore, the reference power was set at around 0.9 mW.

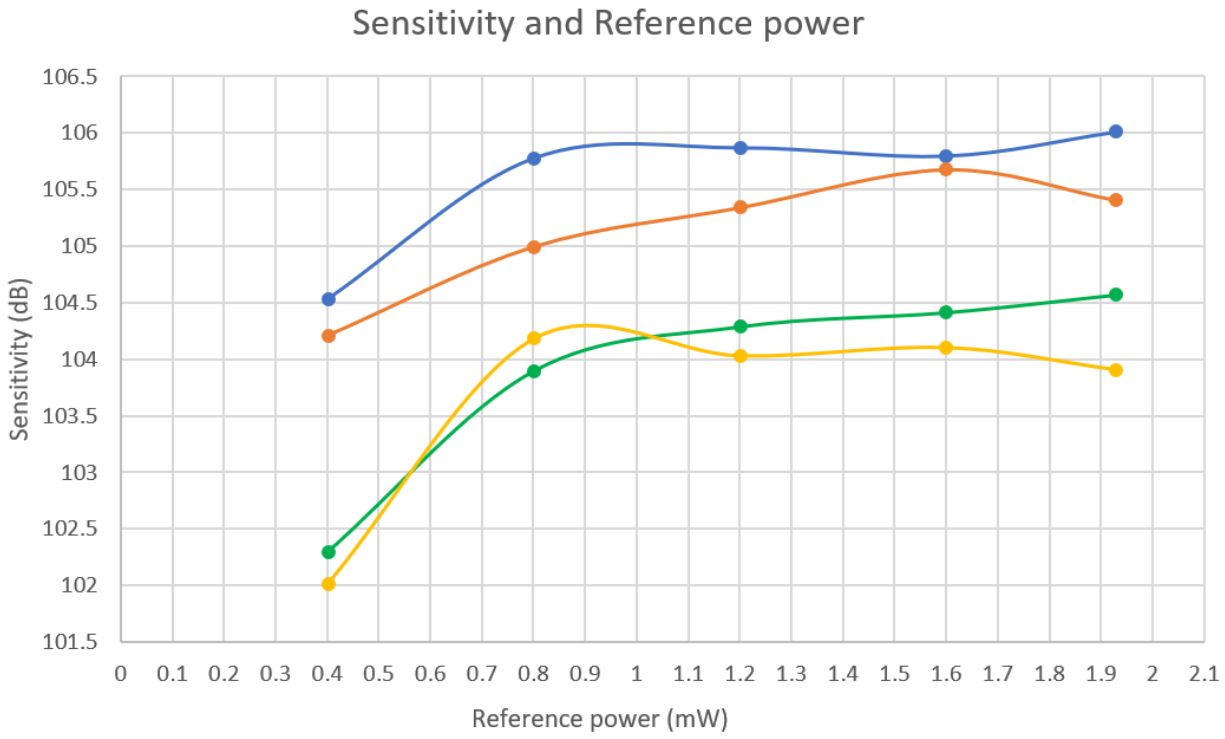

Figure 4.2: Sensitivity changing trend with reference power.

Signal-to-noise ratio (SNR) and sensitivity

After the optimization of reference power, the SNR and sensitivity was measured under the condition that 0.9-mW reference power. The intensity and background of the OCT signals of each channel, which corresponds

to the four entries of the Jones matrix, are shown in Fig. 4.3. With the measured data of signal intensity and background, the sensitivity of the four polarization channels were calculated to be 105, 105, 104, and 104 dB (Table 4.1).

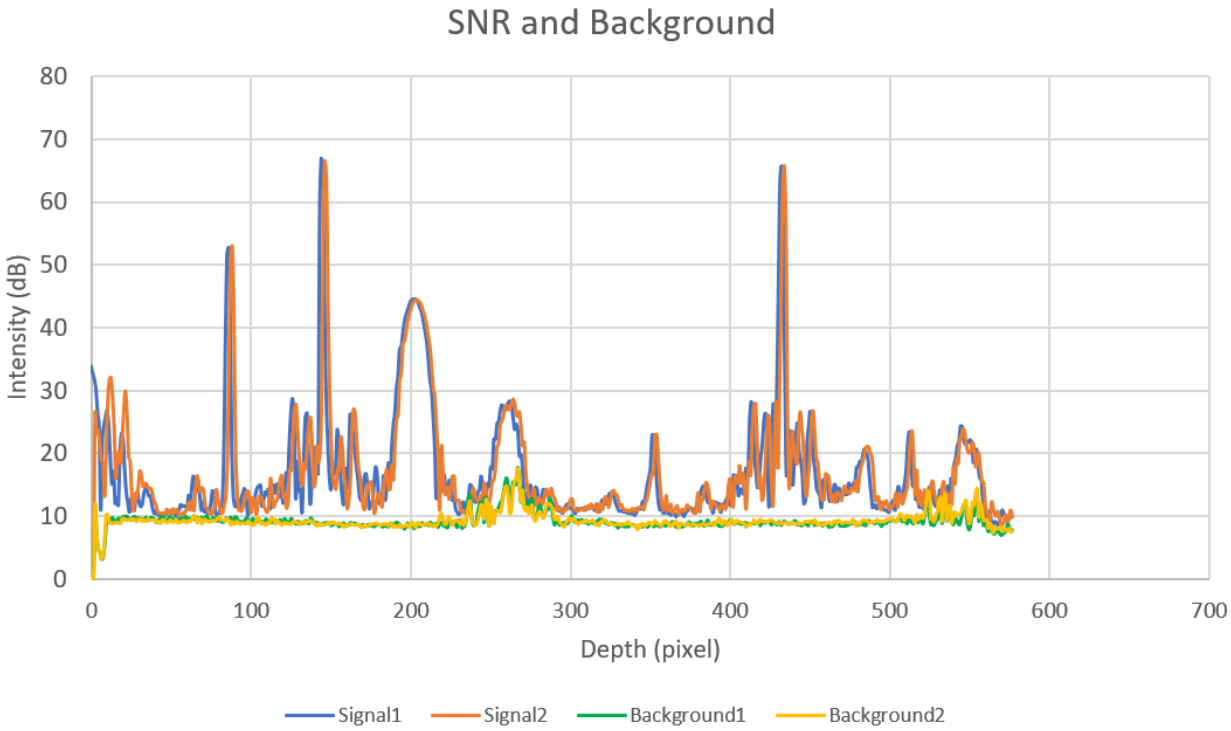

Figure 4.3: Intensity of OCT signals and background measured at 0.9-mW reference power.

Table 4.1 Sensitivity of each channel

Depth (z) / Channel No.	**Non-delay (144 pixel)**	**Delay (432 pixel)**
Ch. 1	105 dB	104 dB
Ch. 2	105 dB	104 dB

Imaging depth range and resolution

The depth imaging range is around 2.5 mm in air, which corresponds to 1.8 mm in tissue assuming a refractive index of 1.38. The axial resolution was measured to be 19.4 μm in air (14.1 μm in tissue), and the depth pixel separation was 8.7 μm in air (6.3 μm in tissue).

4.3 Multi-contrast imaging

Based on the theory described in Chapter 2, four contrasts, the scattering OCT, birefringence, DOPU, and OCT-A, were computed from the Jones matrix tomographies as follows.

4.3.1 Scattering OCT

A sensitivity-enhanced scattering OCT was obtained by a coherent composition of the four repeated Jones matrix tomographies as described in Section 3.8 of [27].

4.3.2 Birefringence tomography

The depth-resolved birefringence (local retardation) tomography was obtained by local Jones matrix analysis [24] combined with a maximum a posteriori birefringence estimator [25]. For easy observation, a pseudo-color birefringence tomography is created by combining the scattering intensity, birefringence, and reliability of the birefringence estimation. In this image, the birefringence is expressed by color hue if it is reliable, otherwise, the pixel is a shade of gray. The birefringence computation protocol is detailed in Section 4 of [22], and the pseudo-color image formation is described in Section 3.4 of [25].

4.3.3 DOPU tomography

The DOPU image was obtained using the DOPU computation algorithm with Makita's noise correction [41].

4.3.4 OCT-A

To compute OCT-A signal, we first corrected detection jitter of spectral signal as described in the next section (Section 4.3.5). The jitter-corrected signal was then processed by a complex correlation based OCT-A method, which is detailed in Section 4.2 of [42].

4.3.5 Jitter correction

OCT-A images were obtained using a complex correlation-based OCT-A method, in which the noise-corrected complex correlation among the four repeated frames is computed. The details of this method are described elsewhere [42], but we additionally applied a jitter correction as follows.

The jitter is a random ±1-sampling-point spectral shift generated by a small mutual fluctuation between the k-clock and the A-trigger. It results in strong artifacts in OCT-A because the jitter generates a large difference between the two temporal phase changes of the two incident polarization images as schematically depicted in Fig. 4.4. Here, the two incident polarizations are denoted as non-delayed and delayed channels.

As the first step of the numerical jitter correction, we computed

$$\rho_{h,v}^{d,nd}(t,\zeta;\tau) \equiv \Gamma_{h,v}^{d,nd}(t+\tau,\zeta)\Gamma_{h,v}^{*d,nd}(t,\zeta) \quad (1),$$

where ζ is the depth-pixel index, t is time, and τ is a time-lag between repeated scans. Further, $\Gamma_{h,v}^{d,nd}(t,\zeta)$ is a complex OCT A-line at time t and at indexed depth ζ. Subscripts h and v represent the two polarization detection channels (horizontal and vertical) and superscripts d and nd represent the two incident polarizations (delay and non-delay). Superscript $*$ denotes the complex conjugate.

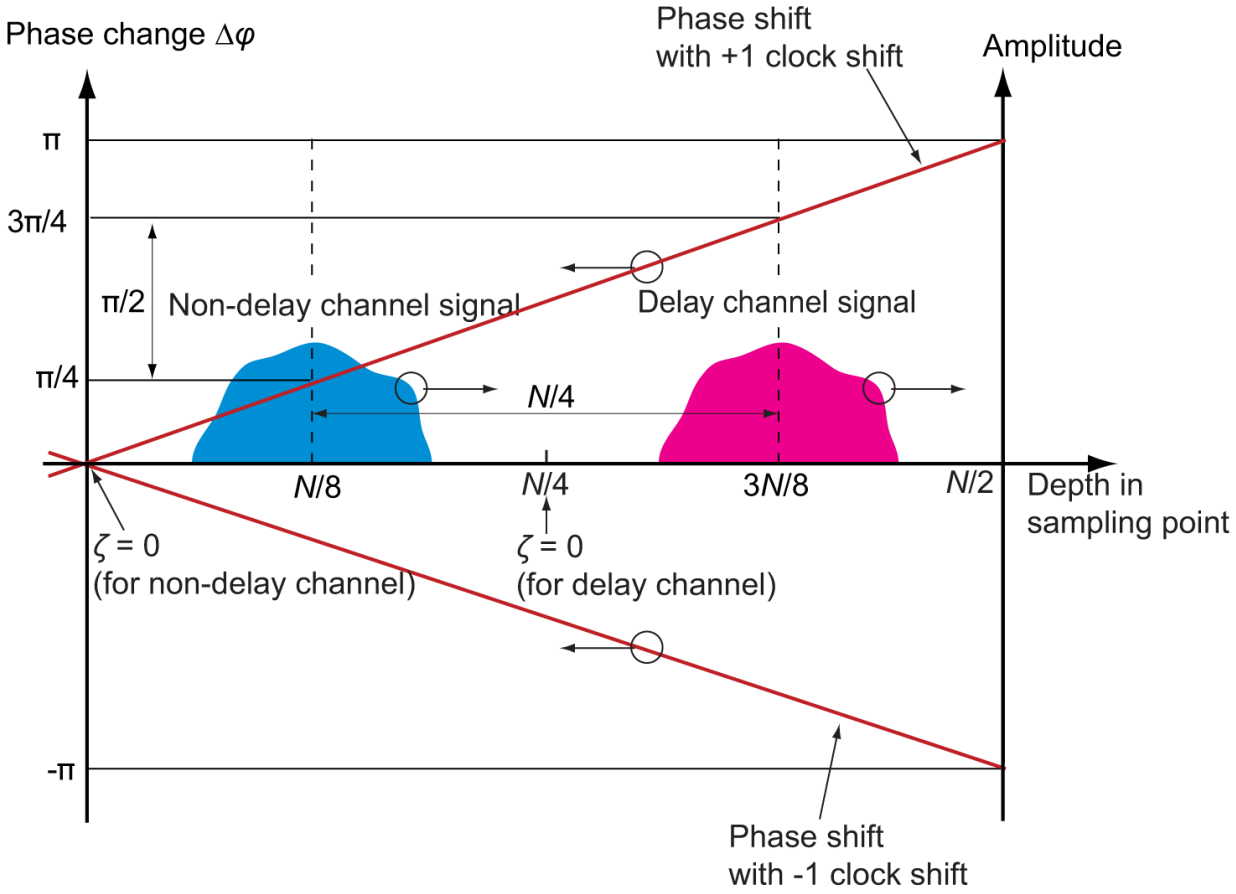

Figure 4.4: Schematic diagram of the phase shift caused by the random shift of the spectral sampling signal. N is sampling number and ζ is indexed depth position. The 0-th sampling point corresponds to the zero depth of the non-delayed polarization channel, while N/4-th sampling point corresponds to that of delayed polarization channel. The upper and lower red lines indicate a phase error caused by jitter of +1 and -1 clock shifts, respectively. For the +1-clock shift, the delayed signal is phase shifted by +π/2 in respect to the non-delayed channel. For the -1-clock shift, the corresponding phase shift is −π/2.

For each A-scan, we find five depth-points $(\zeta_1, \cdots, \zeta_5)$ with the highest time correlation using the method described in Section 3.1.1 of Ref. [42]. The temporal phase difference between $\Gamma_{h,v}^{d,nd}(t+\tau,\zeta)$ and $\Gamma_{h,v}^{d,nd}(t,\zeta)$ is then defined from the summation of $\rho_{h,v}^{d,nd}$ over the five points and the horizontal and vertical channels as

$$\Delta\phi^{d,nd}(t;\tau) \equiv \mathrm{Arg}\left[\sum_{i=1}^{5}\sum_{j=h,v}\rho_j^{d,nd}(t,\zeta_i;\tau)\right] \quad (2)$$

Here, note that the spectral sampling jitter among A-lines is the −1, 0 or +1 sampling point. In addition, the delay between non-delay and delay channels was configured to be quarter of the sampling points (N). Hence, the phase difference between the delay and non-delay signals, $\Delta\varphi(t;\tau) \equiv \Delta\phi^{d}(t;\tau) - \Delta\phi^{nd}(t;\tau)$Δϕ(t; τ), takes only three possible values as $-\pi/2$ for the −1-sampling-point shift, 0 for the 0-sampling-point shift, and $\pi/2$ for +1-sampling-point shift. Hence, the amount of jitter m (in sampling points) is estimated as

$$m(t;\tau) \equiv \begin{cases} -1 & \text{if } \Delta\varphi(t;\tau) \simeq -\dfrac{\pi}{2} \\ 0 & \text{if } \Delta\varphi(t;\tau) \simeq 0 \\ +1 & \text{if } \Delta\varphi(t;\tau) \simeq +\dfrac{\pi}{2} \end{cases} \quad (3).$$

Finally, the jitter corrected complex OCT signals are defined as

$$\hat{\Gamma}_{h,v}^{nd}(t+\tau,\zeta) \equiv \Gamma_{h,v}^{nd}(t+\tau,\zeta)e^{-i\frac{2\pi}{N}m\zeta} \quad (4)$$

and

$$\hat{\Gamma}_{h,v}^{d}(t+\tau,\zeta) \equiv \Gamma_{h,v}^{d}(t+\tau,\zeta)e^{-i\frac{2\pi}{N}m\zeta - i\frac{\pi}{2}m} \quad (5),$$

where the first terms in the exponential in Eqs. (4) and (5) are for phase slope correction, and the second term in Eq. (5) is to correct a phase offset caused by the jitter. The OCT-A was finally computed by means of a complex correlation based OCT-A method [42] from these jitter-corrected OCT signals.

Figure 4.5 demonstrates the performance of the jitter correction. Without jitter correction, vertical low correlation (white) line artifacts are evident in the cross-sectional image [Fig. 4.5(a)] and several low correlation (white) salt-and-pepper artifacts appeared in the *en face* image [Fig. 4.5(b)]. These artifacts were removed by the jitter correction as shown in Figs. 4.5(c) and 4.5(d). The residual horizontal white artifacts in Fig. 4.5(d) are due to sample motion.

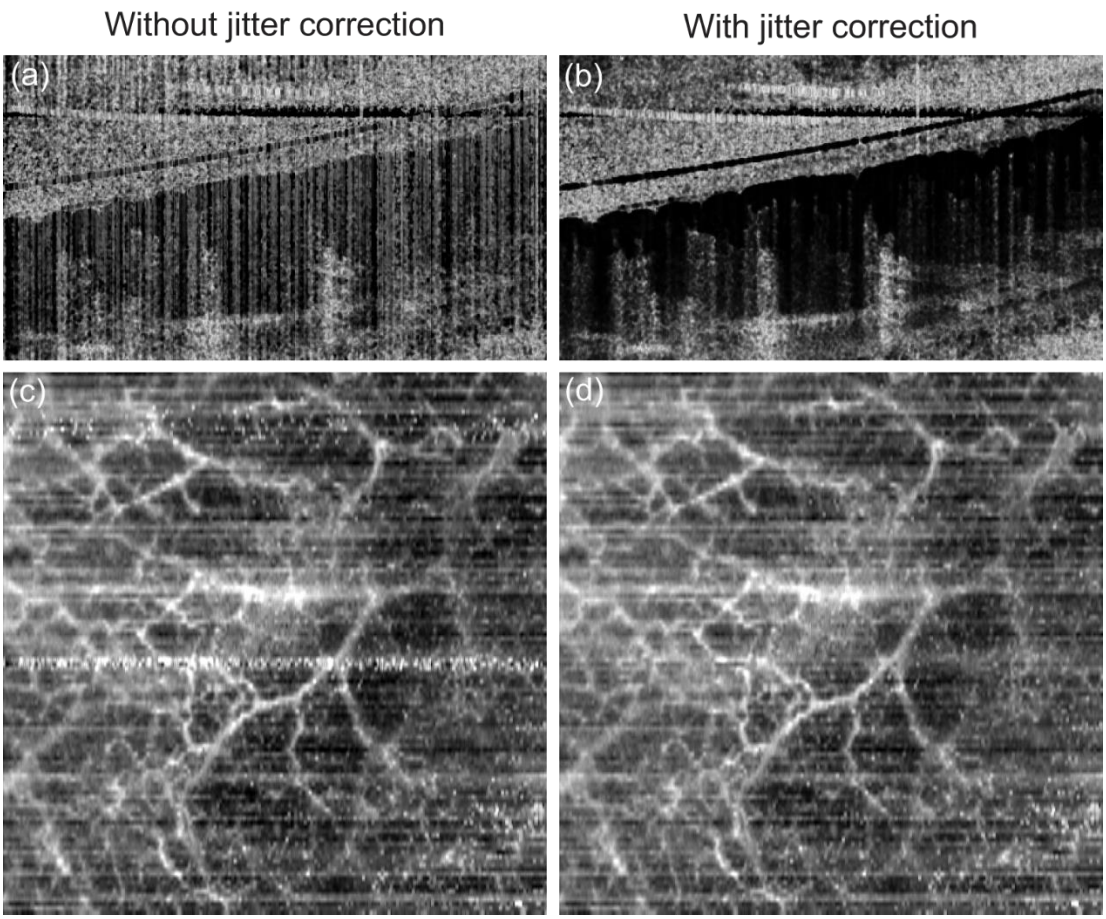

Figure 4.5: Examples of OCT-A images of nail bed skin without (left) and with (right) motion correction. (a) and (b) are cross-sections, (c) and (d) are *en face* images.

4.4 Experiment

To assess the utility of the JM-OCT for dermatological investigation, five healthy volunteers (4 males and 1 female) were measured. All the subjects are East Asian, and their ages ranged from 30 to 40 years old. For each subject, skin at three locations including finger pad, inner-forearm, and outer-forearm were measured. Since the JM-OCT findings are consistent among the subjects, a representative case is discussed for each location in Section 4.5.

The scan is a raster scan with 512 A-lines × 128 B-scans × 4 repeats of the B-scan. The imaging range is 6.0 × 6.0 mm in lateral and 1.8 mm in depth. For this configuration, the voxel size is 11.7 μm × 46.9 μm (lateral) × 6.3 μm (depth, in tissue). The acquisition time for a volume is 6.7 s. All protocols were approved by the Institutional Review Board of the University of Tsukuba. Written informed consent was obtained prior to measurement.

4.5 Results

4.5.1 Multi-contrast imaging of the outer forearm

Examples of multi-contrast imaging of the skin of the outer forearm are shown in Fig. 4.6. The cross-sectional images and *en face* images of each contrast were extracted from volumetric OCT data. The straight sloped lines above the surface of the skin that can be observed in the cross-sectional images [Figs 4.6(a)-(d)] are from the glass slip. The space between the glass slip and the skin surface was filled with ultrasound gel for refractive index matching. Small hyper-scattering spots in the gel [Fig. 4.6(a)] are the cross-sections of hairs.

Figure 4.6(a) is a cross-sectional scattering OCT. The epidermis appears as a relatively low scattering region just beneath the skin surface. The higher scattering region beneath the epidermis is dermis. Figure 4.6(b) is a complex-correlation OCT-A. The white (low time correlation) spots with tailed artifacts are blood vessels in the dermis. Figure 4.6(c) is the cross-sectional DOPU image. The epidermis and superficial part of the dermis (papillary dermis) appeared with high uniformity (red), while the uniformity decreases (yellow to green) in the deeper dermis. Figure 4.6(d) shows the birefringence property of the skin. The epidermis regions have low birefringence (blue), while the dermis regions have relatively high birefringence (green). It should be noted that regions with very low OCT signal, such as air and deep tissue regions, show not very low but only moderately low DOPU values. It is because the DOPU we used is not the original DOPU [40] but M-DOPU, which is DOPU with signal-to-noise ratio correction [41].

The *en face* slices [Figs. 4.6(e)-(h)] were extracted at the dermal level; 0.58-mm (in tissue) below the skin surface. The depth position of the slices is indicated by dashed lines in Figs. 4.6(a)-(d). Note that the texture pattern that appears in the scattering OCT [Fig. 4.6(e)] is not correlated with that in the DOPU [Fig. 4.6(g)]. Future histological correlative study is necessary for understanding these structures. The *en face* OCT-A [Fig. 4.6(f)] shows large plexus dermal vessels.

4.5.2 Multi-contrast imaging of finger pad

Figure 4.7 shows multi-contrast tomographies of the finger pad. In the backscattering OCT intensity image [Fig. 4.7(a)], the stratum corneum appears as the topmost thick moderately scattering layer. The helical structures in the stratum corneum are sweat glands. In Fig. 4.7(c), the sweat glands appear with high polarization uniformity (red). The superficial part of the stratum corneum shows high polarization uniformity (red), while the lower part exhibits low polarization uniformity (yellow to green). In Fig. 4.7(b), the superficial stratum corneum exhibits low birefringence (blue to light blue). Since the superficial stratum corneum with distinctive DOPU and birefringence appearance is significantly thicker than the optical resolution and DOPU kernel, this superficial layer would not be an artifact. It would highlight inhomogeneity of stratum corneum as

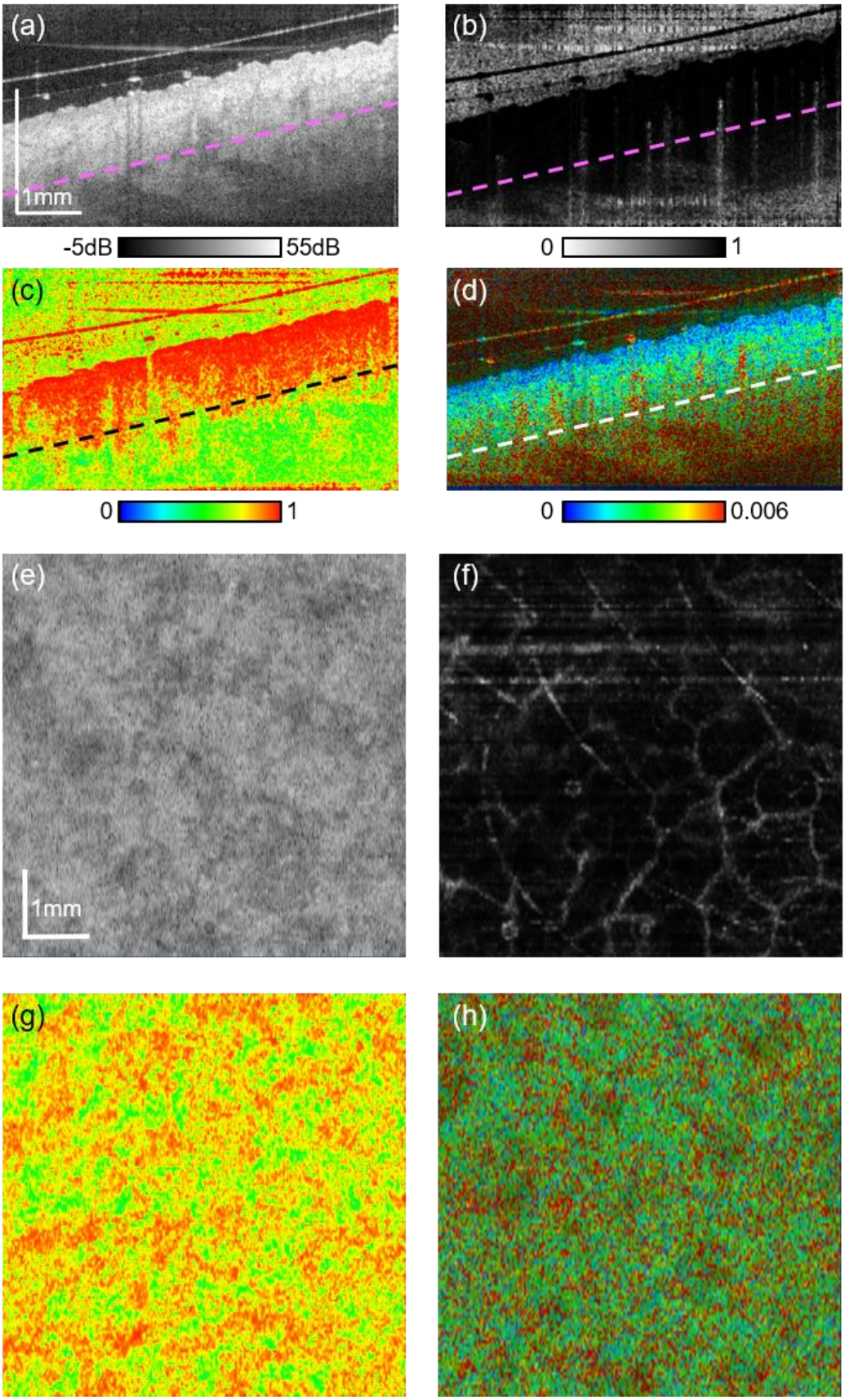

Figure 4.6: Multi-contrast images of outer-forearm skin. Cross-sections of (a) scattering OCT, (b) OCT-A, (c) DOPU, and (d) birefringence. *En face* slices of (e) scattering OCT, (f) OCT-A, (g) DOPU, and (h) birefringence. The depth position of the *en face* slices are indicated by dashed lines in (a)-(d).

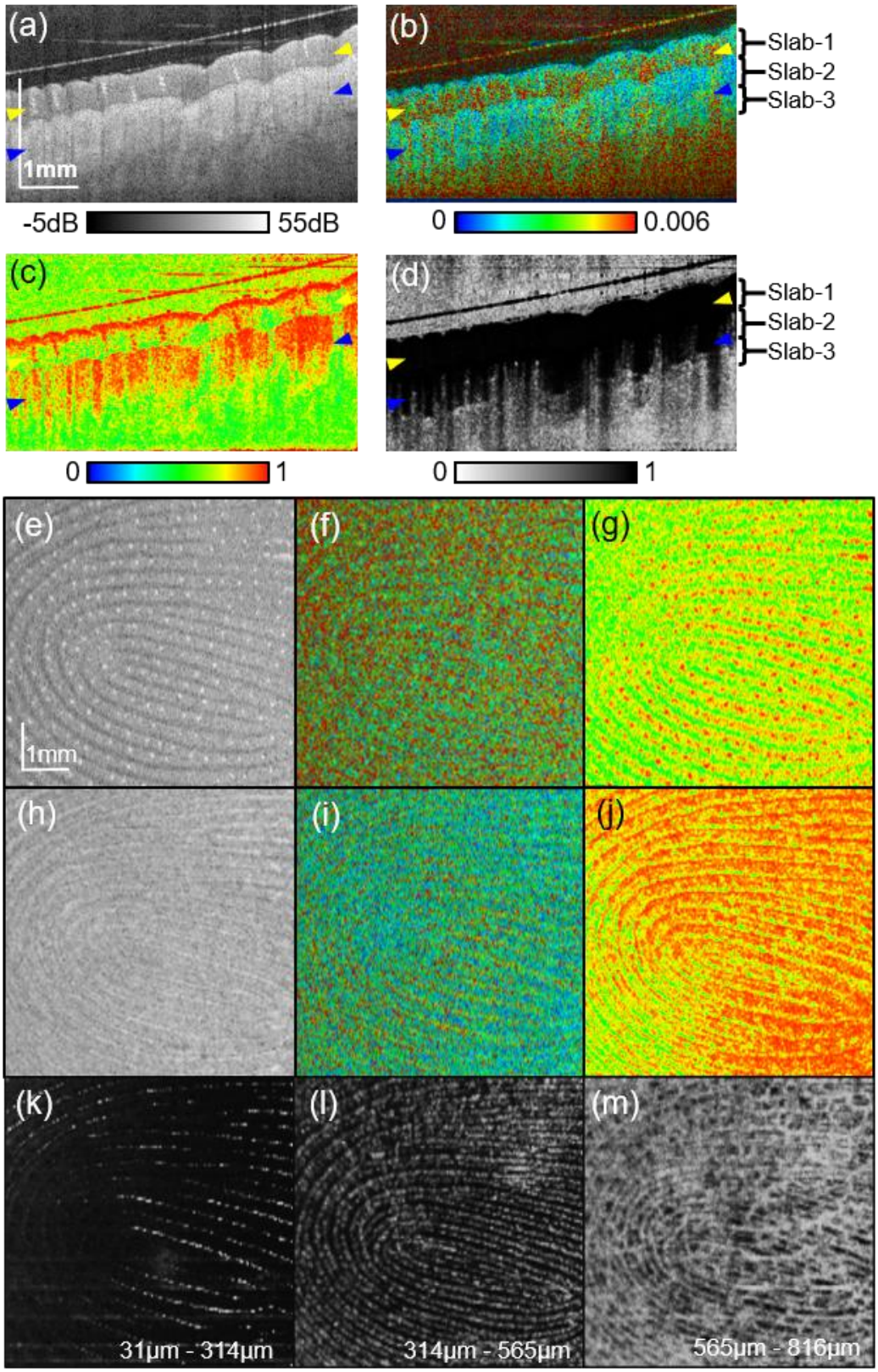

Figure 4.7: Multi-contrast images of finger pad. Cross-sectional (a) intensity, (b) birefringence tomography, (c) DOPU tomography, and (d) OCT-A. (e)-(g) are *en face* slices at the depth indicated by yellow arrowheads in the cross-sectional images. (h)-(j) are *en face* slices at the depth of blue arrowheads. (e) and (h): scattering intensity, (f) and (i): birefringence, (g) and (j): DOPU. (k)-(m) are slab projections of OCT-A. The depth positions of the slabs are indicated in (b) and (d).

it can be seen in histology (i.e., Chapter 9 of [47]). The tissue beneath the stratum corneum is deeper part of epidermis and then dermis, although these layers are not clearly distinguishable in a conventional OCT contrast image [Fig. 4.7(a)]. This region has weak to moderate birefringence (light blue to green) [Fig. 4.7(b)] and low polarization uniformity [Fig. 4.7(c)]. In the OCT-A cross section [Fig. 4.7(d)], some white spots appear in the dermal region. Because the spots appeared with tailed artifacts, they are blood vessels. There is a diffuse white appearance in the deep (reticular) dermal region. It would indicate flows in capillaries.

The high birefringence appearance at the glass surface [Fig. 4.7(b)] would be an artifact caused by the birefringence computation method. In our method, the birefringence is computed by using two pixels separated for 6 pixels in depth. On the other hand, the glass surface signal has a depth width of around 2.2 pixels, which is defined by the depth resolution. Since the signal width is significantly narrower than the pixel separation for the birefringence computation, the birefringence obtained at the glass surface cannot be accurate.

Bonesi *et al*. also investigated DOPU distribution of human fingertip (Fig. 6 of [36]. Since Bonesi *et al*. uses conventional DOPU [40] and we have used DOPU with Makita's noise correction [41], the absolute DOPU values are different. However, the overall tendency of DOPU values are consistent. For example, the superficial part of stratum corneum has very high DOPU and the middle layer of stratum corneum has low DOPU. In both images, the lower epidermal and dermal regions show vertical stripe patterns of DOPU as the ridge regions show higher DOPU than groove regions. Pircher *et al*. investigated the phase retardation and optic axis orientation appearances of finger pad [48]. Although this study did not use DOPU, the overall polarization-uniformity property of the finger pad is consistent with the present study. Namely, the phase retardation and the axis orientation at the middle part of stratum corneum showed random pattern as in Figs. 2 and 4 of [48], while our result showed low DOPU at this region. Pircher *et al*. also performed quantitative analysis of cumulative phase retardation at the stratum corneum. It was recently found that the cumulative phase retardation is not consistent with local phase retardation (birefringence) if the axis orientation is not constant (see Section 6.1 of [22]). Hence, it is hard to compare their phase retardation values and our birefringence values. In order to link the findings obtained by phase-retardation-based and birefringence-based PS-OCTs, it would be important to investigate the relationship among cumulative phase retardation, birefringence, and histology.

The *en face* images in Figs. 4.7(e)-(g) are at the 0.20 mm below the surface (stratum corneum, indicated by a pair of yellow arrowheads in the cross-sectional images) and Figs. 4.7(h)–(j) are 0.57 mm below the surface (around the superficial dermis, blue arrow heads). In the scattering OCT at the stratum corneum [Fig. 4.7(e)], the fingerprint appears with relatively bright bands (ridges) and dark bands (grooves). The bright spots aligned along the ridges are sweat ducts. In the DOPU image [Fig. 4.7(g)], the ridges appear with moderate uniformity (yellow) and the grooves appear with low uniformity (green). The sweat ducts appear as high-uniformity (red) spots in the ridges. In the scattering image of the deeper region [Fig. 4.7(h)], the bright bands (ridges) in the superficial layer appears as dark bands and the bright bands (grooves) appear as dark. This structure is known as the internal fingerprint [10]. The internal fingerprint is visible also in the DOPU image

[Fig. 4.7(j)]. Unlike the superficial layer [Fig. 4.7(g)], the ridges appeared with high uniformity (red) and the grooves appear with low uniformity (yellow to green).

Figures 4.7(k)-(m) show the slab-average projection of OCT-A at the depths of 31 to 314 μm (stratum corneum, slab-1), 314 to 565 μm (deep epidermis to papillary dermis, slab-2), and 565 to 816 μm (deep dermis, slab-3), respectively. The depth locations of the slabs are indicated in Figs. 4.7(b) and 4.7(d). In the slab-2 [Fig. 4.7(l)], the vasculature forms the fingerprint pattern. This vasculature would be papillary capillaries, which are known to be aligned along the fingerprint ridges [49,50]. Because slab-1 includes the deep epidermis and papillary dermis to some extent, some papillary capillaries are visible as shown in Fig. 4.7(k). The deepest slab (slab-3) [Fig. 4.7(m)] shows not only the fingerprint pattern but also the dermal vessel network.

4.5.3 Multi-contrast imaging of inner forearm

The inner forearm was measured as an example of thin skin. Figure 4.8 shows multi-contrast cross-sections of the forearm. In the scattering image [Fig. 4.8(a)], the stratum corneum is appeared as the topmost thin hyper-scattering layer, which is significantly thinner than that of finger pad. The epidermis appears as relatively low scattering layer beneath the stratum corneum. It appears with high polarization uniformity (red) as shown in Fig. 4.8(c), while the dermis shows both low and high uniformity regions. The birefringence image [Fig. 4.8(d)] visualizes low birefringence (blue) in the epidermis, and moderately high birefringence (green) in the dermis. OCT-A [Fig. 4.8(b)] shows blood flow in the dermis. It should be noted that the very small high birefringence

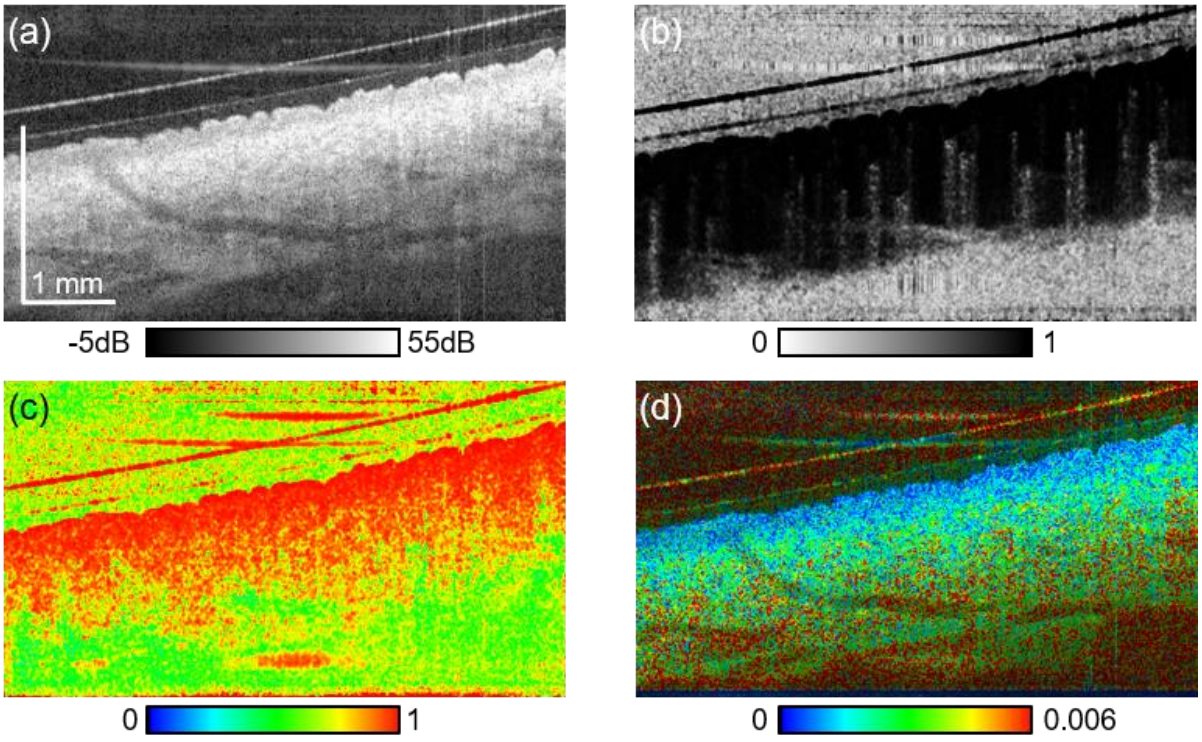

Figure 4.8: Cross-sectional multi-contrast images of inner-forearm skin. (a) Scattering OCT, (b) OCT-A, (c) DOPU, and (d) birefringence tomography.

spots in Fig. 4.8(d) would be artifacts caused by birefringence measurement and/or estimation algorithm. One possible cause is that the current birefringence estimator [25] does not take the speckle effect into account. Although it was not evident as in Fig. 4.8(c), the same artifacts can also be seen in the birefringence images in Figs. 4.6 and 4.7.

We split the JM-OCT volume into three slabs based on its birefringence appearance as shown in Fig. 4.9, and OCT-A average projections were created for each slab [Figs. 4.9(b)–(d)]. The slabs show the low birefringence region (superficial slab), a mixture of low and high birefringence region (intermediate slab), and high birefringence region (deepest slab). The depths of each slab were 31 to 75 µm (superficial), 75 to 282 µm (intermediate), and 282 to 659 µm (deepest), respectively from the skin surface. The first superficial slab (low birefringence) had a thickness of around 75 µm, which is close to the epidermal thickness of the inner-forearm [51]. In the *en face* OCT-A of the first slab [Figs. 4.9(b)], vertical capillaries appear as white spots. The intermediate slab mainly consists of papillary dermis and its OCT-A shows fine vascular plexus [Figs. 4.9(c)]. The deepest slab also shows vascular plexus [Figs. 4.9(d)], but the vessels are thicker, and the plexus is more macroscopic.

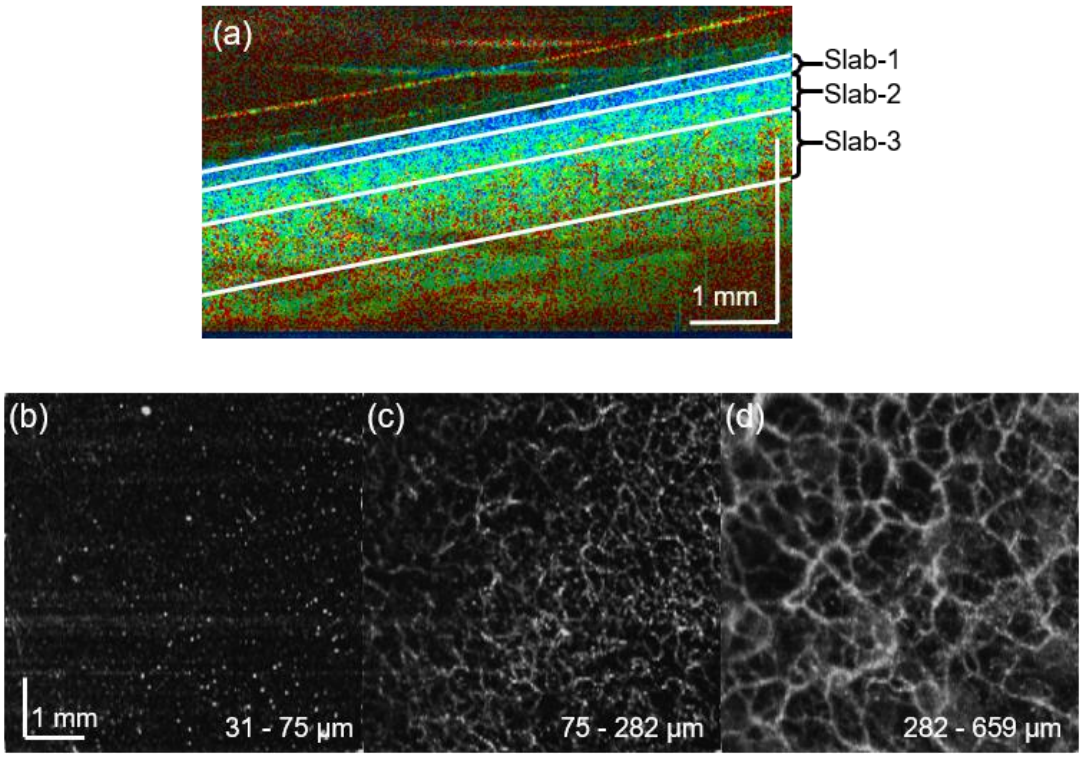

Figure 4.9: (b)-(d) Slab projections of OCT-A of the inner-forearm skin tissue. The depth positions of the slabs are indicated in a cross-sectional birefringence tomography (a).

4.6 Discussion and conclusion

Almost all previous PS-OCT studies used phase retardation imaging to investigate collagen-related skin alteration and optical properties, such as age-related alteration and photo-aging [19], and some mechanical skin properties [52]. Because birefringence imaging enables a more accurate and quantitative evaluation of tissue property than the phase retardation images [22], it will enable further investigation of skin properties, alteration, and pathologies.

There are still some limitations in the current JM-OCT. First, the imaging range is not always large enough. The depth measurement range of the current system is 2.5 mm in air (1.8 mm in tissue). This is sufficient for most tissue types, but it is not enough for tissue with a markedly uneven surface. In the current measurement protocol, we use a glass slip primarily to avoid skin surface reflection, but it also flattened the skin. Although this moderates the above limitation, it could potentially occlude the blood circulation, and hence, disturbs the OCT-A measurement. Hence, a JM-OCT with longer depth range is preferable. The measurement range is primarily limited by the k-clock frequency, and also by the coherence length of the wavelength sweeping light source. The former limitation can be resolved by using a high-frequency k-clock generator [28], and the latter can be resolved by using light sources with a more longer coherence length, such as akinetic light source [53] or VCSEL light source [54].

Another limitation is the relatively low lateral resolution in the out-of-focus region. This limitation will become more severe if we extend the depth measurement range as discussed above. Some possible solutions are numerical refocusing [55–58] or an extended focus technique [59–61].

The interpretation of birefringence values at low DOPU regions is an open issue. In this particular study, the birefringence is estimated by using a spatial kernel. So, the polarization property of the tissue is not uniform within the kernel and the estimated birefringence cannot be accurate. In other words, the estimated birefringence is not reliable if DOPU is low. This imitation should be considered for the interpretation of JM-OCT images.

4.7 Summary

In this chapter, a multifunctional JM-OCT was developed and utilized for dermatological imaging. In the detailed discussion, we investigated and demonstrated to image different dermatological tissues *in vivo*, such as outer-forearm, finger pad, inner-forearm with using the established JM-OCT, in which four contrasts, including depth-resolved birefringence, DOPU, and OCT-A, were simultaneously computed from the Jones matrix tomography. Unlike most of common PS-OCT, using phase retardation imaging to investigate collagen-related skin alteration and optical properties, birefringence imaging in the multifunctional JM-OCT system enables a more accurate and quantitative evaluation of tissue property, which allows one to further investigation of skin properties, alteration, and pathologies. As shown in this research, particularly, making use of scattering, polarization, and flow contrasts, internal skin structures that were not visible by standard

OCT could be successfully visualized. Despite further investigation is still necessary to tackle a few limitations (e.g. relatively low lateral resolution in the out-of-focus region, not large enough imaging range, etc.), the developed multifunctional JM-OCT in this study has exhibited its remarkable merits of non-invasiveness and three-dimensional measurement capability. This study provides a first step toward developing dermatological imaging based on the multifunctional JM-OCT as well as the feasibility for future clinic utility.

References

1. D. Huang, E. A. Swanson, C. P. Lin, J. S. Schuman, W. G. Stinson, W. Chang, M. R. Hee, T. Flotte, K. Gregory, C. A. Puliafito, and J. G. Fujimoto, "Optical Coherence Tomography," Science **254**(5035), 1178–1181 (1991).
2. J. A. Izatt, M. R. Hee, E. A. Swanson, C. P. Lin, D. Huang, J. S. Schuman, C. A. Puliafito, and J. G. Fujimoto, "Micrometer-Scale Resolution Imaging of the Anterior Eye In Vivo With Optical Coherence Tomography," Arch Ophthalmol **112**(12), 1584–1589 (1994).
3. C. A. Puliafito, M. R. Hee, C. P. Lin, E. Reichel, J. S. Schuman, J. S. Duker, J. A. Izatt, E. A. Swanson, and J. G. Fujimoto, "Imaging of Macular Diseases with Optical Coherence Tomography," Ophthalmology **102**(2), 217–229 (1995).
4. I.-K. Jang, G. J. Tearney, B. MacNeill, M. Takano, F. Moselewski, N. Iftima, M. Shishkov, S. Houser, H. T. Aretz, E. F. Halpern, and B. E. Bouma, "In Vivo Characterization of Coronary Atherosclerotic Plaque by Use of Optical Coherence Tomography," Circulation **111**(12), 1551–1555 (2005).
5. G. J. Tearney, M. E. Brezinski, J. F. Southern, B. E. Bouma, S. A. Boppart, and J. G. Fujimoto, "Optical biopsy in human gastrointestinal tissue using optical coherence tomography," Am. J. Gastroenterol. **92**(10), 1800–1804 (1997).
6. B. W. Colston, U. S. Sathyam, L. B. DaSilva, M. J. Everett, P. Stroeve, and L. L. Otis, "Dental OCT," Opt. Express, OE **3**(6), 230–238 (1998).
7. J. Welzel, E. Lankenau, R. Birngruber, and R. Engelhardt, "Optical coherence tomography of the human skin," Journal of the American Academy of Dermatology **37**(6), 958–963 (1997).
8. J. Welzel, "Optical coherence tomography in dermatology: a review," Skin Research and Technology **7**(1), 1–9 (2001).
9. T. Gambichler, G. Moussa, M. Sand, D. Sand, P. Altmeyer, and K. Hoffmann, "Applications of optical coherence tomography in dermatology," Journal of Dermatological Science **40**(2), 85–94 (2005).
10. E. Auksorius and A. C. Boccara, "Fingerprint imaging from the inside of a finger with full-field optical coherence tomography," Biomed. Opt. Express, BOE **6**(11), 4465–4471 (2015).
11. E. D. Harris and A. Sjoerdsma, "Effect of penicillamine on human collagen and its possible application to treatment of scleroderma," Lancet **288**(7471), 996–999 (1966).
12. G. P. Rodnan, E. Lipinski, and J. Luksick, "Skin thickness and collagen content in progressive systemic sclerosis and localized scleroderma," Arthritis & Rheumatism **22**(2), 130–140 (1979).
13. G. Rayman, A. Hassan, and J. E. Tooke, "Blood flow in the skin of the foot related to posture in diabetes mellitus.," Br Med J (Clin Res Ed) **292**(6513), 87–90 (1986).

14. G. Belcaro, S. Vasdekis, A. Rulo, and A. N. Nicolaides, "Evaluation of Skin Blood Flow and Venoarteriolar Response in Patients with Diabetes and Peripheral Vascular Disease by Laser Doppler Flowmetry," Angiology **40**(11), 953–957 (1989).

15. J. A. Izatt, M. D. Kulkarni, S. Yazdanfar, J. K. Barton, and A. J. Welch, "In vivo bidirectional color Doppler flow imaging of picoliter blood volumes using optical coherence tomography," Opt. Lett., OL **22**(18), 1439–1441 (1997).

16. J. F. de Boer, S. M. Srinivas, A. Malekafzali, Z. Chen, and J. S. Nelson, "Imaging thermally damaged tissue by polarization sensitive optical coherence tomography," Opt. Express, OE **3**(6), 212–218 (1998).

17. Y. Yasuno, S. Makita, Y. Sutoh, M. Itoh, and T. Yatagai, "Birefringence imaging of human skin by polarization-sensitive spectral interferometric optical coherence tomography," Opt. Lett., OL **27**(20), 1803–1805 (2002).

18. M. C. Pierce, J. Strasswimmer, B. Hyle Park, B. Cense, and J. F. de Boer, "Advances in Optical Coherence Tomography Imaging for Dermatology," Journal of Investigative Dermatology **123**(3), 458–463 (2004).

19. S. Sakai, M. Yamanari, A. Miyazawa, M. Matsumoto, N. Nakagawa, T. Sugawara, K. Kawabata, T. Yatagai, and Y. Yasuno, "In vivo Three-Dimensional Birefringence Analysis Shows Collagen Differences between Young and Old Photo-Aged Human Skin," Journal of Investigative Dermatology **128**(7), 1641–1647 (2008).

20. W. J. Choi, R. Reif, S. Yousefi, and R. K. Wang, "Improved microcirculation imaging of human skin in vivo using optical microangiography with a correlation mapping mask," J. Biomed. Opt **19**(3), 036010–036010 (2014).

21. B. H. Park, M. C. Pierce, B. Cense, S.-H. Yun, M. Mujat, G. J. Tearney, B. E. Bouma, and J. F. de Boer, "Real-time fiber-based multi-functional spectral-domain optical coherence tomography at 1.3 μm," Opt. Express, OE **13**(11), 3931–3944 (2005).

22. S. Sugiyama, Y.-J. Hong, D. Kasaragod, S. Makita, S. Uematsu, Y. Ikuno, M. Miura, and Y. Yasuno, "Birefringence imaging of posterior eye by multi-functional Jones matrix optical coherence tomography," Biomed. Opt. Express, BOE **6**(12), 4951–4974 (2015).

23. S. Guo, J. Zhang, L. Wang, J. S. Nelson, and Z. Chen, "Depth-resolved birefringence and differential optical axis orientation measurements with fiber-based polarization-sensitive optical coherence tomography," Opt. Lett., OL **29**(17), 2025–2027 (2004).

24. S. Makita, M. Yamanari, and Y. Yasuno, "Generalized Jones matrix optical coherence tomography: performance and local birefringence imaging," Opt. Express, OE **18**(2), 854–876 (2010).

25. D. Kasaragod, S. Makita, S. Fukuda, S. Beheregaray, T. Oshika, and Y. Yasuno, "Bayesian maximum likelihood estimator of phase retardation for quantitative polarization-sensitive optical coherence tomography," Opt. Express, OE **22**(13), 16472–16492 (2014).

26. Y. Lim, M. Yamanari, S. Fukuda, Y. Kaji, T. Kiuchi, M. Miura, T. Oshika, and Y. Yasuno, "Birefringence measurement of cornea and anterior segment by office-based polarization-sensitive optical coherence tomography," Biomed. Opt. Express, BOE **2**(8), 2392–2402 (2011).

27. M. J. Ju, Y.-J. Hong, S. Makita, Y. Lim, K. Kurokawa, L. Duan, M. Miura, S. Tang, and Y. Yasuno, "Advanced multi-contrast Jones matrix optical coherence tomography for Doppler and polarization sensitive imaging," Opt. Express, OE **21**(16), 19412–19436 (2013).

28. M. Yamanari, S. Tsuda, T. Kokubun, Y. Shiga, K. Omodaka, Y. Yokoyama, N. Himori, M. Ryu, S. Kunimatsu-Sanuki, H. Takahashi, K. Maruyama, H. Kunikata, and T. Nakazawa, "Fiber-based polarization-sensitive OCT for birefringence imaging of the anterior eye segment," Biomed. Opt. Express, BOE **6**(2), 369–389 (2015).

29. Z. Wang, H.-C. Lee, O. O. Ahsen, B. Lee, W. Choi, B. Potsaid, J. Liu, V. Jayaraman, A. Cable, M. F. Kraus, K. Liang, J. Hornegger, and J. G. Fujimoto, "Depth-encoded all-fiber swept source polarization sensitive OCT," Biomed. Opt. Express, BOE **5**(9), 2931–2949 (2014).

30. M. Yamanari, S. Tsuda, T. Kokubun, Y. Shiga, K. Omodaka, N. Aizawa, Y. Yokoyama, N. Himori, S. Kunimatsu-Sanuki, K. Maruyama, H. Kunikata, and T. Nakazawa, "Estimation of Jones matrix, birefringence and entropy using Cloude-Pottier decomposition in polarization-sensitive optical coherence tomography," Biomed. Opt. Express, BOE **7**(9), 3551–3573 (2016).

31. M. Villiger and B. E. Bouma, "Practical decomposition for physically admissible differential Mueller matrices," Opt. Lett., OL **39**(7), 1779–1782 (2014).

32. M. Villiger, D. Lorenser, R. A. McLaughlin, B. C. Quirk, R. W. Kirk, B. E. Bouma, and D. D. Sampson, "Deep tissue volume imaging of birefringence through fibre-optic needle probes for the delineation of breast tumour," Scientific Reports **6**, 28771 (2016).

33. L. Duan, S. Makita, M. Yamanari, Y. Lim, and Y. Yasuno, "Monte-Carlo-based phase retardation estimator for polarization sensitive optical coherence tomography," Opt. Express, OE **19**(17), 16330–16345 (2011).

34. D. Kasaragod, S. Sugiyama, Y. Ikuno, D. Alonso-Caneiro, M. Yamanari, S. Fukuda, T. Oshika, Y.-J. Hong, E. Li, S. Makita, M. Miura, and Y. Yasuno, "Accurate and quantitative polarization-sensitive OCT by unbiased birefringence estimator with noise-stochastic correction," in *Optical Coherence Tomography and Coherence Domain Optical Methods in Biomedicine XX* (International Society for Optics and Photonics, 2016), **9697**, p. 96971I.

35. D. Kasaragod, S. Makita, Y.-J. Hong, and Y. Yasuno, "Noise stochastic corrected maximum a posteriori estimator for birefringence imaging using polarization-sensitive optical coherence tomography," Biomed. Opt. Express, BOE **8**(2), 653–669 (2017).

36. M. Bonesi, H. Sattmann, T. Torzicky, S. Zotter, B. Baumann, M. Pircher, E. Götzinger, C. Eigenwillig, W. Wieser, R. Huber, and C. K. Hitzenberger, "High-speed polarization sensitive optical coherence tomography scan engine based on Fourier domain mode locked laser," Biomed. Opt. Express, BOE **3**(11), 2987–3000 (2012).

37. W. C. Y. Lo, M. Villiger, A. Golberg, G. F. Broelsch, S. Khan, C. G. Lian, W. G. Austen, M. Yarmush, and B. E. Bouma, "Longitudinal, 3D Imaging of Collagen Remodeling in Murine Hypertrophic Scars In Vivo Using Polarization-Sensitive Optical Frequency Domain Imaging," Journal of Investigative Dermatology **136**(1), 84–92 (2016).

38. G. Liu, W. Jia, V. Sun, B. Choi, and Z. Chen, "High-resolution imaging of microvasculature in human skin in-vivo with optical coherence tomography," Opt. Express, OE **20**(7), 7694–7705 (2012).

39. W. J. Choi and R. K. Wang, "Volumetric cutaneous microangiography of human skin in vivo by VCSEL swept-source optical coherence tomography," Quantum Electron. **44**(8), 740 (2014).

40. E. Götzinger, M. Pircher, W. Geitzenauer, C. Ahlers, B. Baumann, S. Michels, U. Schmidt-Erfurth, and C. K. Hitzenberger, "Retinal pigment epithelium segmentation by polarization sensitive optical coherence tomography," Opt. Express, OE **16**(21), 16410–16422 (2008).

41. S. Makita, Y.-J. Hong, M. Miura, and Y. Yasuno, "Degree of polarization uniformity with high noise immunity using polarization-sensitive optical coherence tomography," Opt. Lett., OL **39**(24), 6783–6786 (2014).

42. S. Makita, K. Kurokawa, Y.-J. Hong, M. Miura, and Y. Yasuno, "Noise-immune complex correlation for optical coherence angiography based on standard and Jones matrix optical coherence tomography," Biomed. Opt. Express, BOE **7**(4), 1525–1548 (2016).

43. B. Baumann, W. Choi, B. Potsaid, D. Huang, J. S. Duker, and J. G. Fujimoto, "Swept source / Fourier domain polarization sensitive optical coherence tomography with a passive polarization delay unit," Opt. Express, OE **20**(9), 10229–10241 (2012).

44. Y. Lim, Y.-J. Hong, L. Duan, M. Yamanari, and Y. Yasuno, "Passive component based multifunctional Jones matrix swept source optical coherence tomography for Doppler and polarization imaging," Opt. Lett., OL **37**(11), 1958–1960 (2012).

45. S. Makita and Y. Yasuno, "In vivo photothermal optical coherence tomography for non-invasive imaging of endogenous absorption agents," Biomed. Opt. Express, BOE **6**(5), 1707–1725 (2015).

46. S. Moon, S.-W. Lee, and Z. Chen, "Reference spectrum extraction and fixed-pattern noise removal in optical coherence tomography," Opt. Express, OE **18**(24), 24395–24404 (2010).

47. B. Young, P. Woodford, and G. O'Dowd, *Wheater's Functional Histology: A Text and Colour Atlas* (Elsevier Health Sciences, 2013), 6th ed.

48. M. Pircher, E. Goetzinger, R. Leitgeb, and C. K. Hitzenberger, "Three dimensional polarization sensitive OCT of human skin in vivo," Opt. Express, OE **12**(14), 3236–3244 (2004).

49. G. Liu and Z. Chen, "Capturing the vital vascular fingerprint with optical coherence tomography," Appl. Opt., AO **52**(22), 5473–5477 (2013).

50. A. Zam, R. Dsouza, H. M. Subhash, M.-L. O'Connell, J. Enfield, K. Larin, and M. J. Leahy, "Feasibility of correlation mapping optical coherence tomography (cmOCT) for anti-spoof sub-surface fingerprinting," Journal of Biophotonics **6**(9), 663–667 (2013).

51. J. T. Whitton and J. d. Everall, "The thickness of the epidermis," British Journal of Dermatology **89**(5), 467–476 (1973).

52. S. Sakai, M. Yamanari, Y. Lim, N. Nakagawa, and Y. Yasuno, "In vivo evaluation of human skin anisotropy by polarization-sensitive optical coherence tomography," Biomed. Opt. Express, BOE **2**(9), 2623–2631 (2011).

53. M. Bonesi, M. P. Minneman, J. Ensher, B. Zabihian, H. Sattmann, P. Boschert, E. Hoover, R. A. Leitgeb, M. Crawford, and W. Drexler, "Akinetic all-semiconductor programmable swept-source at 1550 nm and 1310 nm with centimeters coherence length," Opt. Express, OE **22**(3), 2632–2655 (2014).

54. O. O. Ahsen, Y. K. Tao, B. M. Potsaid, Y. Sheikine, J. Jiang, I. Grulkowski, T.-H. Tsai, V. Jayaraman, M. F. Kraus, J. L. Connolly, J. Hornegger, A. Cable, and J. G. Fujimoto, "Swept source optical coherence microscopy using a 1310 nm VCSEL light source," Opt. Express, OE **21**(15), 18021–18033 (2013).

55. Y. Yasuno, J. Sugisaka, Y. Sando, Y. Nakamura, S. Makita, M. Itoh, and T. Yatagai, "Non-iterative numerical method for laterally superresolving Fourier domain optical coherence tomography," Opt. Express, OE **14**(3), 1006–1020 (2006).

56. T. S. Ralston, D. L. Marks, P. S. Carney, and S. A. Boppart, "Interferometric synthetic aperture microscopy," Nature Phys **3**(2), 129–134 (2007).

57. A. Kumar, W. Drexler, and R. A. Leitgeb, "Numerical focusing methods for full field OCT: a comparison based on a common signal model," Opt. Express, OE **22**(13), 16061–16078 (2014).

58. J. Mo, M. de Groot, and J. F. de Boer, "Focus-extension by depth-encoded synthetic aperture in Optical Coherence Tomography," Opt. Express, OE **21**(8), 10048–10061 (2013).

59. R. A. Leitgeb, M. Villiger, A. H. Bachmann, L. Steinmann, and T. Lasser, "Extended focus depth for Fourier domain optical coherence microscopy," Opt. Lett., OL **31**(16), 2450–2452 (2006).

60. A. Bouwens, T. Bolmont, D. Szlag, C. Berclaz, and T. Lasser, "Quantitative cerebral blood flow imaging with extended-focus optical coherence microscopy," Opt. Lett., OL **39**(1), 37–40 (2014).

61. M. Villiger, J. Goulley, M. Friedrich, A. Grapin-Botton, P. Meda, T. Lasser, and R. A. Leitgeb, "In vivo imaging of murine endocrine islets of Langerhans with extended-focus optical coherence microscopy," Diabetologia **52**(8), 1599–1607 (2009).

Chapter 5

Improvement of imaging depth range

5.1 Introduction

The custom made dermatological multifunctional JM-OCT has been introduced in Chapter 3. And its ability for skin imaging and investigation has been demonstrated as well. However, as mentioned in the discussion part of the previous chapter, the narrow imaging depth range still limits the availability of JM-OCT. Therefore, it is necessary to enlarge the imaging depth range of JM-OCT to be suitable for skin imaging or other biological tissues. In this chapter, the details of the system improvement are presented. After the system upgrade, the performance parameters and image quality were tested to confirm the status and ability of the advanced JM-OCT.

5.2 Method

It is known that the imaging depth range of SS-OCT is limited by several factors, such as depth of focus [1], coherence length (or instantaneous linewidth) of the swept source[2–4], and sampling numbers[5]. There are few approaches corresponding to these limiting factors to overcome the insufficient depth range of SS-OCT. Among these approaches, the long-coherence and befitting sampling per wavelength sweep are two optional means. Furthermore, for JM-OCT, the imaging depth range is also related to the difference of optical path length between the two multiplexed polarized beams. Thus, the delay between the two polarization states is also one controllable factor for deeper imaging.

5.2.1 Long-coherence swept source

There are several papers have demonstrated that the long-coherence swept source enables extended axial imaging range for SS-CT. Therefore, to improve the imaging depth range for the multifunctional JM-OCT, an OEM type 1310-nm swept source (Fig. 5.1 [6]) with a longer coherence (AXP50124-8; Axsun Technologies, MA) was employed to substitute the conventional narrow coherence length swept source. This light source is also a micro-electromechanical system based swept laser, which is suitable for a compact OCT system. The main performance parameters of the new 1310-nm swept source are listed in Table 5.1. Compare with the original light source (AXA 10823-8; Axsun Technologies, MA), the new one possesses not only relatively longer coherence length (39 mm) but also higher output power (39 mw). The coherence length and output power of the original 1310-nm swept source is around 13 mm and 22.6 mW, respectively. However, the sweep rate and wavelength tuning range of them are almost the same.

Although the center wavelength and the wavelength tuning range of both light sources are almost the same, the directions of the wavelength sweep of them are opposite. The old light source sweeps the

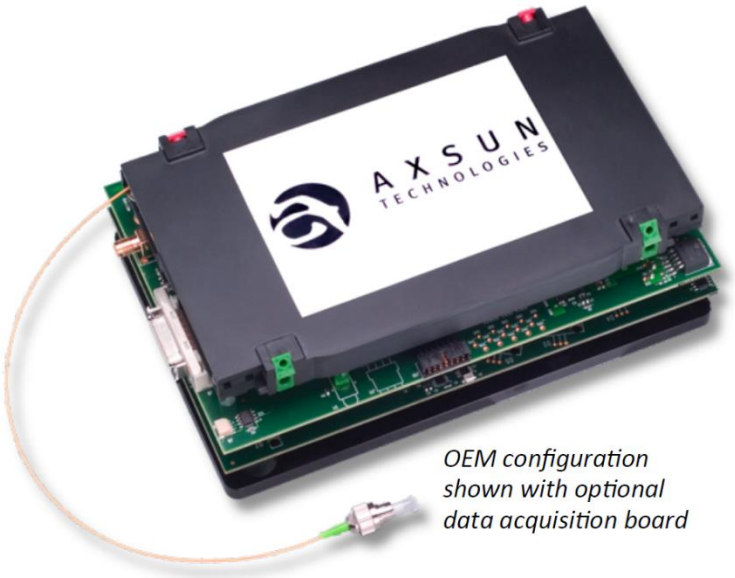

Figure 5.1: Axsun swept laser OEM engine [6].

wavelengths from short ones to long ones; however, the new swept laser sweeps the wavelengths from long ones to short ones. And we used a fiber Bragg grating (FBG) to generate an external A-line acquisition trigger, which is almost at the same timing with the internal A-trigger of the light source. Therefore, the fiber Bragg grating (FBG) was also changed to generate the A-line acquisition trigger at the correct spectral sweeping point, where the timing of internal A-trigger of the new light source appears.

Table 5.1. Performance parameters of new swept source.

Parameters	Test Value
Center Wavelength	1308.83 nm
Wavelength Tuning Range	107.75 nm
Sweep Rate	49.96 kHz
Average Power	39.024 mW
Coherence Length	39.42 mm

5.2.2 Achieve sufficient sampling points

To ensure the sufficient depth range, the sampling points have to be increased and match the axial resolution and expected imaging depth range. Hence, to achieve enough sampling points, a frequency multiplier (MK-3,

0.1 – 300 MHz output; Mini-Circuits, NY, Fig. 5.2) was applied to double the *k-clock* frequency. The effective input and output frequency ranges of the frequency multiplier are from 0.05 – 150 MHz and 0.1 – 300 MHz, and its multiplication factor is 2. To clean up the input *k-clock* frequency to the frequency multiplier, a low-pass filter (DC-158 MHz; Mini-Circuits, NY) and a high-pass filter (140 – 2000 MHz, Mini-Circuits, NY). As mentioned before, in the JM-OCT system, the imaging depth range is also associated with the delay

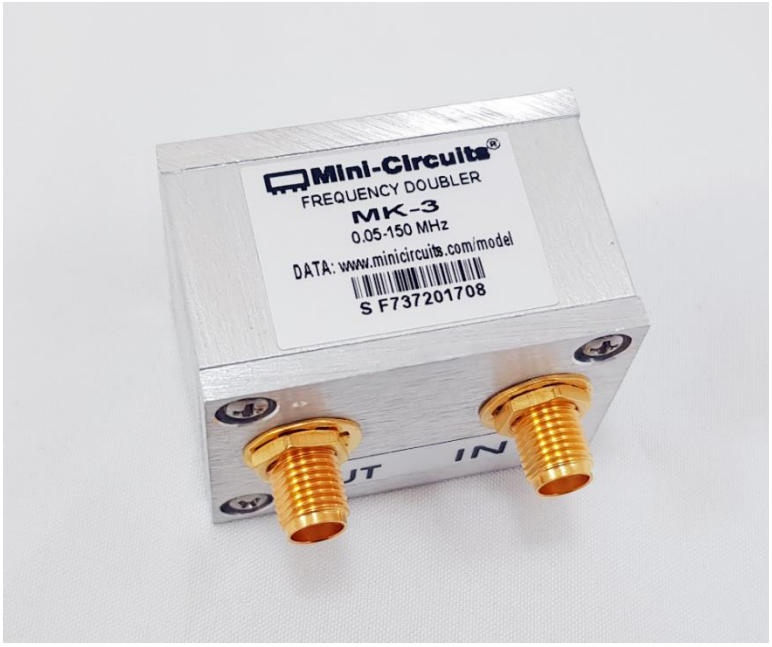

Figure 5.2: Photograph of the frequency multiplier.

between the two multiplexed polarized beams in the sample. Consequently, the delay between the two polarized probe beams was extended by adjusting the passive polarization delay in PPDU (DE-G036-13, Optohub Co., Ltd., Saitama, Japan). Then, the total measuring depth range achieved to 7.8 mm in air (5.6 mm in tissue, the refractive index of tissue is 1.38), which contains 804 sampling points per A-line. However, the two OCT images obtained from two incident polarized beams are multiplexed at different depths in tissue. Thereby, the imaging depth range of each OCT image from the four polarization channels is 3.9 mm in air (2.8 mm in tissue). It is 1 mm larger than the previous multifunctional JM-OCT imaging depth range.

5.3 Performance test

After optimizing the system, the performance parameter was measured.

5.3.1 Loss of each part of sample arm

- Coupler between light source and PPDU: -0.08dB
- PPDU: -1.69dB
- PPDU to Probe (consists of circulator and probe): -1.5dB
- Probe to Detector (includes mirror calibration): -2.3dB

5.3.2 Probe and reference power

The probing beam power was increased to be around 17 mW after changing the light source and optimizing the system. The trend of system sensitivity changes along with the reference power was measured to confirm the appropriate reference power. The result is shown as Fig. 5.3. It suggested that the relatively high sensitivity is obtained when the reference power is around 3.0 mW. Therefore, the reference was set at 3.0 mW.

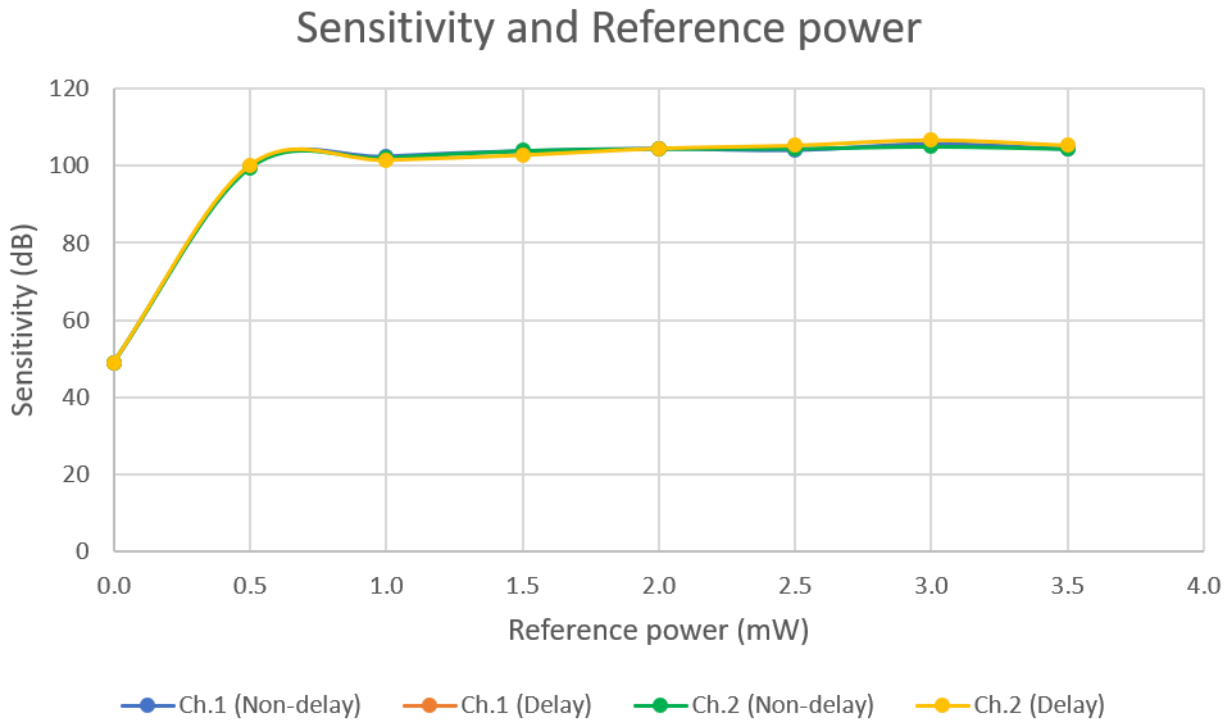

Figure 5.3: Sensitivity changing trend with reference power.

5.3.3 Sensitivity and resolution

After optimized the reference power and DAQ range (100 mV), the sensitivity and axial resolutions were measured. The intensity and background of the OCT signals of each channel, which corresponds to the four entries of the Jones matrix, are shown in Fig. 5.4. With the measured data of signal intensity and background, the sensitivity of the four polarization channels were calculated to be 105, 105, 104, and 104 dB (Table 4.3.3).

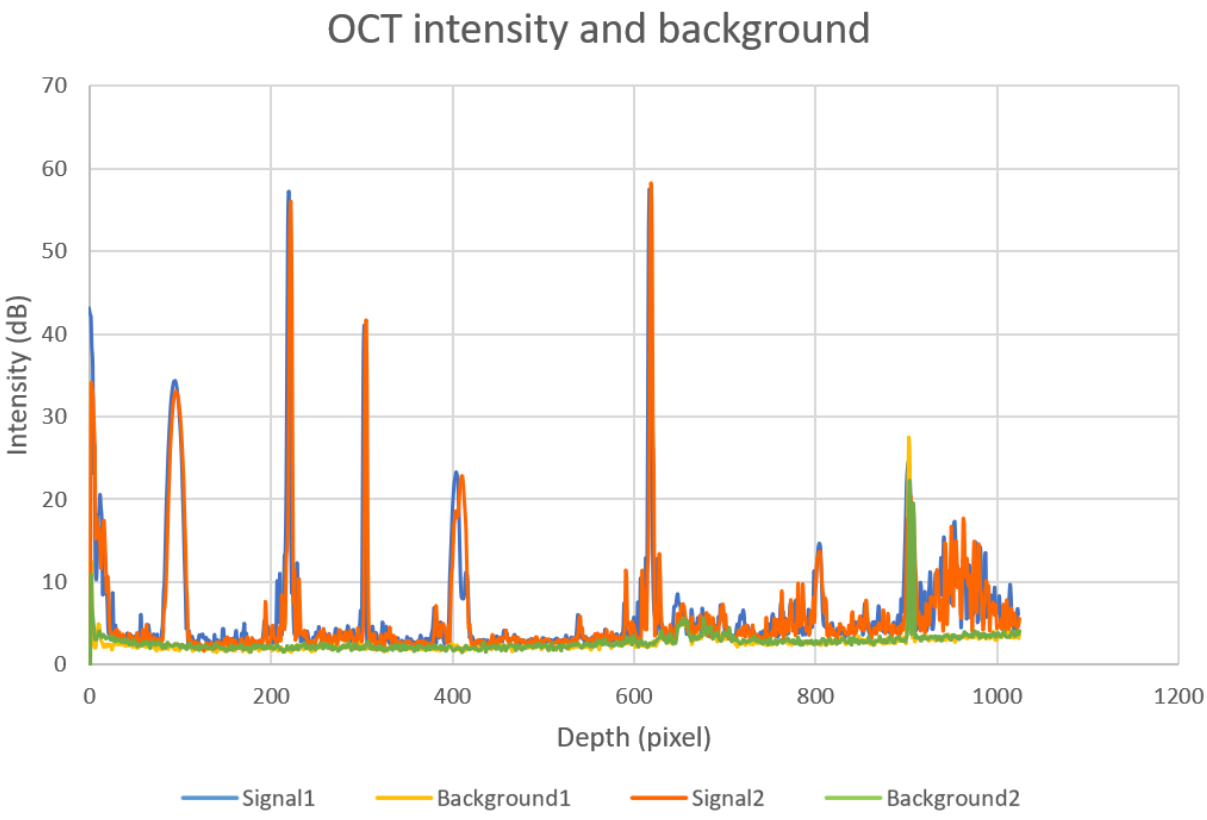

Figure 5.4: Intensity of OCT signals and background measured at 3.0-mW reference power.

Table 5.2 Sensitivity of each channel

Depth (z) / Channel No.	**Non-delay (220 pixel)**	**Delay (617 pixel)**
Ch. 1	105 dB	104 dB
Ch. 2	103 dB	105 dB

5.3.4 Resolution

The axial resolution (full width at half-maximum) was measured to be 19.4 μm in air (14.1 μm in tissue), and the lateral resolution ($1/e^2$ beam diameter at the beam waist) was 19 μm. The depth pixel separation was measured to be around 9.8 μm in air (7.1 μm in tissue).

5.4 Imaging quality test

The *in vivo* human skins at different locations were measured to test the imaging quality of the improved multifunctional JM-OCT. The *in vivo* finger pad and inner-forearm skin tissues were measured for easy comparison with the original version JM-OCT. By evaluating the accuracy of the birefringence images generated with different calculating depth separations, the calculating depth separation of the birefringence image process was modified 8 pixels. In the previous birefringence image postprocess, the calculating depth separation is 6 pixels. After modifying the calculating depth separation, the artifacts were reduced. Two sets multi-contrast images are displayed as examples.

5.4.1 Multi-contrast imaging of the finger pad skin

Figure 5.5 shows the *in vivo* multi-contrast imaging of finger pad skin. Fig. 5.5 (a) is a cross-sectional scattering OCT of the tissue. From this image, the epidermal and dermal layers can be discriminated, and the sweat ducts in the epidermis also can be observed clearly. Fig. 5.5 (b) is a B-frame of OCT-A image, which contrasts the blood flow in the tissue. In the Figs. 5.5 (c) and (d), the different degree of the polarization uniformity and birefringence are observed in epidermal and dermal tissues of the finger pad skin. The *en face* images in Figs. 5.5 (e) – (h) corresponding to Figs. (a) – (d) are at the-0.53 mm depth below the surface, where locates the superficial dermis tissue. In Figs. (e), (g) and (h) the fingerprint still appears with relatively bright bands and dark bands. And partial vasculature in the superficial dermis are visualized.

5.4.2 Multi-contrast imaging of the inner-forearm skin

Another test result example is the multi-contrast imaging for inner-forearm skin tissue, which is shown as Fig. 5.6). Same with the finger pad skin measurement, the cross-sectional scattering intensity OCT [Fig. 5.6(a)], OCT-A [Fig. 5.6(b)], DOPU tomography [Fig. 5.6(c)], birefringence tomography [Fig. 5.6(d)], and their corresponding *en face* images at 0.53-mm depth location under the surface [Figs. 5.6 (e) – (h)] are obtained. In these multi-contrast images, the micro-structures and blood flow (blood vessels) can be observed. The optical properties, especially, the polarization property of the epidermal and dermal tissues of inner-forearm skin can be investigated. Compare with the birefringence image of the inner-forearm skin acquired by the JM-OCT before improvement (Chapter 4), the improved multifunctional JM-OCT achieved relatively deeper tissue imaging. And the birefringence image shows fewer artifacts than the previous results, especially for the low SNR microstructures.

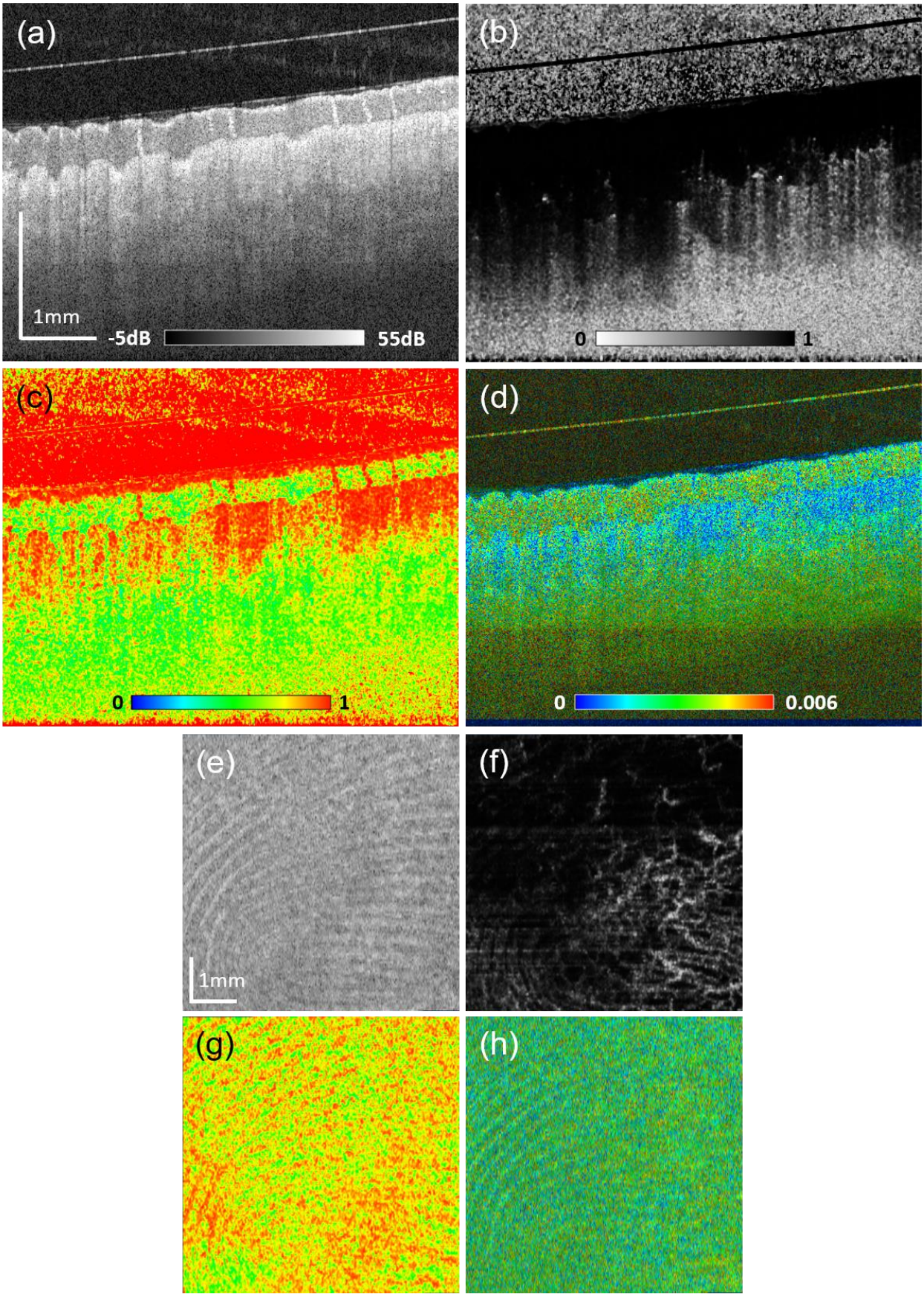

Figure 5.5: Multi-contrast images of finger pad skin. Cross-sectional (a) intensity, (b) OCT-A, (c) DOPU, and (d) birefringence images. (e) – (h) are the corresponding *en face* images at 0.53-mm depth below the surface.

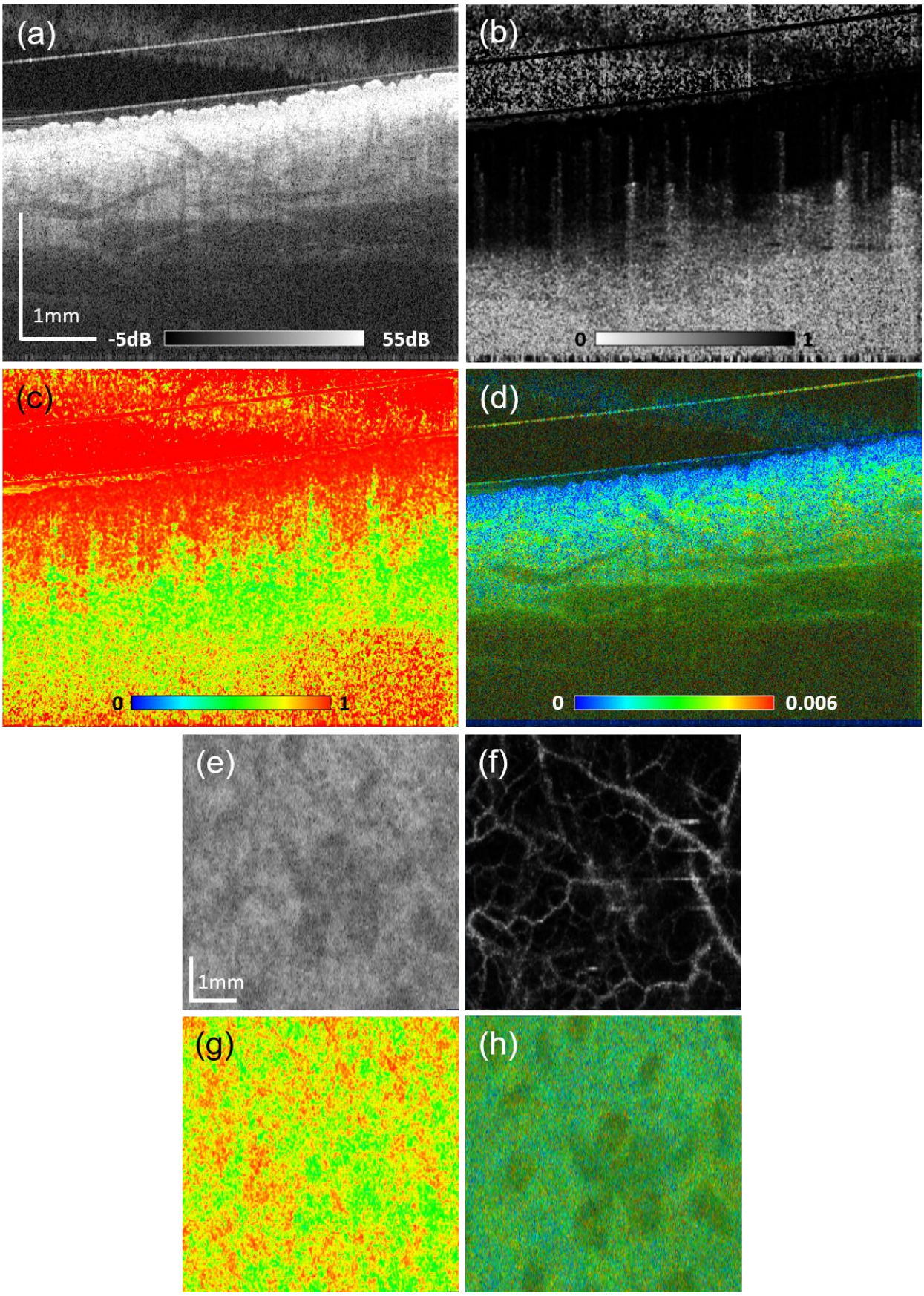

Figure 5.6: Multi-contrast images of inner-forearm skin. Cross-sectional (a) intensity, (b) OCT-A, (c) DOPU, and (d) birefringence images. (e) – (h) are the corresponding *en face* images at 0.53-mm depth below the surface.

5.5 Discussion and conclusion

After changing the light source and redesigning the sampling points, the imaging depth range of the dermatological multi-functional JM-OCT was improved to be around 2.8 mm in tissue. Because of the limited delay between the two multiplexed polarizations generated by the PPDU, the current imaging depth range is not enhanced to the designed ideal value. The used sampling points per A-line is 804 pixels, in fact, the full setting sampling points per A-line during the measurement is 1024. Hence, if the delay between the two incident polarized beams in PPDU is enough, the imaging depth range would be up to around 3.6 mm in tissue. Although the insufficient delay of PPDU limits the actual imaging depth range, the current imaging depth range is still 1-mm deeper than the previous result. The performance parameter measurement and imaging quality test results demonstrated that the working status and performance of the improved JM-OCT system is not degraded. The birefringence images show fewer artifacts by modifying the birefringence calculating depth separation.

5.6 Summary

Although multi-functional JM-OCT system has been successfully developed and demonstrated to *in-vivo* imaging in chapter 3, the shallow imaging depth range still limits the availability of JM-OCT. In this chapter, the system is further upgraded and the details of the improvement in the imaging depth are presented. Through utilizing long-coherence swept source and increased sampling points, the 1-mm deeper imaging was achieved in success. Particularly, there is no clearly observable degradation is found and the birefringence images in the test show fewer artifacts-especially for the low SNR microstructure by modifying the birefringence calculating depth separation. With the refitting JM-OCT system, the depth imaging in skin has been remarked improvement. Additionally, the enhancement may provide more degree of freedom to integrate new functionalities into in the current system for further dermatological imaging.

References

1. B. E. Bouma and G. J. Tearney, *Handbook of Optical Coherence Tomography* (New York : Marcel Dekker, 2002).

2. C. Chong, T. Suzuki, K. Totsuka, A. Morosawa, and T. Sakai, "Large coherence length swept source for axial length measurement of the eye," Appl. Opt. **48**(10), D144–D150 (2009).

3. O. Kolokoltsev, I. Gómez-Arista, C. G. Treviño-Palacios, N. Qureshi, and E. V. Mejia-Uriarte, "Swept Source OCT Beyond the Coherence Length Limit," IEEE J. Sel. Top. Quantum Electron. **22(**3), 222–227 (2016).

4. B. R. Biedermann, W. Wieser, C. M. Eigenwillig, T. Klein, and R. Huber, "Direct measurement of the instantaneous linewidth of rapidly wavelength-swept lasers," Opt. Lett. **35(**22), 3733–3735 (2010).

5. Y. Yasuno, V. D. Madjarova, S. Makita, M. Akiba, A. Morosawa, C. Chong, T. Sakai, K.-P. Chan, M. Itoh, and T. Yatagai, "Three-dimensional and high-speed swept-source optical coherence tomography for in vivo investigation of human anterior eye segments," Opt. Express **13**(26), 10652–10664 (2005).

6. "OCT Swept Laser Engines," https://www.axsun.com/oct-swept-lasers.

Chapter 6

Multifunctional JM-OCT based optical coherence elastography

6.1 Introduction

Jones-matrix optical coherence tomography (JM-OCT) is capable of measuring tissue birefringence[1], while optical coherence elastography (OCE) reveals the mechanical properties[2] of the tissue. Since both birefringence and mechanical properties are associated with tissue microstructures such as collagen, it is worth investigating the relationship between birefringence and biomechanical properties of a tissue.

There already have been several studies on the utilities of tissue birefringence measurement, mechanical property measurement[3], and their combination[4]. However, these studies are not based on spatial-resolved methods. On the other hand, PS-OCT and OCE provide spatially resolved birefringence and mechanical property, respectively. However, simultaneous birefringence and mechanical property imaging is not yet demonstrated.

In this chapter, we propose a new method for simultaneous imaging of birefringence and biomechanical properties of tissue. This method is a Jones-matrix based PS-OCT equipped with a tissue compression probe. It simultaneously provides birefringence tomography, scattering intensity, depth-resolved in-plane axial and lateral displacements, and microstructural decorrelation maps of a biological tissue. The combination of the birefringence and biomechanical images provides more comprehensive and detailed understanding of tissue microstructure than sole PS-OCT or OCE investigation.

6.2 Optical coherence elastography

6.2.1 Overview

Medical researchers have demonstrated that the pathological alteration of biological tissue is always accompanied by the mechanical property (stiffness or elasticity) change of the tissue. Therefore, the quantitative measurement of the elasticity information of the tissue provides a useful approach for clinical diagnosis [5–8]. Currently, mainly applied elastography technologies in clinical medicine are ultrasound elastography (USE) and magnetic resonance elastography (MRE). However, there are still several issues that exist in these methods, such as long measuring time, low resolution and high cost.

OCT is a noninvasive, fast and high-resolution biomedical imaging modality, which enables imaging for microstructures of tissue with a submillimeter scale and few millimeters depth-penetration. With these characteristics of OCT, the combination of OCT and elastography technology provides a new alternative approach for mechanical property imaging of biomedical tissue. The OCT based elastography technology denominated as optical coherence elastography (OCE) was first invented by Schmitt in 1998 [9]. Schmitt installed a compressive mechanism into the sample arm of OCT, and the active compressive load was applied on the anisotropic gelatin phantom and biological samples to drive the deformation in the samples during the

OCT measurement. Then, by utilizing a two-dimensional correlative speckle tracking estimation method, the local displacement image can be obtained. Furthermore, with this local displacement image, the strain distribution can be estimated as well. This study demonstrated a new potential of the extended function to OCT, which provides not only optical scattering property but also biomechanical property of the tissues. Compare with the optical property images, the elastic image is an intrinsically different contract. Therefore, it could supplement the important information of biological tissue to optical imaging in medical investigation. Since then, with the advances of OCT and its related technology, the OCE has been rapidly developed to support biomedical can clinical investigation [10–14] in past decades. Especially after the FD-OCT was developed, the quantitative OCE measurement was achieved and the performance of the OCE system was improved as well [11,15].

6.2.2 Principle and category

So far, there already have been many means to implement the OCE measurement [10,16,17]. All of these OCEs mainly consists of two parts: an OCT system used for tissue imaging and a mechanical load used for driving tissue deformation. There are many papers have described the principle of OCE in details, here I will summarize it briefly. In simple terms, the tissue is first deformed under an active mechanical load when it is measured by an OCT system. And the micro displacements in the tissue is then calculated with the OCT images. By utilizing an appropriate and simplified model or a mechanical model of the continuous medium, the mechanical property of the tissue finally can be estimated and visualized in an elastic mapping.

Similar to ultrasound elastography, there are two major categories in OCE technology, one is Static (or quasi-static) OCE and the other is dynamic OCE [10]. In addition, on the basis of the spatial excitation characteristics of the tissue, OCE technology also can be classified into two types: internal and external excitations. And both of static and dynamic OCEs can be employed for either internal or external tissue excitations [16,18].

To implement the OCE measurement, there are several different methods of the mechanical loading on tissue and the estimation of the resulting displacement in tissue. Based on different mechanical loading methods there are various OCE modalities, such as compression OCE [15,19], surface acoustic wave OCE (SAW OCE) [20], Shear wave OCE (SW OCE) [21], acoustic radiation force OCE (ARF OCE) [22], magnetomotive OCE (MM OCE) [23]. For displacement estimation, the commonly used methods are speckle tracking [24], phase-sensitive detection [11] and Doppler spectrum detection [25]. Among the above-mentioned approaches of OCE with different mechanical loadings, the compression OCE is a relatively mature technique. And it is promising as an optical biopsy method because of its non-invasive, rapid and relatively high-resolution imaging properties. Furthermore, the compression OCE can be combined anyone of the three displacement estimating methods. Therefore, the Jones matrix based optical coherence elastography developed by us, which will be introduced in section 6.3, also uses the compression loading method.

6.2.3 Compression optical coherence elastography

Compression-based OCE belongs to the quasi-static, external excitation OCE technology. It uses a uniaxial, active compressive loading on the whole measuring region of the sample (Fig. 5.2.3), and the step-change of the loading force is synchronized to the OCT acquisition [15,16,19,26]. Then the axially localized displacement is calculated by the OCT images obtained under different loading (usually are with and without loading). As shown in Fig. 6.1, with the change of axial displacement Δu_z over a local small depth range Δz, the corresponding local strain ε_z can be estimated as [16]

$$\varepsilon_z = \frac{\Delta u_z}{\Delta z} \quad (1).$$

Finally, the elastography, which characterizes the mechanical property of tissue, is formed by the distribution of the estimated local displacement.

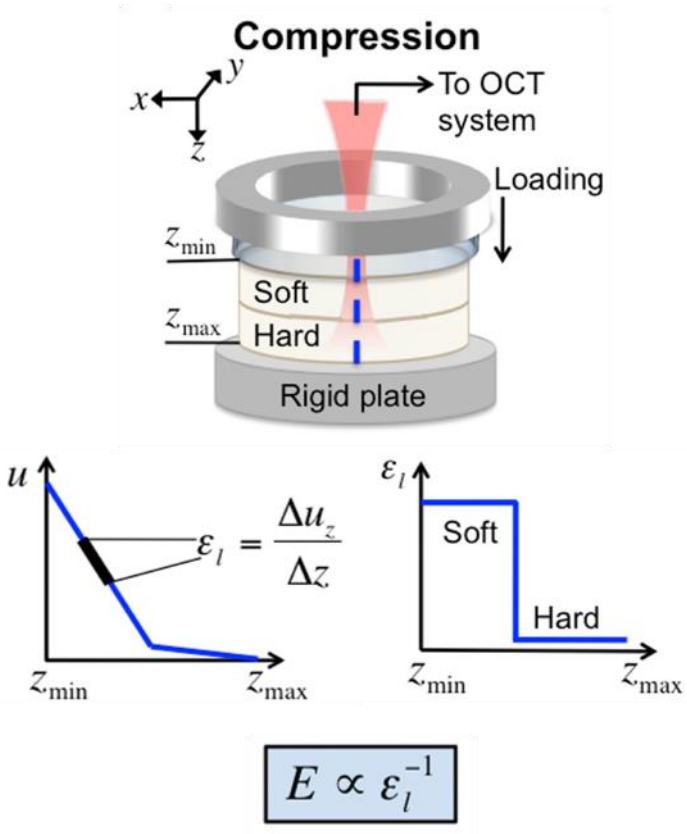

Figure 6.1: Schematic of the uniaxial compression OCE.

In the early stage of compression OCE development, tissue mechanical properties were qualitatively observed by local displacement and strain measurements [24,27]. However, to quantitatively analyze the mechanical properties of tissues, i.e., to measure the elastic modulus, the stress on a tissue should be measured

in addition to the strain. Therefore, a compliant layer has recently been employed to estimate the local stress on a tissue, and *en face* mapping of the tangential modulus was demonstrated [15,28].

Despite its success, compression OCE relies on several assumptions. Among them, the major assumptions are constant axial stress, isotropic tissue mechanical properties, and the absence of lateral tissue displacement [2,15,16,28,29]. However, these assumptions are not always valid.

The artifacts (or errors) caused by violation of the first two assumptions can be eliminated using the approach of iteratively solving the inverse elasticity problem [30]. This method is successful in resolving the inaccuracy problem of uniform axial stress and assumptions of isotropic mechanical properties. This method could be more robust if the lateral displacement information was available. However, compression OCE with a lateral-displacement-measurement capability has not yet been demonstrated. To overcome these limitations of compression OCE, it is necessary to perform a lateral displacement measurement.

In the next section, we first propose a new method of axial and in-plane lateral displacement measurements based on a multifunctional JM-OCT system. This method uses OCT images of a tissue obtained from JM-OCT under two different compressive conditions. Using complex correlation maps computed from these two OCT images, depth-resolved axial and lateral displacement maps of the tissue are obtained. In addition, a depth-resolved microstructural decorrelation (MSD) map is obtained. When a tissue is compressed, microscopic deformation of the tissue ultrastructure, which is smaller than the OCT resolution, occurs in addition to the relatively macroscopic displacement of in and out of the cross-sectional plane in OCT. The MSD map qualitatively visualizes the combined effect of the microstructural deformation and out-of-plane displacement, whereas the current compression OCE only measures tissue displacement and strain. Finally, by utilizing the multiple contrasts including OCT, birefringence tomograms and displacements, MSD maps, the optical and mechanical properties are analyzed.

6.3 JM-OCT based optical coherence elastography

6.3.1 System

To achieve simultaneous imaging for tissue optical and mechanical properties estimation, the optical coherence elastography (OCE) was developed based on an advanced 1.3-μm swept source Jones matrix OCT (SS-JM-OCT), which was introduced in Chapter 4. The configuration of the system is detailed in Section 2.1 of Ref. [31]. To sum up, the system consists of two parts: a JM-OCT system and a tissue deformation driving equipment for elastic imaging. As shown in Fig. 6.2, the swept laser is from a long coherence light source (40 mm coherence length, AXP50124-8; Axsun Technologies, MA) with a 1310-nm center wavelength, an around 40-mW averaging output power, and a scanning range of 50 kHz. It is divided by a 90/10 broadband coupler

(FC1310-70-10-APC, Thorlabs Inc., NJ), and then 90% of the light source power is sent to the sample arm, the other 10% is sent to the reference arm.

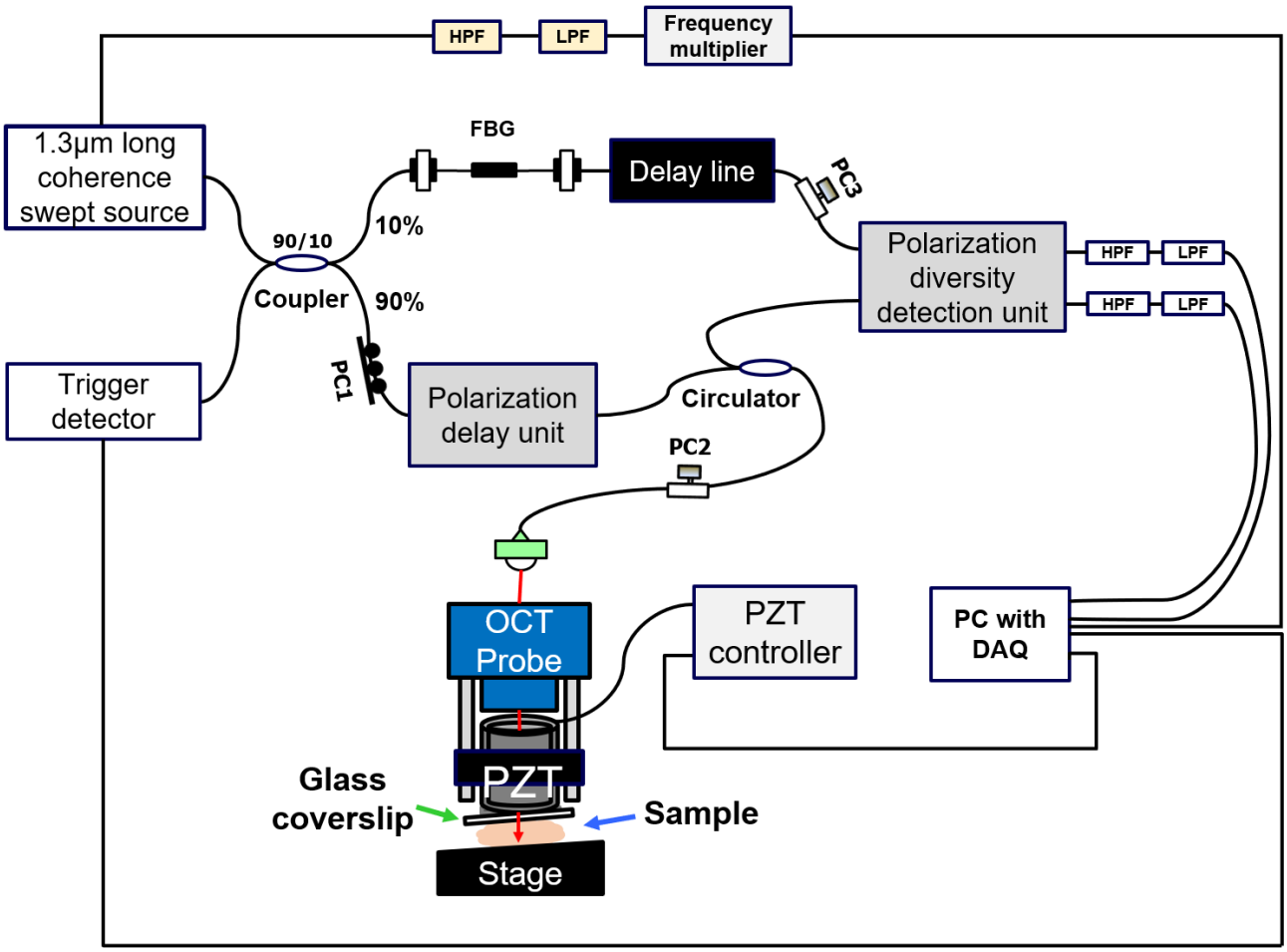

Figure 6.2: Configuration of the Jones matrix based OCE system. PC1, PC2 and PC3: polarization controllers; HPF: high pass filter, and LPF: low pass filter.

In the sample arm, the beam is first optimized by a polarization controller (PC1) and goes into a commercial passive polarization delay unit (PPDU, DE-G043-13, Optohub Co. Ltd., Saitama, Japan), which is applied for multiplexing the two orthogonal independent incident polarization states into two different depths in the OCT image by a mutual delay between the two beams [1]. The output beam from the PPDU goes through a broadband circulator (CIR-1310-50-APC, Thorlabs) and an OCT probe equipped with an active compressive unit to scan the sample. The compressive unit consists of a ring piezoelectric transducer (PZT; HPSt 150/20-15/12 VS35 SG; Piezomechanik GmbH, Germany), a glass coverslip (0.4 mm in thickness) and a PZT controller (M-26110S-1, 250 Hz, 12-μm maximum stroke, MESS-TEK Co., Ltd., Saitama, Japan). This configuration is similar to that in Ref. [2]. The glass coverslip, which is used to compress the measured tissue, was attached to the front end of the PZT. And the PZT was installed in front of the objective (effective focal length = 54 mm, working distance = 42.3 mm, LSM04; Thorlabs). The PZT is controlled by the PZT controller with the actuating signal sent from the computer. Therefore, the tissue deformation can be driven

synchronously with the OCT measurement. The OCT probing beam passes through the ring PZT and glass window to scan the sample. The back scattered lights from the tissue layers are optimized with a polarization controller (PC2) and sent to the commercial polarization diversity detection unit (PDDU, DE-G036-13, Optohub). The lateral resolution ($1/e^2$-width) and axial resolution (full width at half-maximum) were 19 and 14 μm in the tissue, respectively. The imaging range was 2.0 × 2.8 mm (width × depth).

In the reference arm, the optimized reference beam is first sent to a fiber Bragg grating (FBG, FBG-SMF-1354-80-0.2-A-(2)60F/E, ⩾80% reflectivity at 1354 nm; Tatsuta Electric Wire & Cable Co., Ltd, Osaka, Japan), which is employed to generate the A-line acquisition trigger, and after passing a variable delay line (Advanced Fiber Resource Ltd., Hong Kong, China) it goes into the PDDU. The beams from the reference and sample arms are interfered with each other in PDDU, and the interference signal is then detected by the PD-detectors of PDDU.

As mentioned in the previous chapter (Chapter 4), a frequency multiplier (MK-3, 0.1–300 MHz output; Mini-Circuits) connected with a high pass filter and a low pass filter was applied to double the k-clock frequency. In addition, the passive polarization delay of the probe beam was enlarged as well for a larger imaging depth range, which is around 2.8-mm depth range in tissue. The sensitivity was measured to be around 104 dB for each polarization channel.

6.3.2 Measurement protocol

For the measurement, 512 B-scans covering 2.0 mm were sequentially acquired at the same location. One B-scan contained 512 A-lines. During the consecutive B-scan acquisition, the PZT continuously compressed the tissue by 12 μm. Therefore, two adjacent B-scans were obtained with a 0.023 μm compression difference. Displacement and MSD images were computed using the two OCT images with an *n*-B-scan interval corresponding to the 0.023*n* μm compression difference. In this research, the interval of two selected B-scans is 40. Thus, the compression difference of the two B-scans is about 0.9 μm.

6.3.3 Imaging process

6.3.3.1 Scattering OCT imaging

Because the OCT system used in this study employed JM-OCT, it had two incident and two detected polarizations, which can generate four OCT images. The OCT intensity images shows in this chapter are polarization-insensitive OCTs, each of which is obtained by averaging the four polarization-diversity OCT intensity signals.

6.3.3.2 OCE imaging

OCE was computed by the digital shifting complex correlation method [32]. First, the noise-corrected complex correlation (NCC) map [33] between two B-scans was computed. The NCC is a correlation in which the reduction of the correlation induced by noise is canceled based on a theoretical model of the OCT signal correlation and measured noise power. Then, an additional four correlation maps were computed between the target B-scan and four differently directionally shifted reference B-scans. The five correlation values at each point in the B-scan are explained by five simultaneous equations that are parametrized by five unknowns: in-plane lateral and axial displacements, lateral and axial resolutions, and an out-of-plane displacement. Here, all unknowns vary in the B-scan. Therefore, the simultaneous equation system is defined at each point in the B-scan. Finally, by solving the simultaneous equations, in-plane axial and lateral displacement, axial and lateral OCT resolution, and out-of-plane displacement maps were computed. Intuitively, this algorithm can be understood as splitting decorrelation into in-plane lateral and axial displacements, and an unexplained decorrelation. Because the correlation used in this method is the above mentioned NCC, the variations in the OCT signal intensity or signal-to-noise ratio (SNR) does not affect the result. However, if the SNR is too weak to provide the available information of the tissue structure, it would be hard to calculate the displacements and deformation maps of this part of the tissue.

This method was originally developed for in situ monitoring of tissue dynamics during retinal laser coagulation [32]. In the original method, residual decorrelation was interpreted as out-of-plane displacement. However, this component also reflects microscopic tissue alterations and deformation [32,34]. Thus, in this study, it is denoted as MSD.

Since four OCT images can be acquired by JM-OCT, four maps were obtained for each axial and in-plane lateral displacement. The final maps were obtained by weighted averaging of four maps corresponding to the polarization channel where the weight was the OCT intensity of each channel. Because the number of sequentially acquired B-scans is 512 and the interval of the B-scan pair for OCE computation is 40, 472 in-plane lateral and axial displacement image sets are obtained. A part of these images is averaged to reduce noise and artifacts.

6.3.3.3 Birefringence imaging

The birefringence image processing method is almost identical to that described in Chapter 4. However, the depth separation is modified to be 8 pixels as mentioned in Chapter 4, and the spatial kernel is set as 2 × 2-pixel, which is used in the maximum *a posteriori* (MAP) estimator to estimate the birefringence value for each pixel [31]. The same as the previous tissue birefringence visualizing method, the pseudo-color image is also applied in this part study for easy observation.

6.4 Experiment

To assess the performance of the JM-OCT based OCE, several different tissues including porcine carotid artery and esophagus tissues were measured. In the experiment, a moderate amount of silicon oil (AK 35, Wacker Silicones, Munich, Germany) was applied evenly on the surface of the sample to avoid the influence of the friction at the sample and glass coverslip interface.

6.5 Results

6.5.1 Porcine carotid artery tissue

We first applied this method to measure a dissected porcine carotid artery tissue close to heart prepared. Figure 6.3(a) shows the photo of the sample. As shown in the photo, the carotid artery was opened along with longitudinal direction and the inside was placed upwards under the probe. The short yellow line is the position of the B-scan. In order to drive large lateral displacement, a wire used as a phantom of a hard tissue was fixed

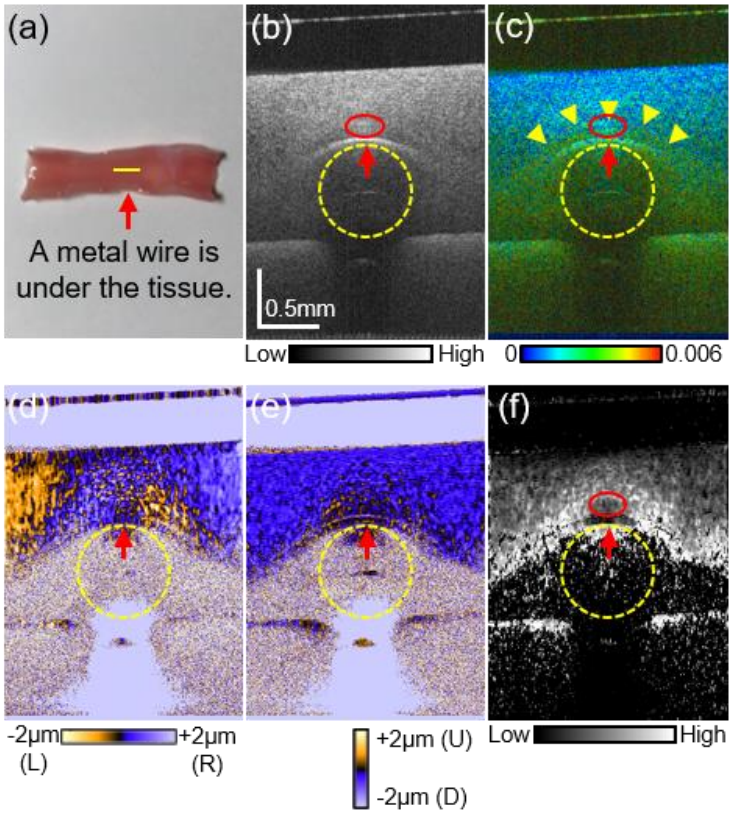

Figure 6.3: Photo (a), intensity OCT (b), local birefringence tomography (c), in-plane lateral displacement map (d), axial displacement map (e), and MSD map (f) of a piece of dissected porcine carotid artery on a metal wire. Red arrows in (b – f) indicate the metal wire surface. The yellow round dotted lines in (b – f) indicate the position of the metal wire.

beneath the center of the sample. The yellow circular dotted line in Figs. 6.3(b) – (f) indicate the position of the wire in the images. The red arrows indicate the surface of the metal wire.

In an OCT B-scan (Fig. 6.3(b)), there is almost no clearly visible tissue structure, but some low contrast lamellar structures are visible. A strong scattering at the bottom of the tissue is the surface of the metal wire (red arrow). In the corresponding birefringence image (Fig. 6.3(c)), most part of the tissue represents low birefringence, but lower part of the tissue exhibits a layer with moderate birefringence (green part, yellow arrow heads).

In the OCE maps (Figs. 6.3(d) – (f)) reveal the tissue comes about a significant microstructural alteration under the compression. As shown in lateral displacement maps (Fig. 6.3(d)), relatively larger lateral displacement come about in two outer parts of the tissue, where the outer left part moves to the left (yellow) and the outer right part moves to the right (blue). While, the middle and bottom parts around the metal wire of the tissue shows a complicated and inhomogeneous pattern, such as the left bottom part moves to the right and the right bottom part moves to the left. To interpret this complicated alteration of the tissue, more detailed numerical analysis of tissue mechanics is necessary. On the other hand, the upper middle part of the tissue shows much less displacement than both end parts of the tissue, but the pattern of this part is similar to the lamellar structures of the tunica media.

In the corresponding axial displacement image (Fig. 6.3(e)), the major part of the tissue moves downward (blue), except the mid-bottom part of the tissue that contacts with the metal wire surface. This part has almost no axial displacement (black).

The MSD image (Fig. 6.3(f)) shows that the lower part of the tissue has a larger decorrelation in general, i.e., its microstructural deformation is larger than the upper tissue. It can be interpreted as that the tunica externa has larger microstructural deformation than the elastic lamina tissue, i.e., the tunica externa is softer than the tunica media. An exception can be found just above the metal wire surface (red ellipse), where the deformation is low (black) and it indicates the tissue is stiff. This region shows a hyper-scattering lamellar structure in the OCT (Fig. 6.3(b)) and moderately high birefringence (green, Fig. 6.3(c)).

6.5.2 Porcine esophagus tissue

The second measurement is of a dissected porcine esophagus tissue. As shown in the photo (Fig. 6.4(a)), the esophagus tissue was opened along the longitudinal direction, and the inside was set towards to the OCT's probe. The short yellow line at the center of the tissue indicates the position of OCT B-scans. And the B-scan is along the circumferential direction. The total thickness of the tissue with compressive preload before measurement is around 2 mm. However, the deep region, such as the tissue located under 0.8 mm from the surface, is not observed because of the limited penetration of OCT.

In the birefringence tomography of the tissue (Fig. 6.4(c)), the superficial part of the tissue shows low birefringence (blue) as indicated by a red arrow. And the layer beneath this low birefringent layer shows intermediate birefringence (green) as indicated by a yellow arrow. However, in the corresponding OCT (Fig. 6.4(b)), these two layers are difficult to be distinguished because of their similar scattering intensity. We only can observe low intensity at the interface between these two layers, but not clearly. The MSD map (Fig. 6.4(f)) does not show clear contrast between these two layers. It indicates the stiffness of these two layers are similar.

A low scattering structure with a lamellar appearance can be seen in the scattering OCT (Fig. 6.4(b), pink arrow). The MSD map (Fig. 6.4(f)) shows relatively high deformation (light gray) at this region, it indicates this part of the tissue is softer than others.

The in-plane axial displacement map (Fig. 6.4(e)) shows overall downward displacement. On the other hand, the in-plane lateral displacement map (Fig. 6.4(d)) shows that the left part tissue moves to left (yellow), and the right part tissue moves to right (blue). Namely, the tissue is laterally expanded. It is noteworthy that this lateral expansion occurred without localized hard material, such as the metal wire used in the previous case. In general, when the tissue is compressed axially, it should expand laterally in order to preserve its volume. So, the lateral displacement found in Fig. 6.4(d) is rational.

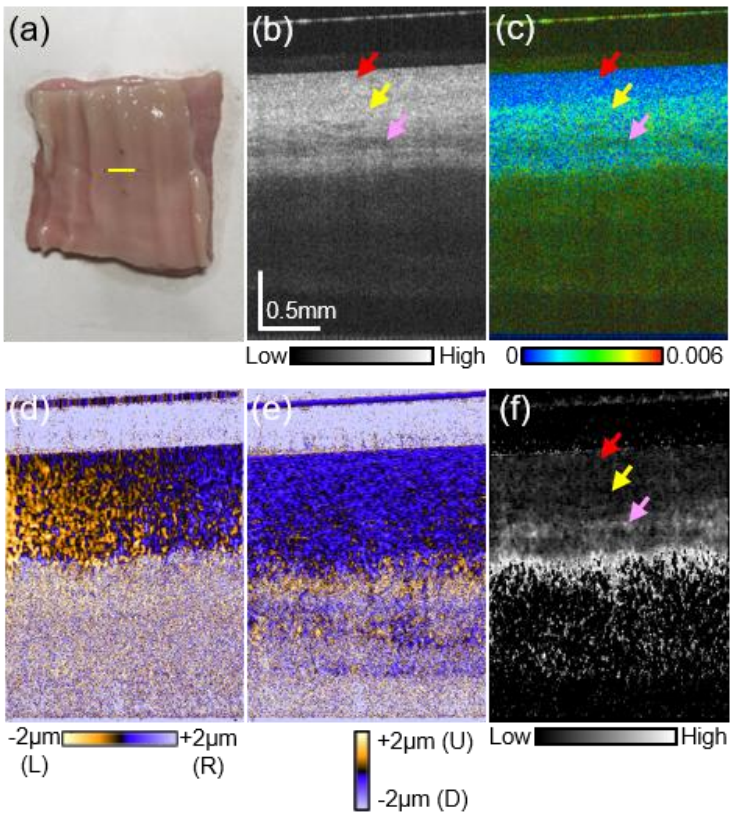

Figure 6.4: Photo (a), intensity OCT (b), local birefringence tomography (c), in-plane lateral displacement map (d), axial displacement map (e), and MSD map (f) of a piece of dissected porcine esophagus. Different color arrows in (b), (c) and (f) indicate the different layers in tissue. The short yellow line in (a) indicates the position of B-scan.

In this measurement, although there was no wire, the lateral displacement was still observed because, when a material is compressed (or stretched), it tends to expand (or contract) in directions perpendicular to the direction of the external force. This phenomenon is called the Poisson effect. Moreover, Poisson's ratio represents the compressibility of a material. Biological material can be considered as an incompressible, i.e. volume-preserving, material. Therefore, its maximal Poisson's ratio would be close to 0.5 [35]. In this case, to preserve its volume, the tissue expands laterally to accommodate the axial displacement.

From the results of the above two cases, we conclude as follows. The scattering OCT, birefringence, and biomechanical images revealed different tissue structures. Namely, some tissue structures can be found only in some types of images. It suggests that sole use of OCT, birefringence or biomechanical imaging is not sufficient to visualize all of the tissue structures. The displacement imaging revealed that significant amount of lateral displacement is induced by axial compression. It implies that not only axial but also lateral displacement measurement is important for compression based OCE.

6.6 Discussion and conclusion

According to the image appearances, the MSD map is more similar to in-plane axial displacement than in-plane lateral displacement. However, it does not suggest a real connection between axial displacement and MSD. The MSD map can visualize only the absolute value of displacement. Therefore, it has no directionality information, whereas the in-plane lateral displacement map visualizes bidirectional displacement. However, the axial displacement induced by the compression is monodirectional in practice, although the method itself can measure bidirectional axial displacement. These directionality properties of the map would be the reason for the resemblance.

The spatial resolutions of the displacement and deformation measurements were defined by three independent factors including OCT imaging resolution, the kernel size of the correlation computation, and digital shifts of the reference B-scan. The OCT imaging resolution was defined by both the optical resolution and pixel separation. In this case, the optical resolutions were 19 μm (lateral) and 14 μm (axial in tissue), while the pixel separations were 3.9 μm and 7.0 μm, respectively. Thus, the lateral and axial OCT image resolutions were dominated by the optical resolution, which were Δx_oct = 19 μm (lateral) and Δz_oct = 14 μm (axial). The second factor, the correlation kernel size, was 7 × 7 pixels. By multiplying the pixel separations, the kernel occupied Δx_ck = 27.3 μm (lateral) and Δz_ck = 49 μm (axial in tissue). The third factor, the digital image shift, was ± 1 pixel. It corresponded to Δx_ds = 7.8 μm (lateral) and Δz_ds = 14 μm (axial in tissue). The overall resolution of the displacement and deformation measurements was defined by the convolution of these factors. Therefore, it was roughly estimated as $\Delta x = \Delta x\_oct + \Delta x\_ck + \Delta x\_ds$ = 54 μm (lateral) and $\Delta z = \Delta z\_oct + \Delta z\_ck + \Delta z\_ds$ = 77 μm (axial in tissue). This relatively low resolution may account for the broadening of the wire surface signal in the displacement and deformation images [Fig. 5.5.1 (d)–(f)].

In conclusion, we demonstrated a new birefringence and biomechanics analysis method; compression-based PS-OCE. It simultaneously measured two-dimensional birefringence tomography, scattering intensity OCT, spatial-resolved in-plane axial and lateral displacement, the coupled effect of out-of-plane displacement and microstructural decorrelation induced by micrometer-scale tissue compression. Although it is still qualitative, it can be used for detailed analysis of both optical and biomechanical properties of tissues. The results suggest that the PS-OCE is capable of providing more comprehensive insight and information of the microstructures in tissue than the sole use of PS-OCT or OCE. Therefore, it would be helpful to the investigation of collagenous tissues.

6.7 Summary

In this chapter, a new method for simultaneous imaging of birefringence and biomechanical properties of tissue is proposed for the first time. It is based on Jones-matrix based PS-OCT system but equipped with a tissue compression probe, where birefringence tomography, scattering intensity, depth-resolved in-plane axial and lateral displacements, and microstructural decorrelation maps of a biological tissue become available simultaneously. Specifically, this method makes use of OCT images of a tissue obtained from JM-OCT under two different compressive conditions. Using complex correlation maps computed from these two OCT images, depth-resolved axial and lateral displacement maps of the tissue are obtained. In addition, a depth-resolved MSD map is obtained. When a tissue is compressed, microscopic deformation of the tissue ultrastructure, which is smaller than the OCT resolution, occurs in addition to the relatively macroscopic displacement of in and out of the cross-sectional plane in OCT. The MSD map qualitatively visualizes the combined effect of the microstructural deformation and out-of-plane displacement, whereas the current compression OCE only measures tissue displacement and strain. Finally, by utilizing the multiple contrasts including OCT, birefringence tomograms and displacements, MSD maps, the optical and mechanical properties of tissue are analyzed. Although it is still qualitative, it is useful for detailed analysis of both optical and biomechanical properties of tissues. The combination of the birefringence and biomechanical images enables more comprehensive insight and information of the microstructures in tissue than the sole use of PS-OCT or OCE. It would be helpful to the investigation of collagenous tissues.

References

1. E. Li, S. Makita, Y.-J. Hong, D. Kasaragod, and Y. Yasuno, "Three-dimensional multi-contrast imaging of in vivo human skin by Jones matrix optical coherence tomography," Biomed. Opt. Express **8**(3), 1290–1305 (2017).

2. B. F. Kennedy, T. R. Hillman, R. A. McLaughlin, B. C. Quirk, and D. D. Sampson, "In vivo dynamic optical coherence elastography using a ring actuator," Opt. Express **17**(24), 21762–21772 (2009).

3. B. R. Freedman, J. J. Sarver, M. R. Buckley, P. B. Voleti, and L. J. Soslowsky, "Biomechanical and structural response of healing Achilles tendon to fatigue loading following acute injury," J. Biomech. **47**(9), 2028–2034 (2014).

4. M. Yamanari, K. Ishii, S. Fukuda, Y. Lim, L. Duan, S. Makita, M. Miura, T. Oshika, and Y. Yasuno, "Optical Rheology of Porcine Sclera by Birefringence Imaging," PLOS ONE **7**(9), e44026 (2012).

5. A. Itoh, E. Ueno, E. Tohno, H. Kamma, H. Takahashi, T. Shiina, M. Yamakawa, and T. Matsumura, "Breast Disease: Clinical Application of US Elastography for Diagnosis," Radiology **239**(2), 341–350 (2006).

6. A. Lyshchik, T. Higashi, R. Asato, S. Tanaka, J. Ito, J. J. Mai, C. Pellot-Barakat, M. F. Insana, A. B. Brill, T. Saga, M. Hiraoka, and K. Togashi, "Thyroid Gland Tumor Diagnosis at US Elastography," Radiology **237**(1), 202–211 (2005).

7. L. Sandrin, B. Fourquet, J.-M. Hasquenoph, S. Yon, C. Fournier, F. Mal, C. Christidis, M. Ziol, B. Poulet, F. Kazemi, M. Beaugrand, and R. Palau, "Transient elastography: a new noninvasive method for assessment of hepatic fibrosis," Ultrasound Med. Biol. **29**(12), 1705–1713 (2003).

8. L. Xu, Y. Lin, J. C. Han, Z. N. Xi, H. Shen, and P. Y. Gao, "Magnetic resonance elastography of brain tumors: preliminary results," Acta Radiol. **48**(3), 327–330 (2007).

9. J. M. Schmitt, "OCT elastography: imaging microscopic deformation and strain of tissue," Opt. Express **3**(6), 199–211 (1998).

10. K. V. Larin and D. D. Sampson, "Optical coherence elastography - OCT at work in tissue biomechanics [Invited]," Biomed. Opt. Express **8**(2), 1172–1202 (2017).

11. R. K. Wang, S. Kirkpatrick, and M. Hinds, "Phase-sensitive optical coherence elastography for mapping tissue microstrains in real time," Appl. Phys. Lett. **90**(16), 164105 (2007).

12. M. R. Ford, W. J. Dupps, A. M. Rollins, A. S. Roy, and Z. Hu, "Method for optical coherence elastography of the cornea," J. Biomed. Opt. **16**(1), 016005 (2011).

13. M. A. Kirby, I. Pelivanov, S. Song, L. Ambrozinski, S. J. Yoon, L. Gao, D. Li, T. T. Shen, R. K. Wang, and M. O'Donnell, "Optical coherence elastography in ophthalmology," J. Biomed. Opt. **22**(12), 121720 (2017).

14. L. Chin, B. Latham, C. M. Saunders, D. D. Sampson, and B. F. Kennedy, "Simplifying the assessment of human breast cancer by mapping a micro-scale heterogeneity index in optical coherence elastography," J. Biophotonics **10**(5), 690–700 (2017).

15. K. M. Kennedy, L. Chin, R. A. McLaughlin, B. Latham, C. M. Saunders, D. D. Sampson, and B. F. Kennedy, "Quantitative micro-elastography: imaging of tissue elasticity using compression optical coherence elastography," Sci. Rep. **5**, (2015).

16. B. F. Kennedy, K. M. Kennedy, and D. D. Sampson, "A Review of Optical Coherence Elastography: Fundamentals, Techniques and Prospects," IEEE J. Sel. Top. Quantum Electron. **20**(2), 272–288 (2014).

17. S. Wang and K. V. Larin, "Optical coherence elastography for tissue characterization: a review," J. Biophotonics **8**(4), 279–302 (2015).

18. X. Liang, V. Crecea, and S. A. Boppart, "Dynamic optical coherence elastography: a review," J. Innov. Opt. Health Sci. **03**(04), 221–233 (2010).

19. B. F. Kennedy, R. A. McLaughlin, K. M. Kennedy, L. Chin, A. Curatolo, A. Tien, B. Latham, C. M. Saunders, and D. D. Sampson, "Optical coherence micro-elastography: mechanical-contrast imaging of tissue microstructure," Biomed. Opt. Express **5**(7), 2113–2124 (2014).

20. C. Li, G. Guan, R. K. Wang, S. Li, and Z. Huang, "Evaluating elastic properties of heterogeneous soft tissue by surface acoustic waves detected by phase-sensitive optical coherence tomography," J. Biomed. Opt. **17**(5), 057002 (2012).

21. S. Song, N. M. Le, Z. Huang, T. Shen, and R. K. Wang, "Quantitative shear-wave optical coherence elastography with a programmable phased array ultrasound as the wave source," Opt. Lett. **40**(21), 5007–5010 (2015).

22. W. Qi, R. Chen, L. Chou, G. Liu, J. Zhang, Q. Zhou, and Z. Chen, "Phase-resolved acoustic radiation force optical coherence elastography," J. Biomed. Opt. **17**(11), 110505 (2012).

23. A. Ahmad, J. Kim, N. A. Sobh, N. D. Shemonski, and S. A. Boppart, "Magnetomotive optical coherence elastography using magnetic particles to induce mechanical waves," Biomed. Opt. Express **5**(7), 2349–2361 (2014).

24. J. Rogowska, N. A. Patel, J. G. Fujimoto, and M. E. Brezinski, "Optical coherence tomographic elastography technique for measuring deformation and strain of atherosclerotic tissues," Heart **90**(5), 556–562 (2004).

25. B. F. Kennedy, M. Wojtkowski, M. Szkulmowski, K. M. Kennedy, K. Karnowski, and D. D. Sampson, "Improved measurement of vibration amplitude in dynamic optical coherence elastography," Biomed. Opt. Express **3**(12), 3138–3152 (2012).

26. L. Chin, B. Latham, C. M. Saunders, D. D. Sampson, and B. F. Kennedy, "Simplifying the assessment of human breast cancer by mapping a micro-scale heterogeneity index in optical coherence elastography," J. Biophotonics **10**(5), 690–700 (2017).

27. R. C. Chan, A. H. Chau, W. C. Karl, S. Nadkarni, A. S. Khalil, N. Iftimia, M. Shishkov, G. J. Tearney, M. R. Kaazempur-Mofrad, and B. E. Bouma, "OCT-based arterial elastography: robust estimation exploiting tissue biomechanics," Opt. Express **12**(19), 4558–4572 (2004).

28. S. Es'haghian, K. M. Kennedy, P. Gong, Q. Li, L. Chin, P. Wijesinghe, D. D. Sampson, R. A. McLaughlin, and B. F. Kennedy, "In vivo volumetric quantitative micro-elastography of human skin," Biomed. Opt. Express **8**(5), 2458–2471 (2017).

29. K. M. Kennedy, S. Es'haghian, L. Chin, R. A. McLaughlin, D. D. Sampson, and B. F. Kennedy, "Optical palpation: optical coherence tomography-based tactile imaging using a compliant sensor," Opt. Lett. **39**(10), 3014–3017 (2014).

30. L. Dong, P. Wijesinghe, J. T. Dantuono, D. D. Sampson, P. R. T. Munro, B. F. Kennedy, and A. A. Oberai, "Quantitative Compression Optical Coherence Elastography as an Inverse Elasticity Problem," IEEE J. Sel. Top. Quantum Electron. **22**(3), 277–287 (2016).

31. A. Miyazawa, S. Makita, E. Li, K. Yamazaki, M. Kobayashi, S. Sakai, and Y. Yasuno, "Polarization-sensitive optical coherence elastography," Biomed. Opt. Express **10**(10), 5162–5181 (2019).

32. K. Kurokawa, S. Makita, Y.-J. Hong, and Y. Yasuno, "In-plane and out-of-plane tissue micro-displacement measurement by correlation coefficients of optical coherence tomography," Opt. Lett. **40**(9), 2153–2156 (2015).

33. S. Makita, F. Jaillon, I. Jahan, and Y. Yasuno, "Noise statistics of phase-resolved optical coherence tomography imaging: single-and dual-beam-scan Doppler optical coherence tomography," Opt. Express **22**(4), 4830–4848 (2014).

34. K. Kurokawa, S. Makita, and Y. Yasuno, "Investigation of Thermal Effects of Photocoagulation on Retinal Tissue Using Fine-Motion-Sensitive Dynamic Optical Coherence Tomography," PLOS ONE **11**(6), e0156761 (2016).

35. E. Konofagou and J. Ophir, "A new elastographic method for estimation and imaging of lateral displacements, lateral strains, corrected axial strains and poisson's ratios in tissues," Ultrasound Med. Biol. **24**(8), 1183–1199 (1998).

Chapter 7

Conclusions and outlook

7.1 Conclusions

Optical coherence tomography (OCT) has many great benefits for biological samples imaging such as non-invasiveness, high resolution, and large depth imaging range. The multifunctional JM-OCT extended more advantages to conventional OCT as high-speed measurement, specific imaging of biological tissue, and quantitative evaluation of optical properties of tissue. These advantages are very useful for the investigation of clinical medicine and biology.

In this dissertation, the principle and implementing the method of multifunctional JM-OCT has been described in detail at first. Based on this theory, two steps of the development for Jones matrix optical coherence tomography (JM-OCT) have been presented. First, a three-dimensional multifunctional JM-OCT was developed for low transparency biological tissues such as skin. With this multifunctional JM-OCT, multiple contrasts including scattering intensity OCT, OCT angiography (OCT-A), degree of polarization uniformity (DOPU) and birefringence images of the *in vivo* skin tissue have been successfully obtained. The second step, an additional function, which enables the displacement and microstructure decorrelation imaging of biological tissues, have been extended to the JM-OCT. By using this JM-OCT based OCE, simultaneous optical and mechanical properties measurements have been achieved.

7.1.1 Multifunctional JM-OCT for dermatology

A custom made multifunctional dermatological JM-OCT has been demonstrated in Chapter 3. It uses a passive-polarization-delay component based swept-source JM-OCT configuration, but is specially designed for *in vivo* human skin measurement. The center wavelength of its probe is 1310 nm and the A-line rate is 49.6 kHz. The JM-OCT is capable of simultaneously providing birefringence (local phase retardation) tomography, DOPU tomography, complex-correlation-based OCT-A, and conventional scattering OCT. Using these four different OCT contrasts, the morphological characteristics and optical properties of skin tissues were visualized and analyzed.

7.1.2 JM-OCT based OCE

A new method for simultaneous imaging of optical and biomechanical properties of tissue has been developed based on an improved 1.3-μm multifunctional JM-OCT (Chapter 5 and Chapter 6). This method combined the compression OCE technology with the swept-source JM-OCT to implement the OCE imaging for the tissue. By applying the multifunctional imaging method and a digital shifting complex-correlation method, the depth-resolved birefringence tomography, scattering intensity, in-plane axial and lateral displacements, and

microstructural decorrelation maps of a biological tissue can be obtained. With these different specific images, the optical and mechanical properties of biological tissue were observed and interpreted.

7.2 Contributions

- This research successfully demonstrated a multifunctional JM-OCT for *in vivo* human skin imaging. It is the first time to apply the JM-OCT based multi-contrast imaging modality for the skin, which is a low transparency biological tissue.
- For the first time, JM-OCT based OCE is developed and demonstrated to obtain the in-plane axial and lateral displacements and microstructural decorrelation maps. Especially the lateral displacement is successfully measured by a compression OCE, to the best of our knowledge, which has not been reported yet.
- By using the JM-OCT based OCT, simultaneous optical and mechanical properties imaging for biological tissues has been implemented preliminarily.

7.3 Outlook

7.3.1 Limited passive-polarization delay

As mentioned in Chapter 5, the imaging depth range of the multifunctional JM-OCT has been improved by using a long coherence swept source, a longer passive-polarization delay, doubled *k*-clock frequency and increased sampling points. However, the limited passive-polarization delay is not sufficient to use full of the sampling points, such that the corresponding imaging depth in tissue is impossible to achieve the ideal value (designed imaging depth range). And if the passive-polarization delay is further extended, the noise will be increased as well. Currently, the origin of the increased noise along with the extension of passive-polarization delay is unclear. To obtain a sufficient imaging depth range, it is necessary to fix the noise problem of the PPDU with a long delay between two polarizations.

7.3.2 Low resolution of OCE imaging

The resolution of the displacement and MSD images has been illuminated in Chapter 6. It shows that the resolution of OCE imaging is much lower than OCT imaging. Since the mechanical property measurement presented in this study is still qualitative, the low resolution of the OCE images does not significantly affect the results. While, for the accurate quantitative measurement in the future, the resolution of OCE imaging should be improved.

7.3.3 Quantitative OCE imaging

To achieve quantitative analysis of the tissue mechanical properties, i.e. to measure the elastic modulus, the local stress on the tissue should be measured, in addition to the strain. Therefore, a compliant layer is necessary to be employed as a stress sensor [1–4]. With this well-characterized stress sensor, the local stress on the tissue can be estimated. By dividing the local stress by the corresponding local strain in the tissue, the local Young's modulus of the tissue can be calculated, which is mapped into a quantitative micro-elastogram.

7.3.4 Three-dimensional OCE imaging

The digital shifting complex correlation method used in this study was originally designed for quasi-three-dimensional displacement (quasi-3-D) measurement. However, the out-of-plane displacement component is coupled with microstructural deformation, especially in the compression OCE measurement. Here, the microstructural deformation denotes alteration of the physical structure of the sample smaller than the OCT resolution or correlation-computation kernel. This coupling prevents the 3-D displacement measurement and pure microstructural deformation measurement. In a future study, we can modify the digital shifting complex correlation method to be compatible with the 3-D displacement measurement and pure microstructural deformation measurement by using two 3-D OCT volumes with two different compression states. In this case, the out-of-plane displacement and microstructural deformation are decoupled. Therefore, it is safe to interpret the residual decorrelation as microstructural deformation.

References

1. K. M. Kennedy, L. Chin, R. A. McLaughlin, B. Latham, C. M. Saunders, D. D. Sampson, and B. F. Kennedy, "Quantitative micro-elastography: imaging of tissue elasticity using compression optical coherence elastography," Sci. Rep. **5**, (2015).

2. S. Es'haghian, K. M. Kennedy, P. Gong, Q. Li, L. Chin, P. Wijesinghe, D. D. Sampson, R. A. McLaughlin, and B. F. Kennedy, "In vivo volumetric quantitative micro-elastography of human skin," Biomed. Opt. Express **8**(5), 2458–2471 (2017).

3. L. Chin, B. Latham, C. M. Saunders, D. D. Sampson, and B. F. Kennedy, "Simplifying the assessment of human breast cancer by mapping a micro-scale heterogeneity index in optical coherence elastography," J. Biophotonics **10**(5), 690–700 (2017).

4. W. M. Allen, K. M. Kennedy, Q. Fang, L. Chin, A. Curatolo, L. Watts, R. Zilkens, S. L. Chin, B. F. Dessauvagie, B. Latham, C. M. Saunders, and B. F. Kennedy, "Wide-field quantitative micro-elastography of human breast tissue," Biomed. Opt. Express **9**(3), 1082–1096 (2018).

Publications

Journal papers

1. **En Li**, Shuichi Makita, Young-Joo Hong, Deepa Kasaragod, and Yoshiaki Yasuno, “Three-dimensional multi-contrast imaging of *in vivo* human skin by Jones matrix optical coherence tomography,” Biomedical Optics Express, Vol. 8, No. 3, 1290-1305 (2017).
2. **En Li**, Shuichi Makita, Shinnosuke Azuma, Arata Miyazawa, and Yoshiaki Yasuno, “Compression optical coherence elastography with two-dimensional displacement measurement and local deformation visualization,” Optics Letters, Vol. 44, No. 4, 787-790 (2019).
3. Arata Miyazawa, Shuichi Makita, **En Li**, Kohei Yamazaki, Masaki Kobayashi, Shingo Sakai, and Yoshiaki Yasuno “Polarization-sensitive optical coherence elastography,” Biomedical Optics Express, Vol. 10, No. 10, 5162-5181 (2019).

Proceedings of conference

1. **En Li**, Shuichi Makita, Young-Joo Hong, Deepa Kasaragod, Tomoko Sasaoka, Masahiro Yamanari, Satoshi Sugiyama, and Yoshiaki Yasuno, "Three-dimensional multifunctional optical coherence tomography for skin imaging," Photonic Therapeutics and Diagnostics XII, International Society for Optics and Photonics, Vol. 9689, p. 96890N, (2016).
2. **En Li**, Shuichi Makita, Young-Joo Hong, Deepa Kasaragod, and Yoshiaki Yasuno, “Birefringence and vascular imaging of *in vivo* human skin by Jones-matrix optical coherence tomography,” Optical Coherence Tomography and Coherence Domain Optical Methods in Biomedicine XXI, International Society for Optics and Photonics, Vol. 10053, p. 1005317, (2017).
3. Arata Miyazawa, Shuichi Makita, **En Li**, Kohei Yamazaki, Masaki Kobayashi, Shingo Sakai, and Yoshiaki Yasuno, “Tissue analysis using optical and mechanical tissue properties obtained by polarization-sensitive optical coherence elastography,” Proceedings of SPIE, Vol. 11242, p.1124214-1 – 1124214-5, (2020).
4. Kohei Yamazaki, **En Li**, Arata Miyazawa, Masaki Kobayashi, Tetsuya Sayo, Shuichi Makita, Yoshito Takahashi, Yoshiaki Yasuno, and Shingo Sakai, “Depth-resolved investigation of multiple optical properties and wrinkle morphology in eye-corner area with multi-functional Jones matrix optical coherence tomography,” Proceedings of SPIE, Vol. 11211, p.112110R-1 – 112110R-6, (2020).
5. Young-Joo Hong, Yiwei Chen, **En Li**, Masahiro Miura, Shuichi Makita, and Yoshiaki Yasuno. "Eye motion corrected OCT imaging with Lissajous scan pattern," Ophthalmic Technologies XXVI, International Society for Optics and Photonics, Vol. 9693, p. 96930P, (2016).

6. Shuichi Makita, Kazuhiro Kurokawa, Young-Joo Hong, **En Li**, Masahiro Miura, and Yasuno Yoshiaki, "Noise-immune complex correlation for vasculature imaging based on standard and Jones-matrix optical coherence tomography," Optical Coherence Tomography and Coherence Domain Optical Methods in Biomedicine XX, International Society for Optics and Photonics, Vol. 9697, p. 96970J (2016).

7. Deepa Kasaragod, Satoshi Sugiyama, Yasushi Ikuno, David Alonso-Caneiro, Masahiro Yamanari, Shinichi Fukuda, Tetsuro Oshika, Young-Joo Hong, **En Li**, Shuichi Makita, Masahiro Miura, and Yoshiaki Yasuno, "Accurate and quantitative polarization-sensitive OCT by unbiased birefringence estimator with noise-stochastic correction," Optical Coherence Tomography and Coherence Domain Optical Methods in Biomedicine XX, International Society for Optics and Photonics, Vol. 9697, p. 96971I (2016).

International conferences

Oral presentations

1. **En Li**, Shuichi Makita, Young-Joo Hong, Deepa Kasaragod, Tomoko Sasaoka, Masahiro Yamanari, Satoshi Sugiyama, and Yoshiaki Yasuno, "Three-dimensional multifunctional optical coherence tomography for skin imaging," SPIE Photonics West 2016 (BiOS), No. 9689-22, 14 February 2016, San Francisco (U.S).

2. **En Li**, Shuichi Makita, Young-Joo Hong, Deepa Kasaragod, and Yoshiaki Yasuno, "Birefringence and vascular imaging of *in vivo* human skin by Jones-matrix optical coherence tomography," SPIE Photonics West 2017 (BiOS), No. 10053-42, 31 January 2017, San Francisco (U.S).

3. **En Li**, Shuichi Makita, Deepa Kasaragod, and Yoshiaki Yasuno, "Simultaneous tissue birefringence and deformation measurement by polarization sensitive optical coherence elastography with active compression," SPIE Photonics West 2018 (BiOS), No. 10496-44, 28 January 2018, San Francisco (U.S).

4. **En Li**, Yuta Ueno, Shuichi Makita, Tetsuro Oshika, and Yoshiaki Yasuno, "Simultaneous imaging of scleral birefringence and biomechanics by Jones matrix optical coherence elastography," 2018 ARVO Imaging in the eye conference, No. 04, 28 April 2018, Honolulu, Hawaii (U.S.).

5. **En Li**, Shuichi Makita, Arata Miyazawa, Shinnosuke Azuma, and Yoshiaki Yasuno "Simultaneous analysis of optical and biomechanical properties of tissue by compression-based polarization sensitive optical coherence elastography," SPIE Photonics West 2019 (BiOS), No. 10867-77, 6 February 2019, San Francisco (U.S).

6. Arata Miyazawa, Shuichi Makita, **En Li**, Kohei Yamazaki, Masaki Kobayashi, Shingo Sakai, and Yoshiaki Yasuno, SPIE Photonics West 2020, "Tissue analysis using optical and mechanical tissue properties obtained by polarization-sensitive optical coherence elastography", Poster, SPIE BiOS, 11242-39, 2 February 2020, San Francisco, California, US.

7. Kohei Yamazaki, **En Li**, Arata Miyazawa, Masaki Kobayashi, Tetsuya Sayo, Shuichi Makita, Yoshito Takahashi, Yoshiaki Yasuno, and Shingo Sakai, "Depth-resolved investigation of multiple optical properties and wrinkle morphology in eye-corner area with multi-functional Jones matrix optical coherence tomography", Oral, SPIE BiOS, 11211-25, 2 February 2020, San Francisco, California, US.
8. Young-Joo Hong, Yiwei Chen, **En Li**, Masahiro Miura, Shuichi Makita, and Yoshiaki Yasuno, "Eye motion corrected OCT imaging with Lissajous scan pattern," SPIE Photonics West 2016 (BiOS), No. 9693-24, 13 February 2016, San Francisco (U.S).
9. Shuichi Makita, Kazuhiro Kurokawa, Young-Joo Hong, **En Li**, Masahiro Miura, and Yasuno Yoshiaki, "Noise-immune complex correlation for vasculature imaging based on standard and Jones-matrix optical coherence tomography," SPIE Photonics West 2016 (BiOS), No. 9697-18, 15 February 2016, San Francisco (U.S).
10. Makita, Shuichi, Young-Joo Hong, **En Li**, and Yoshiaki Yasuno, "Depth-resolved photothermal optical coherence tomography by local optical path length change measurement," SPIE Photonics West 2016 (BiOS), No. 9710-41, 15 February 2016, San Francisco (U.S).
11. Deepa Kasaragod, Satoshi Sugiyama, Yasushi Ikuno, David Alonso-Caneiro, Masahiro Yamanari, Shinichi Fukuda, Tetsuro Oshika, Young-Joo Hong, **En Li**, Shuichi Makita, Masahiro Miura, and Yoshiaki Yasuno, "Accurate and quantitative polarization-sensitive OCT by unbiased birefringence estimator with noise-stochastic correction," SPIE Photonics West 2016 (BiOS), No. 9697-53, 16 February 2016, San Francisco (U.S).
12. Kohei Yamazaki, **En Li**, Arata Miyazawa, Masaki Kobayashi, Tetsuya Sayo, Shuichi Makita, Yoshito Takahashi, Yoshiaki Yasuno, and Shingo Sakai, "Depth-resolved investigation of multiple optical properties and wrinkle morphology in eye-corner area by multi-functional Jones matrix optical coherence tomography," SPIE Photonics West 2020 (BiOS), No. 11211-25, 2 February 2020, San Francisco (U.S).
13. Arata Miyazawa, Shuichi Makita, **En Li**, Kohei Yamazaki, Masaki Kobayashi, Shingo Sakai, and Yoshiaki Yasuno, "Tissue analysis using optical and mechanical tissue properties obtained by polarization-sensitive optical coherence elastography," SPIE Photonics West 2020 (BiOS), No. 11242-39, 2 February 2020, San Francisco (U.S).

Poster presentations

1. **En Li**, Shuichi Makita, Arata Miyazawa, Shinnosuke Azuma, and Yoshiaki Yasuno, "Lateral and axial displacements and microstructural decorrelation measurement for compression-based optical coherence elastography," SPIE Photonics West 2019 (BiOS), No. 10880-51, 2 February 2019, San Francisco (U.S).

Domestic conferences (Japan)

Oral presentations

1. **En Li**, Shuichi Makita, Young-Joo Hong, Tomoko Sasaoka, Masahiro Yamanari, Satoshi Sugiyama, and Yoshiaki Yasuno "Three-dimensional multifunctional optical coherence tomography for skin imaging," Optics & Photonics Japan 2015, No. 29pA1, 29 October 2015, Tokyo (Japan).
2. **En Li**, Shuichi Makita, Young-Joo Hong, Deepa Kasaragod, and Yoshiaki Yasuno, "Advanced three-dimensional multi-contrast imaging of *in vivo* human skin by Jones matrix optical coherence tomography," Optics & Photonics Japan 2016, No. 1pA1, 1 November 2016, Tokyo (Japan).
3. **En Li**, Shuichi Makita, Deepa Kasaragod, Yoshimi Iwasaki, and Yoshiaki Yasuno, "Birefringence and deformation estimation of biological tissue by polarization sensitive optical coherence elastography," Optics & Photonics Japan 2017, No. 1pA3, 1 November 2017, Tokyo (Japan).
4. Shuichi Makita, Kazuhiro Kurokawa, Young-Joo Hong, **En Li**, Masahiro Miura, and Yoshiaki Yasuno, "Noise-immune complex correlation for optical coherence angiography," Optics & Photonics Japan 2015, No. 29aA6, 29 October 2015, Tokyo (Japan).
5. Shuichi Makita, Young-Joo Hong, **En Li**, and Yoshiaki Yasuno, "Depth-resolved photothermal optical coherence tomography by local optical path length change measurement," Optics & Photonics Japan 2015, No. 29aA7, 29 October 2015, Tokyo (Japan).
6. Deepa Kasaragod, Satoshi Sugiyama, Yasushi Ikuno, David Alonso Caneiro, Masahiro Yamanari, Shinichi Fukuda, Tetsuro Oshika, Young-Joo Hong, **En Li**, Shuichi Makita, Masahiro Miura, and Yoshiaki Yasuno, "Maximum-a-posteriori birefringence estimator for polarization-sensitive optical coherence tomography," Optics & Photonics Japan 2015, No. 29aA8, 29 October 2015, Tokyo (Japan).

Acknowledgements

I really wish to acknowledge everybody who supports me constantly during my Ph.D. study and brings me unique and enjoyable experience at University of Tsukuba. This dissertation would not have been possible without their help and contributions.

First and foremost, I would like to express my most heartfelt gratitude to Professor Masahide Itoh, Professor Masahiro Sasaki and Professor Yoshiaki Yasuno for their generous support, insightful guidance and indispensable encouragement since I started my research from the master course at University of Tsukuba. I am deeply grateful that they accept me as their student and provide me precious opportunity to pursuit my master and doctoral degrees in their laboratories. Their passionate and energetic working styles and talented thinking models have brought profound influence on my attitude towards research and life. The experience I studied at University of Tsukuba will be a period of unforgettable memory in my life. I have been extremely fortunate and honored to be their student.

Besides, I would like to thank Professor Shuichi Makita, Professor Deepa Kasaragod, Dr. Young-Joo Hong, Dr. Kazuhiro Kurokawa, Dr. Arata Miyazawa, Professor Sadao Aoki, and Professor Norio Watanabe for their kind support and help whenever I needed in this study. Their guidance and comments enlighten my understanding and help me remove the obstacles in the research. I really appreciate them very much.

Also, my sincere gratitude is expressed to my doctoral thesis examination committee members (Professor Masahiro Sasaki, Professor Masahide Itoh, Professor Toshiaki Hattori, Professor Hideaki Kano and Professor Yiheng Lim) for their precious time to review my thesis. Their comments and insightful questions make me have new digestion to my research and newly dress the thesis.

Additionally, I should convey my deep appreciation to our collaborators - Biological Science Laboratory of Kao Corporation Odawara Research Center and Optohub Co., Ltd. for the financial, experimental and technical support on this research. Particularly, I would like to sincerely appreciate Mr. Yamazaki Kouhei, Dr. Shingo Sakai, Dr. Masaki Kobayashi and Dr. Tetsuya Sayo from Kao Corporation for the support and discussions on the animal experiments and dermatological investigations. They helped me to remove some obstacles and gave me many valuable advices during the study. I thank them very much.

And the same sincere gratitude is expressed to Dr. Masahiro Yamanari, Mr. Satoshi Sugiyama (Tomey Corporation), Professor B. F. Kennedy (The University of Western Australia & Harry Perkins Institute of Medical), Professor D. Sampson (University of Surrey), and their colleagues for technical and/or theoretical discussions about JM-OCT and OCE, respectively.

This work was supported in part by the Japan Society for the Promotion of Science (JSPS) and Ministry of Education, Culture, Sports, Science and Technology (MEXT) through a contract with the Local Innovation Ecosystem Development Program. And I was personally supported by the Otsuka Toshimi Scholarship

Foundation and JSPS scholarship. I really want to express my deep acknowledgements to these organizations and institutions.

I am also grateful to all current and former members in Yasuno Lab (COG) and Itoh-Watanabe Lab (PDG): Dr. Yiwei Chen, Dr. Aaron Chan, Ms. Danling Liao, Mr. Shinosuke Azuma, Mr. Daisuke Oida, Ms. Chie Yoshinaga, Ms. Kayo Yuyama, Ms. Tomomi Nagasaka; Dr. Feng Lei, Dr. Tetsuya Hoshino, Dr. Kai Chen, Ms. Emiko Ito, Mr. Shiono, Mr. Tada, etc. for their friendship and kind assistance in many aspects for research and even my stay in Tsukuba.

Lastly, I would like to thank my family for their unconditional love and support. They always believe in me and give me a resting place against the tempest and depression. I would also like to thank all relatives for their prayers and invisible support. Then, I would like to give my most special appreciation to my love, Xu Yang. He stands with me together all the time no matter happy or sad. Without his constant love, sacrifice and encouragement, it would not go well for me to complete the thesis.